Analysis of first KM3NeT/ORCA Data and Information Field Theory methods applied to ANTARES Data

Master's Thesis in Physics

submitted by
Johannes Schumann
October 14, 2019

Physikalisches Institut
Erlangen Centre for Astroparticle Physics
Friedrich-Alexander-Universität Erlangen-Nürnberg

Supervisor: PD. Dr. Thomas Eberl

Abstract

The KM3NeT detector is the succeeding experiment of the neutrino telescope ANTARES and it is currently being built in the deep Mediterranean Sea. Within its low energy branch KM3NeT/ORCA four detection units (DUs) are already installed and taking data.
KM3NeT/ORCA is designed for neutrino oscillation research and the determination of the neutrino mass hierarchy.
In the first part of this study different neutrino candidate selection strategies have been implemented and tested on the first available ORCA data. Within this study data and Monte-Carlo simulations with one and two DUs were compared and finally used for developing the event selection criteria.
In the second part a first attempt of applying the information field theory (IFT) framework to neutrino-event-like data was taken. In order to test those methods a toy neutrino sky map was set up, which was then analysed using IFT methods. Finally, a sky map based on the public event selection provided by the ANTARES collaboration was studied. Those reconstructions are based on different correlation structure assumptions, i.e. different initial priors.

Zusammenfassung

Das Neutrinoteleskop KM3NeT ist das Nachfolgeexperiment des ANTARES Detektors und wird aktuell am Grund des Mittelmeeres gebaut. Am dichter instrumentierten Teil KM3NeT/ORCA, welcher zum Zweck der Forschung an der Neutrinooszillation auf niedrigere Energien sensitiv ist, sind zum aktuellen Zeitpunkt vier Detektor Strings in Betrieb und nehmen Daten.
Im ersten Teil dieser Arbeit werden diese Daten analysisert und Neutrinokandidaten mittels unterschiedlicher Selektionen gesucht. Dazu werden Messdaten mit Monte-Carlo Simulationen verglichen, wobei während der Bearbeitung Daten mit ein und zwei Detektor Strings verfügbar waren.
Im zweiten Teil wird ein erster Ansatz zur Verwendung von Infomations Feldtheorie (IFT) zur Analyse von Daten im Format von Neutrinoereignissen erstellt. Dazu wird eine Himmelskarte mit Neutrinoereignissen simuliert und diese dann mittels des IFT Frameworks analysiert. Abschließend wird die publizierte Event Selektion mittels verschiedener zu Grunde liegender Korrelationsstrukturen analysiert.

Contents

1 Motivation

The existence of at least one type of neutrino was first predicted by Wolfgang Pauli in 1930 [1] in order to solve the broken energy conservation by the continous spectrum of the emitted electrons in the β^- decay. More than 20 years later the first detection of a neutrino was realised by Clyde Cowan and Frederik Reines in 1956 and the first model of neutrino flavour oscillations was proposed in 1957 by Bruno Pontecorvo [2].
This phenomena of neutrino flavour oscillations, which requires neutrinos not to be massless, is not even predicted by one of the most elaborate and successful description of matter so far, the standard model of particle physics (SM). Thus, the weak interaction and the detailed properties of the neutrinos and the flavour oscillation mechanism play a major role in particle physics as this might open up a window to "new physics". Due to the importance of this phenomena the Nobel-Prize 2015 was awarded to Takaaki Kajita and Arthur McDonald "for the discovery of neutrino oscillations, which shows that neutrinos have mass" [3].
Within astroparticle physics, the discovery of cosmic rays by Victor Hess in 1912 [4], opened the opportunity for doing research on neutrino oscillations as the cosmic rays provide a natural source of neutrinos. The cosmic rays consist mostly of protons, alpha particles and heavier nuclei, which collide with nucleons in the atmosphere and provide a natural high energetic long baseline neutrino source via the decay products.
Another promising role of neutrinos in astroparticle physics is related to their properties of being electrically neutral, stable and taking part in the weak interaction. Thus, they are not deflected by cosmic magnetic fields, they are very penetrating and they are providing strong evidence for hadronic acceleration in cosmic sources.
The KM3NeT neutrino telescope, which is currently being built in the deep Mediterranean Sea, will be the first cubic-kilometre-sized neutrino detector in the northern hemisphere. It is the succeeding experiment after the ANTARES neutrino telescope, which is taking data since 2008. KM3NeT is split into two branches, where ORCA (Oscillation Research with Cosmics in the Abyss) is the more dense instrumented low energy part designed for doing oscillation research with focus on the determination of the mass hierarchy. ARCA (Astroparticle Research with Cosmics in the Abyss) is the more loose instrumented high energy part searching for astrophysical neutrinos.
This thesis consists of two parts with different analysis types applied to neutrino telescope data. In the first part, measurement data from the first two deployed detection units (DU) of KM3NeT/ORCA are analysed aiming for a selection of neutrino candidates at this minimal detector configuration. For the selection the data is compared to expectations from Monte Carlo simulations and finally the measurement results based on the detected patterns itself are studied.
In the second part a simulation of ANTARES like detector data has been set up for testing the applicability of information field theory (IFT) methods to the field of neutrino astronomy.

Part I

Scientific Context

This part contains the theoretical physics background on neutrino physics and information field theory. It also introduces all relevant context on astroparticle physics and neutrino detection with focus on KM3NeT and ANTARES. Last, an overview over the used and implemented software is provided.

2 Neutrino Physics

Neutrinos are leptons and they take part in the electro-weak interaction within the standard model of elementary paricle physics (SM). Neutrinos are electrical neutral fermions without a colour charge, which means that they only interact weakly via the exchange of W- and Z-Bosons. The chirality of (anti-)neutrinos is left (right) handed. According to current knowledge there exist three lepton families consisting of a neutrino and a massive charged partner particle, which are electrons, muons and taus.

2.1 Neutrino Interactions

Neutrinos only interact via the weak force, which is split up into two interaction channels. The neutral current interaction (NC), i.e. the exchange of a Z-Boson, and the charged current interaction (CC), i.e. the exchange of a $W^{\pm}$-Boson. A schematic of both interaction channels in terms of Feynman diagrams is given in Figure 2.1. The interacting fermions referenced in

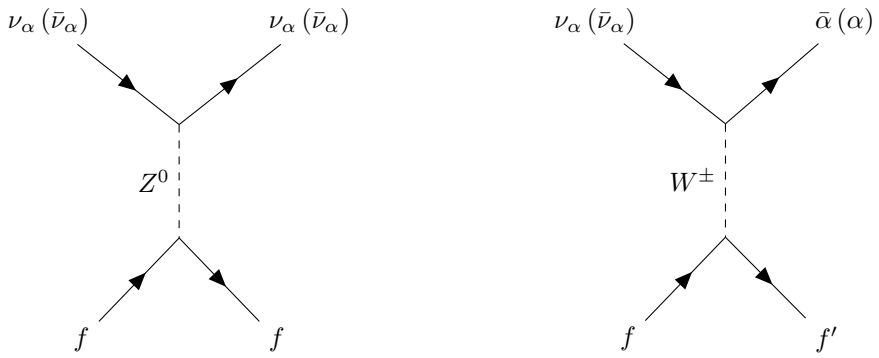

(a) Neutral current (NC) interaction

(b) Charged current (CC) interaction

Figure 2.1: Feynman diagram display of (anti-)neutrinos interactions with matter within the weak interaction.

the Feynman diagrams can either be leptons or quarks of a hadron contained in a nucleon. The elastic scattering cross section with electrons is roughly given by

$$\sigma \approx \frac{2 m_e E_\nu G_F}{\pi}\,, \tag{2.1}$$

where m_e is the electron mass, E_ν the neutrino energy and G_F the Fermi constant [5]. At an energy of 1 GeV this yields $\sigma \approx 1.72 \times 10^{-41}\,\mathrm{cm}^2$ which is three orders of magnitude lower than the cross section for scattering with a nucleon (see Figure 2.2). This reduces the relevant interactions for the detection to the nucleon interaction which yields the event signatures shown in Figure 5.3.

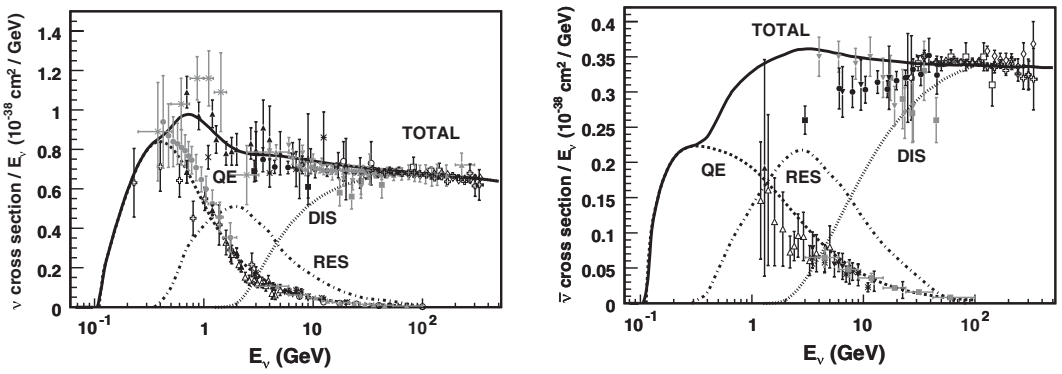

Figure 2.2: Charged-current-interaction cross section for a neutrino (anti-neutrino) nucleon interaction divided by the neutrino energy on the left (right). Taken from [5].

The nucleon scattering can be divided in the following three regimes.

- **Quasi Elastic Scattering(QE):**
  In the lower energy regime the interaction the inner structure of the nucleon cannot be resolved, which leads to an approximatley elastic interaction process.
- **Resonance Production (RES)**
  In the intermediate energy regime of 1-5 GeV the scattering starts to get inelastic. Thus, the neutrino interaction is dominated by the production of baryon resonances, e.g. $\Delta 1232$ [6].
- **Deep Inelastic Scattering (DIS)**
  At higher energies the inner nucleon structure is resolved. The neutrino scatters of directly on a constituent quark, which leads to a more complex scattering dynamic.

The related interaction terms in the SM-Lagrangian are

$$\mathcal{L}_{NC} = \cdots + \frac{g}{\cos\theta_W}\left(\sum_f I_f^3 \bar{f}\gamma_\mu \frac{1-\gamma^5}{2} f - \sin^2\theta_W J_\mu^{em}\right) Z^\mu \quad \text{and} \tag{2.2}$$

$$\mathcal{L}_{CC} = -\frac{g}{\sqrt{2}}\left[\bar{u}_i\gamma^\mu \frac{1-\gamma^5}{2} M_{ij}^{CKM} d_j + \bar{\nu}_i\gamma^\mu \frac{1-\gamma^5}{2} e_i\right] W_\mu^+ + \text{h.c.} \quad . \tag{2.3}$$

The important detail about (2.2) is the factor I_f^3, which is different for each fermion type. I_f^3 is the fermions weak iso spin, which is $+\frac{1}{2}$ for all neutrino types. This means, that from the neutral current interaction the neutrino type cannot be determined.

2.2 Neutrino Flavour Oscillation in Vacuum

Neutrino oscillation is the mechanism to model the state transition between the different neutrino flavours along propagation. This phenomenon is not obvious, as it is not predicted by the SM, which provides, apart from that, a very sophisticated and in many aspects well proven description of matter interaction. Neutrino oscillations were first predicted by Bruno Pontecorvo in 1957 [2] and a first evidence was found by the Homestake experiment in the 1970s measuring a deficit in the predicited solar neutrino flux of the standard solar model[7].
The quantum mechanical differential equation, which describes the dynamics of states, is the time-dependent Schrödinger equation

$$i\partial_t |\psi\rangle = H |\psi\rangle \,, \tag{2.4}$$

where ψ is the wave function and H the system related Hamiltonian. In the vacuum case the neutrino Hamiltonian H has no time dependence and has the eigenvalues,

$$\mathrm{spec}(H) = \{i \in I | E_i\}\,, \tag{2.5}$$

where I is the index set containing the number of neutrino types. These eigen energys are given by the relativistic energy momentum relation.

$$E_i = \sqrt{m_i^2 + p^2}. \tag{2.6}$$

In the case of the mass term being small compared to the momentum, the energy momentum relation can be approximated as

$$E_i \approx E + \frac{m_i^2}{2E}\,. \tag{2.7}$$

In this case of the Hamiltionian H being a diagonal operator, the solution for the Schrödinger equation can be analytically expressed in the form

$$|\nu_i(t)\rangle = \exp\left(\frac{-iE_i t}{\hbar}\right)|\nu_i(0)\rangle\,, \tag{2.8}$$

where ν_i is the related neutrino eigenstate. With respect to the mass dependence of the eigenenergys, those eigenstates are called mass eigenstates. If these are equal to the flavour states, no oscillation can be observed, which indicates, that the flavour states are not an eigenbasis and therefore a superposition of the mass eigenstates.
Transformations between different bases of the underlying Hilbert space are performed via a unitary transformations

$$|\nu_\alpha\rangle = \sum_{i\in I} U_{\alpha i}\,|\nu_i\rangle\ , \tag{2.9}$$

where U is a unitary matrix. Unitary matrices can be written as a product of the rotation operators

$$U = \prod_{a<b\in I} R_{ab} \tag{2.10}$$

which are defined in matrix notation as

$$[R_{ab}]_{\nu\mu} = 1 + (\cos(\theta_{ab}) - 1)\,V_{\nu\mu} - \begin{cases} \sin(\theta_{ab})W_{\nu\mu}\exp\left(\mathrm{sgn}(W_{\nu\mu})i\delta_{ab}\right) & \text{, if } |a-b|>2 \\ \sin(\theta_{ab})W_{\nu\mu} & \text{, else} \end{cases} \tag{2.11}$$

where $a \neq b$ denote the addressed mass eigenstates and ν and μ are the row and column indices. The used matrices V and W are defined as

$$V = \hat{e}_a \otimes \hat{e}_b + \hat{e}_b \otimes \hat{e}_a \quad \text{and} \tag{2.12}$$

$$W = \hat{e}_a \otimes \hat{e}_b - \hat{e}_b \otimes \hat{e}_a. \tag{2.13}$$

Bringing the previous components together, the transition probability is finally given by

$$P(\alpha \to \beta, t) = |\langle\nu_\beta(t)|\nu_\alpha(t)\rangle|^2 \tag{2.14}$$

$$= \left|\sum_{i\in I} U_{\alpha i}U^*_{\beta i}\exp\{-iE_i t\}\right|^2 \tag{2.15}$$

$$= \sum_{i\in I}\left|U_{\alpha i}U^*_{\beta i}\right|^2 + 2\Re\left(\sum_{j>i\in I} U_{\alpha i}U^\dagger_{\alpha j}U^\dagger_{\beta i}U_{\beta j}\exp\{-i\Delta_{ij}\}\right). \tag{2.16}$$

The parameter Δ_{ij} is defined as

$$\Delta_{ij} = \frac{\Delta m_{ij}^2}{2E} = \frac{m_i^2 - m_j^2}{2E}\,, \tag{2.17}$$

which follows directly from (2.7). In the following the standard three flavour case is assumed, which means for the index sets

$$I = \{1, 2, 3\} \qquad \text{and} \tag{2.18}$$

$$\tilde{I} = \{e, \mu, \tau\}\,. \tag{2.19}$$

The unitary matrix in the three flavour case is called PMNS-matrix [1]. The parameters to describe this matrix including the values which were used within this study are given in Table 2.1. The ordering of the mass eigenstates is not determined yet, because only the absolute mass

Parameter	**Value**	**Description**
θ_{12}	$33.62°$	Solar mixing angle
θ_{13}	$8.54°$	Reactor mixing angle
θ_{23}	$47.20°$	Atmospheric mixing angle
δ_{CP}	$234°$	CP violating phase
Δm_{31}^2	$7.40 \times 10^{-5}\mathrm{eV}^2$	Reactor mass difference
Δm_{32}^2	$2.49 \times 10^{-3}\mathrm{eV}^2$	Atmospheric mass difference

Table 2.1: Oscillation parameters for the three dimensional case including the Values taken from [8]

differences are measured. In the following the so-called natural hierarchy

$$m_1 < m_2 < m_3 \tag{2.20}$$

is considered for calculating the flavour transition probabilities. As the arrangement of $m_1 < m_2$ has already been fixed, based on the observation of the neutrino oscillation in the sun [6]. The second remaining option would be

$$m_3 < m_1 < m_2\,, \tag{2.21}$$

which is called inverted hierarchy.

2.3 Neutrino Flavour Oscillation in Matter

The description of neutrino oscillation in matter differs from the vacuum oscillation, as the penetrated medium also influences the propagating neutrinos [9, 10].
The oscillation is not affected by the NC channel, because the coupling of all neutrino flavours is equal, which follows from (2.2). In terms of coherent forward scattering, this leads to a constant phase offset, which does not change the oscillation probability. In the CC channel the flavour families of the involved particles at the interaction vertex have to match, as it is indicated by (2.3) when comparing the indices. Matter at low energies is just composed by electrons, up- and down quarks, i.e. first family particles, which leads to an asymmetry. The description of this effect can be reduced to the description of vacuum oscillations by introducing effective mass eigenstates in matter. In order to calculate these, the vacuum Hamiltonian in the flavour basis is corrected in the ee-term

$$H_{\alpha\beta}^m = H_{\alpha\beta}^0 + \delta_{ee} A\,. \tag{2.22}$$

[1] Named after Bruno **P**ontecorvo, Ziro **M**aki, Masami **N**akagawa and Shoichi **S**akata.

The correction term is defined as

$$A = 2\sqrt{2}G_F N_e \,, \tag{2.23}$$

where G_F is the Fermi constant and N_e the electron density of the medium. The matter Hamiltonian in flavour basis $H^m_{\alpha\beta}$ can be diagonalised

$$H^m_{ij} = \tilde{U} H^m_{\alpha\beta} \tilde{U}^\dagger \,, \tag{2.24}$$

where H^m_{ij} is the diagonal Hamiltonian with new effective neutrino mass eigenstates in matter and $\tilde{U}$ being a new unitary matrix with new effective oscillation parameters in mass.

2.4 PREM Model

The preliminary reference Earth model (PREM) is the most common description of the matter composition of the layers of the Earth. As it is very difficult to measure the properties of the inner composition of the Earth, this model is unchanged since its publication in 1981 [11]. The predicted distribution in terms of the electron density is shown in Figure 2.3.
In the following work the PREM model has been used to predict the matter oscillations of upgoing neutrinos propagated through the Earth.

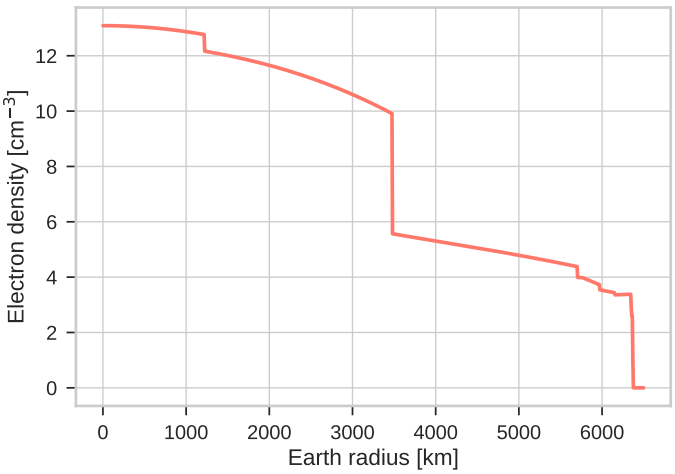

Figure 2.3: Electron density over the Earth radius according to the preliminary reference earth model. Values taken from [11].

3 Astroparticle Physics

In this chapter the relevant details about the astroparticle physics background is outlined. Within the study two different mechanisms of astrophysical particle production are of interest. The production of atmospheric neutrinos (and muons) and neutrinos originated from cosmic sources. In Figure 3.1 the expected composition of the neutrino flux reaching ground is shown.

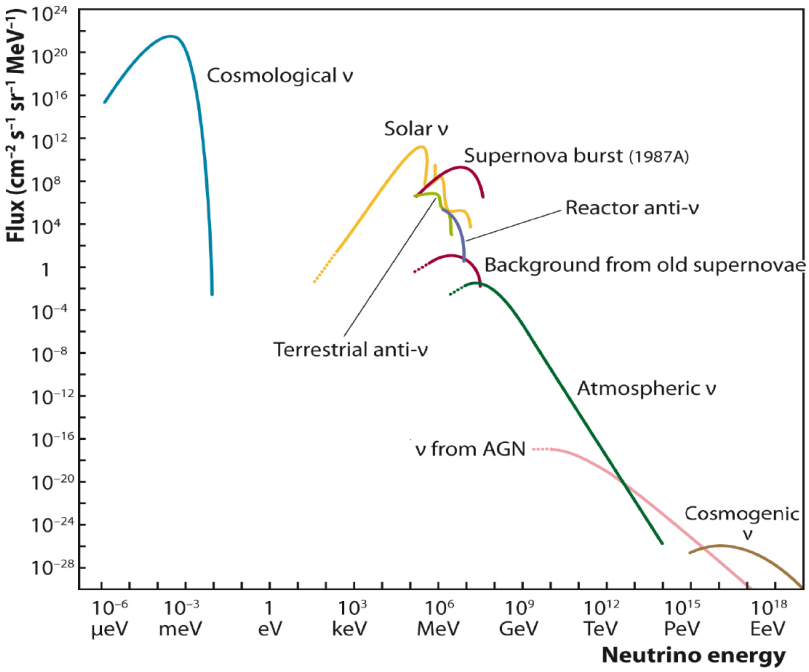

Figure 3.1: Expected composition of the incident neutrino flux from different sources on the Earth. Taken from [12].

3.1 Atmospheric Flux

The atmospheric flux of elementary particles is produced by high energetic extraterrestrial primary particles colliding with nuclei in the atmosphere. Those high energetic extraterrestrial particles are part of the cosmic radiation, which is the diffuse flux of charged particles from galactic and extra-galactic sources hitting the Earth's atmosphere. The majority of those particles are protons and the flux can be described using a power law, i.e.

$$\Phi(E) \propto E^{-\gamma}. \tag{3.1}$$

The collisions of primary particles with nuclei in the atmosphere produce particle cascades called atmospheric showers. Those are boosted towards the ground according to the primary

particle momentum. In Figure 3.2 the different production channels of such a particle shower are given. The most relevant channel for the production of atmospheric neutrinos is the resonant

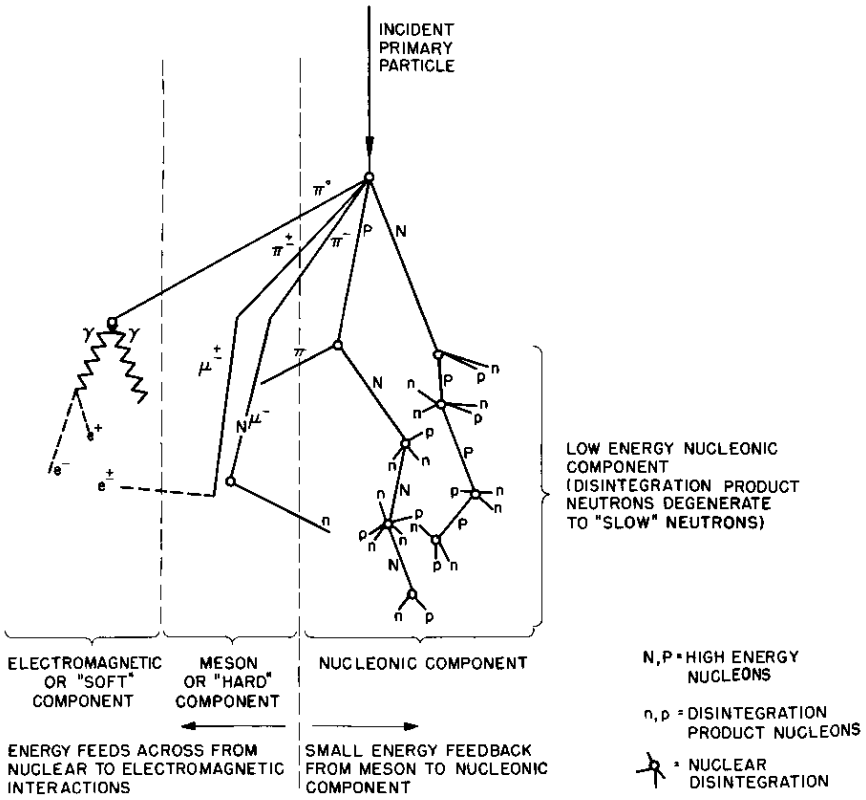

Figure 3.2: Schematic of an atmospheric shower event split into different branches based on the secondary particle type. Taken from [13].

production of mesons, i.e. pions and kaons

$$p + X \rightarrow \begin{cases} \pi + Y & (\pi = \pi^{\pm}, \pi^{0}) \\ K + Y & (K = K^{\pm}, K^{0}) \end{cases} \tag{3.2}$$

A lower bound for the energy regime of this production can be given via the rest mass of the particles, which is

$$m_{\pi^{\pm}} = 139.57\,\mathrm{MeV} \quad \text{and} \tag{3.3}$$

$$m_{K^{\pm}} = 493.68\,\mathrm{MeV}\ [6]. \tag{3.4}$$

Those mesons are very short-lived as their lifetime is in its order of tens of nanoseconds in its rest-frame. This causes them to decay very quickly and only the decay products to reach ground. The decay processes are

$$K^{-(+)} \longrightarrow \mu^{-(+)} + \mu^{0}\,, \tag{3.5}$$

$$\pi^{-(+)} \longrightarrow \mu^{-(+)} + \bar{\nu}_{\mu}(\nu_{\mu}) \text{ and} \tag{3.6}$$

$$\mu^{-(+)} \longrightarrow e^{-(+)} + \bar{\nu}_{e}(\nu_{e}) + \nu_{\mu}(\bar{\nu}_{\mu})\,. \tag{3.7}$$

The neutrinos and muons are the resulting decay products of interest, because electrons can be shielded very easily and do not reach the detector at the sea floor.

Atmospheric Neutrino Flux

The atmospheric neutrino flux is also expected to follow a power-law spectrum as it was introduced in Equation 3.1. According to the flux plot given in Figure 3.3 (left), the power-law index for the atmospheric neutrino flux is expected to be $\gamma_\nu \approx 3$. In Figure 3.4 the flux according to HKKM15 is shown as contour plot over energy and zenith angle. The neutrino ratio between electron and muon flavour at ground from above is shown in Figure 3.3 (right). For an incident direction close to the horizon at $\cos(\theta_z) \approx 0$, the ratio is lower due to the longer mean travel path of the muons in the atmosphere, which yields a higher probability for the muon to decay (3.7) producing electron neutrinos. At higher muon energies, this decay probability is lower, which yields the higher ratio at higher energies.

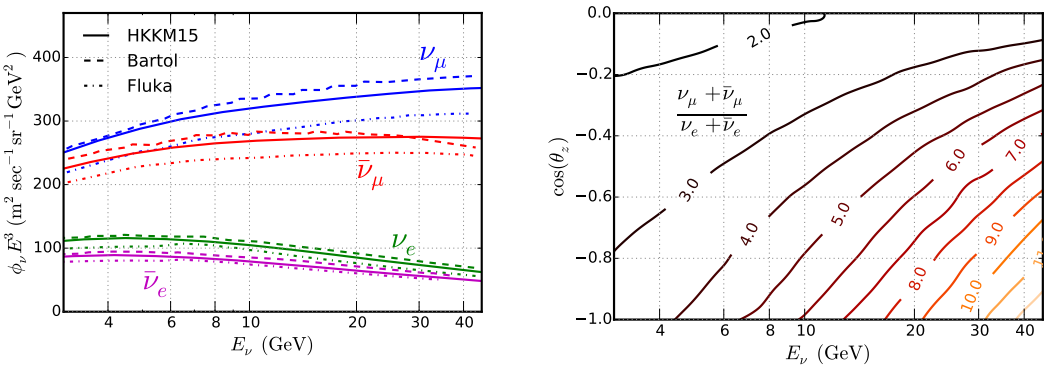

Figure 3.3: Multiple predictions of the atmospheric neutrino flux for electron and muon flavour over energy (left). Contour plot of the electron to muon flavour ratio of the arriving neutrinos based on the HKKM flux over energy and the zenith angle in the upgoing regime (right). Taken from [14].

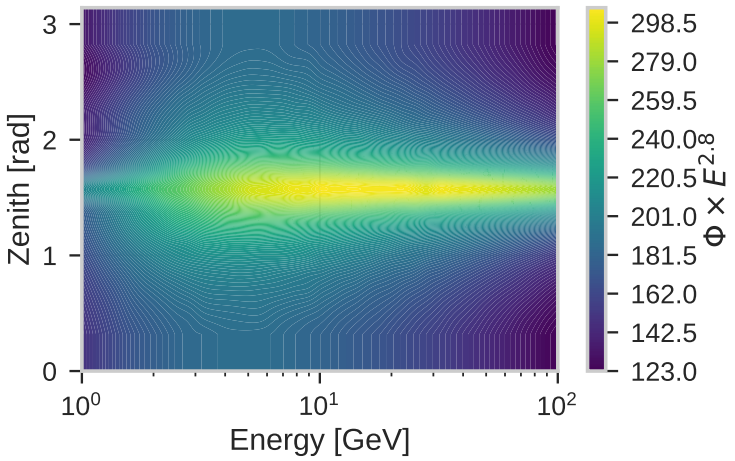

Figure 3.4: Atmospheric ν_μ flux multiplied by $E^{2.8}$ over energy and zenith angle generated using the `km3flux` package.

Atmospheric Muon Flux

The muons produced in the mesonic branch of an atmospheric shower via kaons (3.5) and pions (3.6) decays are so-called atmospheric muons. The mean muon lifetime at rest is $\tau_\mu = 2.2 \times 10^{-6}$ s, which is sufficient for atmospheric muons at higher energies to reach the ground.

This effect is also apparent in the evolution of the ratio between ν_μ and ν_e, where the relative number of ν_μ increases at higher energies (see Figure 3.3).
The flux of atmospheric muons with an energy above $E > 1\,\mathrm{GeV}$ at sea level is about $\Phi_\mu \approx 100\,\mathrm{m}^{-2}\,\mathrm{s}^{-1}\,\mathrm{sr}^{-1} \times \cos(\theta)^2$. Muons at GeV scale are very penetrating with a stopping power of about $\left\langle \frac{dE}{dx} \right\rangle \approx 250\,\mathrm{MeV\,m}^{-1}$ [6], which leads to a remaining intensity at 2.5 km water depth of $I = 3 \times 10^{-8}\,\mathrm{cm}^{-2}\,\mathrm{s}^{-1}\,\mathrm{sr}^{-1}$ [15].
The atmospheric muons propagating through sea water are also emitting Čherenkov light with

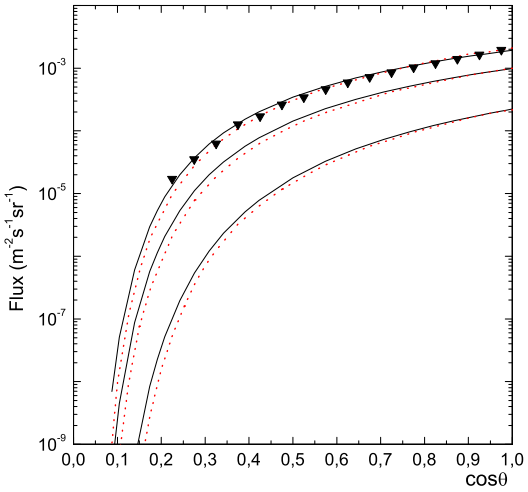

Figure 3.5: MUPAGE simulation of atmospheric muon flux for different depths. The given data points are measured with the AMANDA II detector. Taken from [16].

a track signature, which can be similar to the neutrino event signature and also measured by the detector. Thus, atmospheric muons are an important source of background signals.

3.2 Cosmic High Energy Neutrino Sources

Cosmic elementary particles and in particular cosmic neutrinos are emitted by different sources by different mechanisms. In the regime up to MeV energies those particles can result from nuclear mechanisms, as they occur, e.g. in supernova bursts and in the sun. At higher energies above GeV cosmic acceleration mechanisms are required. Measuring gamma rays from a specific source can give first indication about the acceleration mechanism by its electro-magnetic spectrum. As those can be emitted by inverse Compton scattering

$$e^- + \gamma_{\text{low energy}} \longrightarrow e^+ + \gamma_{\text{high energy}}\,, \tag{3.8}$$

which only requires leptonic acceleration, it is not a proof of hadronic acceleration in the source. Cosmic high energy (HE) neutrinos above GeV from point sources would provide strong evidence for cosmic hadronic acceleration processes.
One neutrino production mechanism, which was not discussed in context of atmospheric processes, is the photo-meson production. Protons at ultra high energies $E_p \approx 10^{20}\,\mathrm{eV}$ can interact with photons from the cosmic microwave background, which leads to the production of mesons, e.g. via the Δ-resonance

$$p + \gamma_{\text{CMB}} \to \Delta^+_{1232} \to p + \pi^0 \tag{3.9}$$

and

$$p + \gamma_{\text{CMB}} \to \Delta^+_{1232} \to n + \pi^+\,. \tag{3.10}$$

The most important phenomena being potential HE neutrino sources are listed below.

- **Supernova Remnants** (SNR) are the remains of supernova explosions. The matter ejected after the core collapse forms shock fronts at high velocities. Charged particles are accelerated to higher energies by Fermi acceleration [17]. This mechanism accelerates particles by multiple scattering at inhomogeneities of the magnetic fields in the shock fronts. The generation of high energetic neutrinos is based on accelerated protons and the pion reactions according to the Equations (3.2), (3.6) and (3.7).

- **Active Galactic Nuclei** (AGN) are super-massive black holes in the center of a galaxy. The black hole accretes a disk of matter and transforms its gravitational energy into radiation and kinetic energy in the relativistic regime, which is aligned along jets. The neutrino production follows from hadronic collisions (3.2) and the subsequent meson decays (3.5) and (3.6).
  If neutrons are created by (3.10) those can escape the large magnetic fields of the jets and decay to protons, electrons and electron antineutrinos.

- **Gamma Ray Bursts** (GRB) are believed to be one of the most powerful phenomena in the Universe, releasing a huge amount of gamma rays within a timespan of milliseconds up to minutes. The most common model for GRBs is the so-called fireball model [18]. It assumes a large ejection of mass, driven by a central process, e.g. the collapse of star into a black hole. The different layers of ejected plasma form shock fronts when one shell is overhauled by its successor. Those shock fronts can accelerate protons by Fermi acceleration up to ultra high energies sufficient for photo-meson production, e.g. (3.9) and (3.10).

In Figure 3.1 the expected source composition of the neutrino flux on ground level is shown. The flux measurement and different expectations on one specific galactic source, the supernova remnant RX J1713.7-3946, is exemplarily given in Figure 3.6. This neutrino spectrum provides

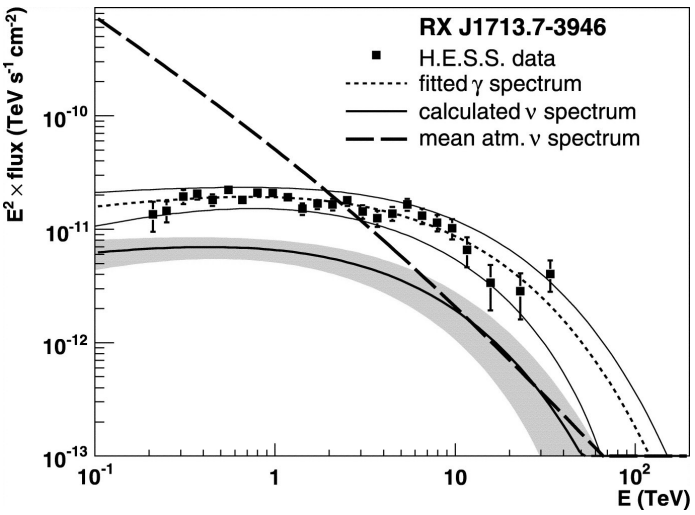

Figure 3.6: Gamma ray flux from the supernova remnant RX J1713.7-3946 measured by the H.E.S.S. telescope. The spectral fit models are based on the assumption of purely from hadronic acceleration originating processes. Taken from [12].

an estimate on the magnitude of the flux norm of

$$\max(E^2 \times \Phi_0) \approx 6 \times 10^{-12} \mathrm{TeV\,s^{-1}\,cm^{-2}}\,. \tag{3.11}$$

4 Information Field Theory

Information Field Theory (IFT) uses concepts of statistical mechanics and field theory to infer information contained in measurement data based on a priori constaints. In this specific case these priors are provided in form of hyper-prior parameters, which are constraints on the correlation structure. Based on that, the correlation structure is then learned using the IFT method based on a optimisation scheme. The following introduction to the topic is based on [19, 20, 21].

4.1 Bayesian Probability & Shannon Information

In the Bayesian picture probabilites are considered to be the quantity of belief in some event. This allows to provide a generic connected between related quantities in a system, which can be used to infer a system quantity of interest. This relation is expressed by Bayes theorem, given by

$$\mathcal{P}(s|d) = \frac{\mathcal{P}(d|s)\mathcal{P}(s)}{\mathcal{P}(d)}\,. \tag{4.1}$$

The quantity s is inferred via the conditional probability at given d, which is called the posterior. The nominator on the right hand side is composed of the conditional probability of d at given s, the likelihood, and the a priori knowledge about the inferred quantity s, the prior. It is normalised by the probability density function (PDF) of d, the evidence, which is negligible, because this term stays constant at a given d. In the following s is the inferred signal field and d is the measurement data.
The Equation (4.1) can also be rewritten in terms of the information Hamiltonian, which is given by the Shannon information

$$\begin{aligned}\mathcal{H}(s|d) &= -\log \mathcal{P}(s|d) && (4.2)\\ &= \mathcal{H}(d|s) + \mathcal{H}(s) - \mathcal{H}(d) && (4.3)\\ &\equiv \mathcal{H}(d|s) + \mathcal{H}(s)\,. && (4.4)\end{aligned}$$

In this study the likelihood is assumed to follow a Poisson distribution, which yields

$$\mathcal{H}(d|s) \equiv \sum \mathcal{R}s - d^\dagger \ln \mathcal{R}s \tag{4.5}$$

where $\mathcal{R}$ implements a prior on a known instrument response. The d dependent term is constant and therefore also negligible with respect to the minimisation. The Hamiltonian of the used Gaussian prior reads

$$\mathcal{H}(s) = \frac{1}{2}\sum_{f\in s} f^\dagger S_f^{-1} f + \frac{1}{2}\ln|2\pi S_f|\,, \tag{4.6}$$

where f are the fields that contribute to the final composition of the signal s. The covariance $S_f(x,x')$ is assumed to be homogeneous and isotropic, which can be satisfied by the kernel being only dependent on the absolute distance of two points, i.e. $S_f(x,x') = S_f(|x-x'|)$. Thus, this is basically a spatial correlation between two values of the field f over a certain distance $r = |x-x'|$. Using the Wiener-Khintchin theorem and the assumption of the Gaussianity of

the studied fields $f \in s$ it can be shown, that the covariance is a diagonal operator in harmonic space. The correlation structure is therefore fully described via its power spectrum, which is defined as

$$C^{(f)} = \mathbb{P} \left\langle \hat{f} \hat{f}^* \right\rangle_{\mathcal{P}(x)} , \tag{4.7}$$

where $\mathbb{P}$ projects the one dimensional power spectrum to the diagonal of the covariance $\widehat{S}_f$ in the harmonic domain of the field f. The power spectrum, i.e. correlation function in harmonic space, is modeled via a log-normal field. This is a convenient parametrisation with respect to the energy of a harmonic oscillator, which has a ω^2 dependency. The log-normal field also ensures positivity and it is determined by the exponent τ_f. The amplitude operator is now defined as

$$A_f = \mathbb{P} \exp\left(\frac{1}{2}\tau_f\right) , \tag{4.8}$$

which is used to finally write the covariance S_f as

$$S_f = \mathbb{F} A_f A_f^\dagger \mathbb{F}^\dagger , \tag{4.9}$$

where $\mathbb{F}$ is the harmonic transformation operator. In order to separate the sample values from a specific power spectrum during the optimisation process and therefore reduce the computational cost for inferring the field f, it can be reparametrised as it was shown by Knollmüller et al. in the following form

$$f = \mathbb{F} A_f \xi_f , \tag{4.10}$$

where ξ_f is a white Gaussian field with zero mean and unit covariance. At this point the problem is reduced to a one dimensional problem with respect to the field τ_f, which is addressed by the reparametrisation again. Therefore an additional white Gaussian field ζ_f is introduced and the allowed variability is set by the hyper prior parameters σ_f and l_f and. The whole hierarchy of those dependencies is given as a tree in Figure 4.1.

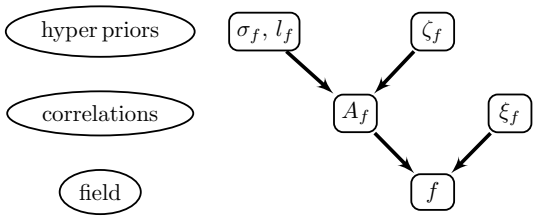

Figure 4.1: Hierarchical tree model for a generic Gaussian field f, as it was used for the sky and energy domain. The parametrisation of the model is carried out via the hyper priors σ_f and l_f. The correlation structure is encoded to the amplitude field A_f. Taken from [21]

In this study also a spherical domain is considered, which was used for the event direction. The previous description can also be applied to this special case, where the specific details can be found in [21].
The final posterior Hamiltonian is therefore given by

$$\mathcal{H}(s|d) \equiv \mathcal{H}(d|s) + \mathcal{H}(s) \tag{4.11}$$

$$\equiv \sum \mathcal{R}s - d^\dagger \ln \mathcal{R}s + \sum_{f \in \mathbf{s}} \xi_f^\dagger \xi_f + \mathcal{H}(\tau_f | \zeta_f, \sigma_f, l_f) , \tag{4.12}$$

where the last partial Hamiltonian contains the information about the hyper priors and is used to infer the fields τ_f [21].

4.2 Gaussian Variational Inference

The Hamiltonian in Equation (4.12) fully contains the information necessary to solve the minimisation problem. Due to its non-linear terms the expression for the posterior distribution is obviously not Gaussian and therefore not trivial to evaluate as an analytic solution is not inevitably existing. Thus, variational inference is used to obtain results using an approximate posterior distribution, which also provides numerical stability and accurate results on reasonable timescales. Within this method, the Kullback-Leibler Divergence (KL) is minimised, which is given by

$$\mathcal{D}_{\mathrm{KL}}\left(\tilde{\mathcal{P}}(s|d)||\mathcal{P}(s|d)\right) = \int \mathcal{D}s\, \tilde{\mathcal{P}}(s|d) \ln\left(\frac{\tilde{\mathcal{P}}(s|d)}{\mathcal{P}(s|d)}\right) \tag{4.13}$$

$$= \langle \mathcal{H}(s|d)\rangle_{\tilde{\mathcal{P}}(s|d)} - \langle \tilde{\mathcal{H}}(s|d)\rangle_{\tilde{\mathcal{P}}(s|d)}\,, \tag{4.14}$$

where $\tilde{\mathcal{P}}$ denotes the approximate probability distribution. In this case $\tilde{\mathcal{P}}$ is assumed to be a Gaussian. The second term is

$$\langle \tilde{\mathcal{H}}(s|d)\rangle_{\mathcal{G}(s-\bar{s},S)} = \frac{1}{2}\ln|2\pi e S|\,, \tag{4.15}$$

where $\langle s\rangle$ is the mean of the signal where the Gaussian is shifted to. This determinant of the covariance S is negligible, because it is mostly independent of the mean $\langle s\rangle$. This yields for the KL

$$\mathcal{D}_{\mathrm{KL}} \equiv \langle \mathcal{H}(s|d)\rangle_{\mathcal{G}(s-\bar{s},S)} \tag{4.16}$$

where the minimisation follows the gradient

$$\partial_{\bar{s}}\mathcal{D}_{\mathrm{KL}} \equiv \langle \partial_s \mathcal{H}(s|d)\rangle_{\mathcal{G}(s-\bar{s},S)}\,, \tag{4.17}$$

which is numerically evaluated by Kullback-Leibler sampling (see Section 6.6).

5 Neutrino Detection

The detection of neutrinos is a challenging task due to their elusive nature. Neutrino detectors are tuned to measure secondary particles resulting from a weak interaction process with a primary neutrino, as it was introduced in section 2.1. There are multiple concepts for such measurements, e.g. radio chemical experiments searching for elements in the target medium, which are produced by a neutrino interaction caused nucleon transition. The following work focuses on water Čherenkov detectors, as it is the working principle of the ANTARES and KM3NeT experiments.

An overall parameter for scattering experiments is the interaction rate ν, which is given by

$$\nu = \sigma \times \Phi \times n_\rho \times V, \tag{5.1}$$

where V is the target volume, σ is the cross-section, Φ is the incident particle flux and n_ρ is the nucleon density of the target material. In order to get sufficient statistics on reasonable timescales, these properties have to be considered when planning an experimental setup. The cross section σ is a property of the underlying physical mechanism, which cannot be tuned. Also the nucleon density of the target material n_ρ can only be chosen in a very narrow range, determined by the suiting target materials. For accelerator and beam line experiments the particle flux Φ can be adjusted. The flux is not increasing linearly with the beam intensity as for long beam lines the angular accuracy of the beam is an important parameter. When it comes to natural particle fluxes, e.g. atmospheric neutrinos, this parameters is also fixed.
The volume of the target material V can be chosen freely and is only limited by technical constraints.

5.1 Water Čherenkov Detectors

In the working principle of the Čherenkov neutrino detector design the emitted Čherenkov light of the secondary charged particles of a neutrino interaction is used for detection.

Čherenkov radiation is emitted by charged particles propagating through a polarisable medium faster than the speed of light in that medium. The geometry can be derived using Huygens picture of a super position of spherical waves. The related picture to Huygens principle and the resulting light cone, which is also called Čherenkov cone, is shown in Figure 5.1.
An important parameter to resolve the track geometry is the opening angle of the Čherenkov cone, which is given by

$$\cos(\theta_C) = \frac{1}{n\beta}\,, \tag{5.2}$$

where n is the refractive index of the dielectric medium and β is the velocity of the charged particle divided by the speed of light in vacuum. The Čherenkov angle over energy is given in Figure 5.2, where the angle value steeply rises in the regime of $\mathcal{O}(100MeV)$ and is almost constant at higher energies. Thus, the angle value can be assumed to be constant with $\theta_C^{\text{water}} = 42°$, which is the approximation for $\beta \approx 1$ and the refractive index $n_{\text{water}} = 1.35$.

In order to measure the Čherenkov light the target volume is equipped with optical sensors.

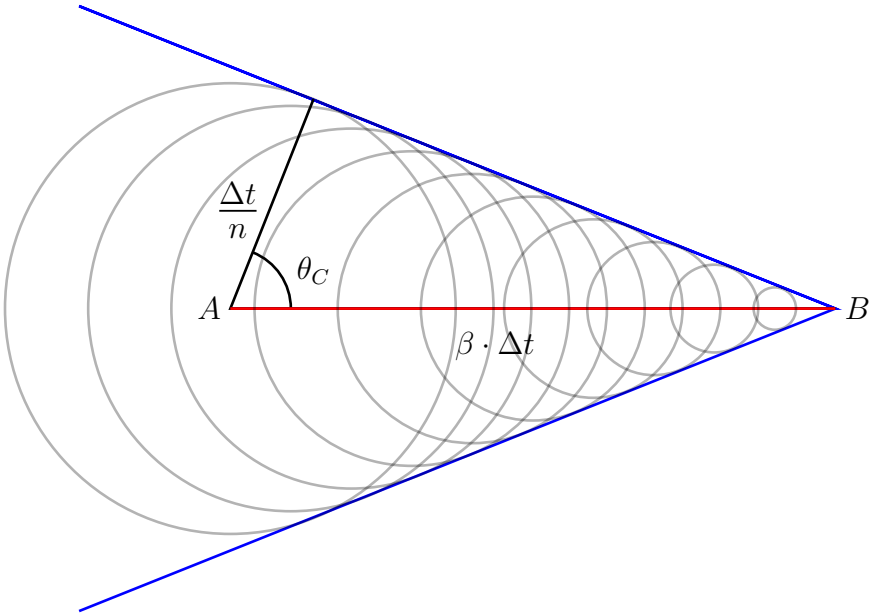

Figure 5.1: Visualisation of the Čherenkov cone geometry produced by a particle track (red) of length $\overline{AB} = \nu\Delta t$. The blue lines yield the light front forming the cone. Modified from [22].

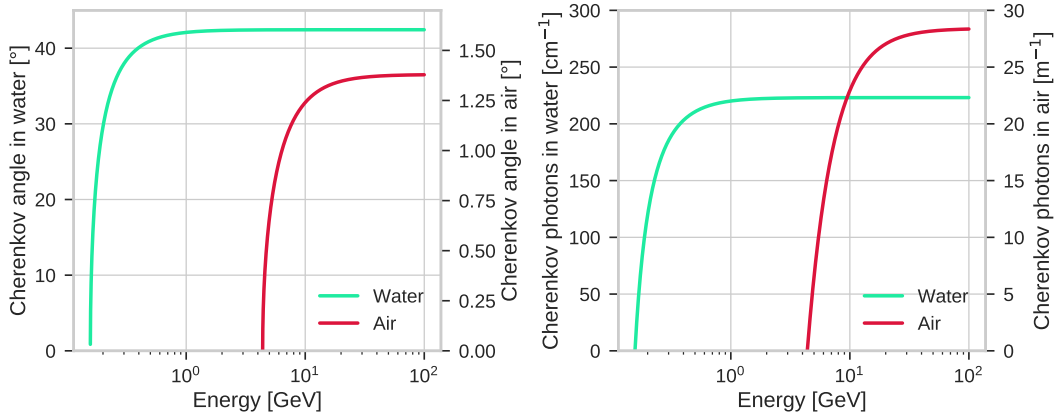

Figure 5.2: Čherenkov angle (left) and number of emitted Čherenkov photons per track-length (right) over energy.

Those are positioned within a grid at distances typically below the optical absorption length of the target medium.
The main advantage of Čherenkov detectors compared to other detector concepts, e.g. radio chemical experiments, is the possibility to resolve the initial neutrino direction to a certain accuracy. This is done by reconstructing the track geometry of the secondary particle based on the Čherenkov hypothesis. The accuracy is limited by the kinematics of the neutrino interaction and the detection precision with respect to the position and time resolution of the optical sensors. An overview over the interaction channels and the related track characteristics is shown in Figure 5.3.

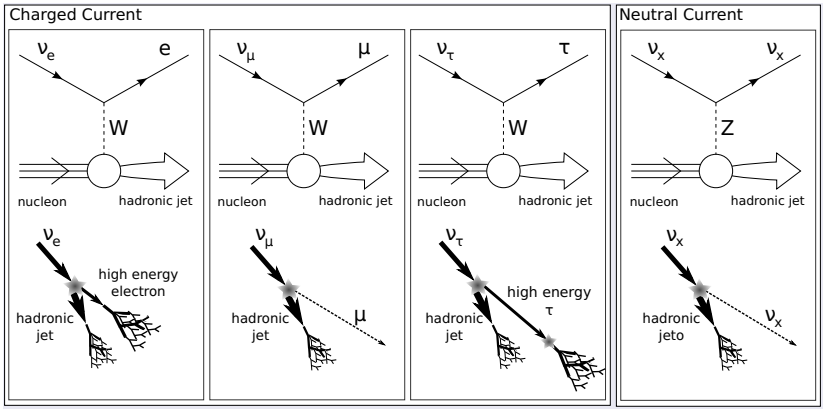

Figure 5.3: Neutrino-interaction channels with associated event signature in the detector. Taken from [23].

5.1.1 Background Light Sources

As natural water reservoirs are not self-contained, additional light sources can contribute to the signal beside Čherenkov light induced by the elementary particles processes expected to occur in the water. In the Mediterranean Sea the main optical background is produced by potassium-40 and bioluminescence.
Also light emission from the detector hardware can contribute to the background light field.

Potassium-40

The radioactive isotope potassium-40 has a natural occurrence in the seawater. The overall activity of potassium-40 in the sea depends on the water composition, i.e. the salinity. The decay of this isotope can cause particles above the Čherenkov threshold to emit light. Measurements within the ANTARES project show an activity of about $A \approx 14\,\mathrm{kBq\,m^{-3}}$ in the Mediterranean Sea [24]. The statistical most probable decay is β^-

$$^{40}_{19}\mathrm{K} \quad \longrightarrow \quad ^{40}_{20}\mathrm{Ca} + e^- + \bar{\nu}_e\,, \tag{5.3}$$

which has a branching ratio of 89.29 %. The released energy from the transition of this decay is 1.3 MeV, which goes mostly into the kinetic energy of the electron. The second most probable process is the electron capture

$$^{20}_{19}\mathrm{K} \quad \longrightarrow \quad ^{20}_{18}\mathrm{Ar} + \nu_e + \gamma\,, \tag{5.4}$$

which has a branching ratio of 10.72 %. The emitted γ-photon has an energy of 1.5 MeV. This momentum can be transferred to an electron via inverse compton scattering, which again emits Čherenkov light. Potassium-40 can also decay via β^+, which has a probability of 10^{-3} % and therefore has no relevant contribution to the intensity of the light emission.

Bioluminescence

The effect of bioluminescence describes the capability of organisms to emit light in the visible regime. The continuous emission is in the order of few photons which contributes to the background rate of detected photon events at the PMTs. Additionally to the continuous emission, light bursts with a higher amount of photons on a nanosecond time scale can occur. Those can be detected and triggered on as event pattern by the detector.

Cross talk

The components of a neutrino detector are designed to detect very faint light, which requires a very elaborate construction with high amplification on nanosecond timescales. Those designs can also emit light, which can be detected by the other sensors in the setup. In the case of photomultiplier-tube (PMT) based experiments the dynode structure can produce sparks. The light of the sparks can propagate outwards through the glass of the tube and be detected by other PMTs.

5.1.2 ANTARES

The ANTARES[1] experiment is a first generation neutrino telescope in the deep sea. It is located roughly 40 km off the French coast near the city of Toulon at a depth of 2450 m (see Figure A.1). The data taking in the final detector configuration started in 2008.
The detector consists of 12 so-called strings equipped with 25 optical storeys each and are anchored at and connected to the seafloor and tautened upright by buoys. The distance between the strings is about 60 m and the vertical spacing in between the storeys is about 15 m. Every optical storey is equipped with 3 optical modules and a central electronics container. The optical modules (OMs) consist of a pressure-resistant glass vessel housing a 10-inch photomultiplier tube (PMT), its high-voltage supply and a mu-metal cage for magnetic shielding. The OMs are pointing 45° downwards, with an angular distance of 120° in the horizontal plane to each other.
The detector also contains acoustic storeys which are equipped with hydrophones. These are part of the AMADEUS [2] project, which studies the feasibility of the acoustic neutrino detection in the ultra-high energy regime.
All strings are connected to a central junction box using optical fibres. In the junction box the data is gathered and sent to the coast via a submarine cable. In Figure 5.4 a schematic of the detector including pictures of both storey types is shown.
The reconstruction of the event geometries in ANTARES require precise knowledge about the position and time of the measured events. Even though the strings are held upright by the buoys, the positions of the storeys are drifting due to the sea current. The Storeys are equipped with LEDs to emit light which can be detected by the OMs around for a relative position calibration.

5.1.3 KM3NeT / ORCA

The KM3NeT detector is the succeeding experiment of ANTARES, which is currently being built in the Mediterranean Sea. The detector is split up into two branches, which are also separated by two different locations.

The high energy branch is named ARCA[3] and it is located offshore at Sicily. It consists of two so-called building blocks (see Section 5.1.3), which are less densely instrumented to cover a higher effective volume. The scientific goal of this branch is the identification of high energetic neutrinos from galactic and extra-galactic sources.

[1] **A**stronomy with a **N**eutrino **T**elescope and **A**byss environmental **RES**earch
[2] **A**NTARES **M**odules for the **A**coustic **D**etection **U**nder the **S**ea
[3] **A**stroparticle **R**esearch with **C**osmics in the **A**byss

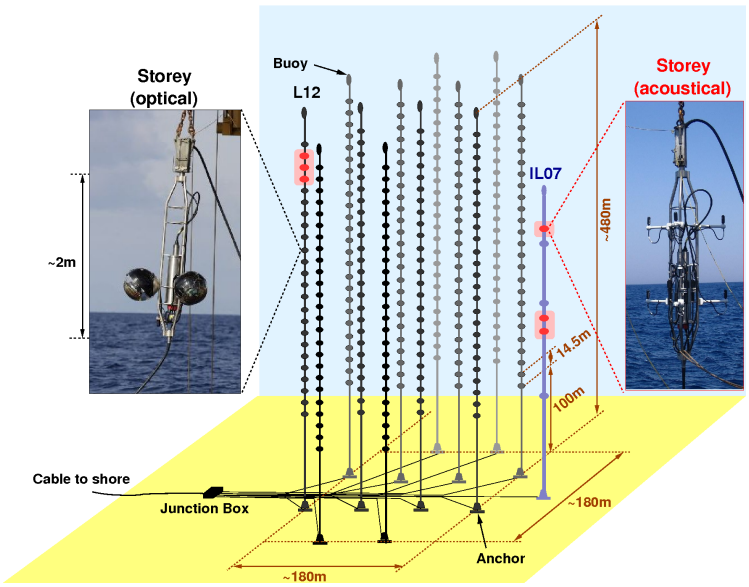

Figure 5.4: Schematic of the ANTARES neutrino detector, including pictures of an optical storey (left) and an acoustic storey (right). The positions of the acoustic storeys in the detector are marked in red. Taken from [25].

The low energy branch, which is named ORCA[4] is close to the location of the ANTARES site (see Figure A.1), which is roughly 40km off the French coast near the city of Toulon. It will consist of one building block, which is more densely instrumented for a better energy resolution at the $\mathcal{O}$(GeV) regime. ORCA adresses the research on neutrino physics and particularly the measurement of the neutrino mass hierarchy.

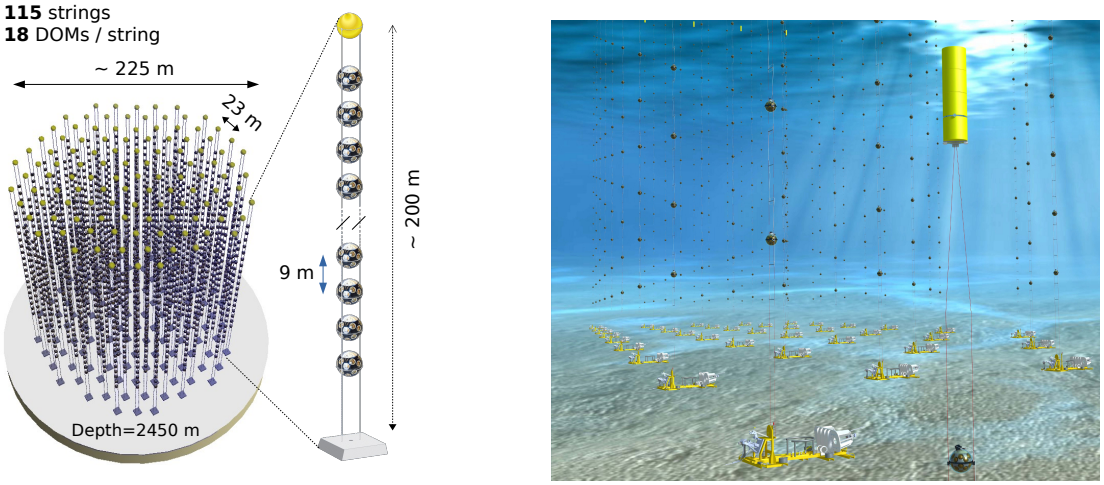

Figure 5.5: Schematic of a whole building block and a single detection unit including the ORCA dimensions (left) and an artists impression of the detector site (right). Taken from [26] and [27].

In Figure 5.5 a visualisation of a building block and the detector in sea environment is given.

[4] **O**scillation **R**esearch with **C**osmics in the **A**byss

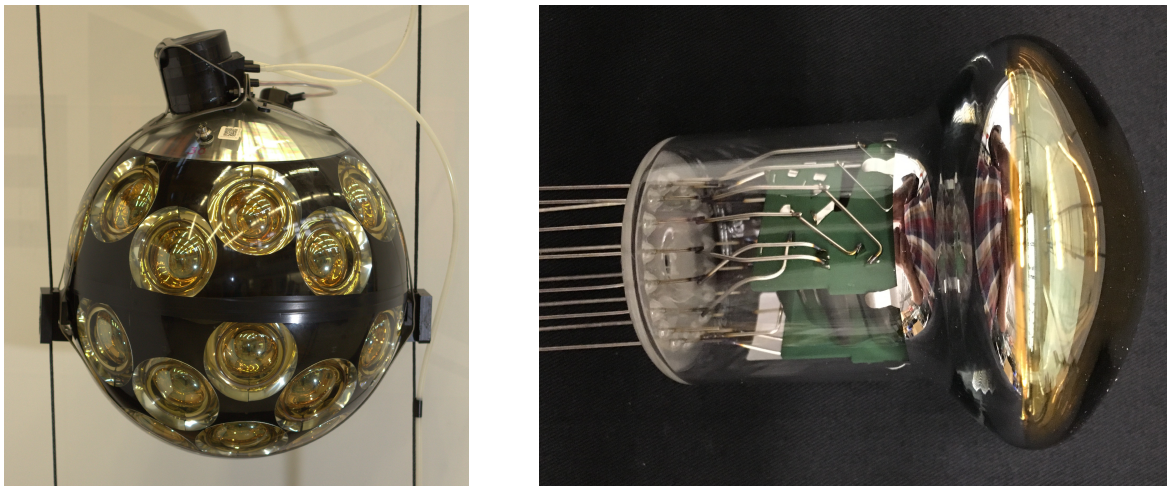

Figure 5.6: KM3NeT digital optical module (left) carrying 31 photomultiplier tubes of type Hamamatsu R12199 (right). DOM picture taken from [27].

Hardware

The largest substructure of the detector is a building block, which is the compound of 115 so-called detection units (DU). A DU is comparable to a detector string in the ANTARES string, but it carries 18 digital optical modules (DOM). A DOM is a module integrated in a pressure-resistant glass sphere, which houses 31 photomultiplier tubes (PMT) and the associated electronics. The electronics consists of the high-voltage supply, which can be adjusted for each PMT individually, and the data aquisition. The DOMs are connected to the power supply and an optical fiber connected to the junction box, which is gathering the data and sending it via an under sea cable to the on-shore station. The PMTs are arranged in 5 rings with 6 PMTs each, which are shifted by $\Delta\varphi = \frac{\pi}{3}$ and one PMT facing directly downwards to cover a maximum of the spheres surface. At the top of the upper hemisphere an area of about $\Omega = \frac{1}{2}\pi$ is not equipped with PMTs, but with an aluminium structure the so-called mushroom. It is placed at the top of the DOM in order to get the most effective photo cathode area facing downwards and therefore to get the maximum sensitivity for upgoing events. The mushroom is used as mount for the central logic board (CLB) and acts also as heat sink for the CLB. The penetration for connecting the power supply and the data fibers to the DOM is also located at the mushroom. Thus, no photo cathode area is covered by those items and it can be directly connected to the CLB.

Current Project Status

The ORCA detector is currently in the deployment phase towards phase 1, which is a setup consisting of 7 DUs. As so far four DUs are deployed and taking data. In Table 5.1 the chronology of the ORCA detector operation from the first start of a DU operating until present is given. For the analysis and neutrino candidate selection in Part II only data from the setup

Description	2017				2018												2019									
	9	10	11	12	1	2	3	4	5	6	7	8	9	10	11	12	1	2	3	4	5	6	7	8	9	10
Schedule KM3NeT																										
One DU running																										
Main sea cable failure																										
Two DUs running																										
Four DUs running																										

Table 5.1: Deployment timeline of the ORCA detector from first detection unit (DU) running until present.

with one and two DUs running is used. This is mainly caused by the availability of comparable Monte-Carlo simulations of a similar setup configuration. The used datasets have a equivalent detector livetime of 125 d for one DU and 17 d for two DUs.

6 Software & Data

In the following section all relevant details about the software and data, which were used to gain the results in part II and III are outlined.

6.1 JFit Reconstruction

JFit is the namespace of the different track hypothesis reconstruction algorithms applied to the measured and simulated detector data. It is part of the main KM3NeT data processing framework JPP [28]. The different stages, each performing a maximum likelihood optimisation, are:

JPrefit reconstructs the coordinates $\{x_0, y_0, t_0\}$ of some pivot on the particle track for fixed track direction. These parameters are used because they appear linearly in the equation defining the track hypothesis, which makes it numerically easy to optimise them. As the track direction is not reconstructed and needs to provided previously. Thus, the prefit algorithm is applied multiple times over an angular grid.

JSimplex reconstructs the coordinates $\{x_0, y_0, t_0\}$ of the interaction vertex and the track direction $\cos(\theta), \cos(\phi)\}$. As this is a more complex problem, JSimplex proper starting values need to be provided, which can be taken from the best JPrefit results. The minimiser of JSimplex uses Powell's method of a likelihood based on the logarithm of the squared time residuals.

JGandalf reconstructs also the coordinates $\{x_0, y_0, t_0\}$ of the interaction vertex and the track direction $\cos(\theta), \cos(\phi)\}$. It also requires starting values to be provided, which can be taken from the best JPrefit and JSimplex results. JGandalf uses the Levenberg-Marquardt method for minimising the likelihood. The likelihood is based on the expected number of received photoelectrons per time, which is given via Monte-Carlo generated probability density functions (PDF).

JEnergy is a one parameter scan over the parameter $\log \mathrm{Energy}$, which is used to generate the PDFs based on a fixed track position and direction. The track parameters can be taken from the reconstruction of JSimplex and JGandalf.

JStart is a one parameter scan of the vertex z-coordinate z_0, which is used to generate the PDFs based on a fixed track position and direction. The track parameters can be taken from the reconstruction of JSimplex and JGandalf.

These reconstruction stages allow for different reconstruction sequences, which are indicated via a bitmask.
In Part II different data versions are referenced, for which the data is retriggered and reconstructed using an updated detector calibration. The parameters which are calibrated are the time calibration, the PMT efficiencies and minor updates in the monte carlo simulations to match the detector response. In the Appendix the details about the used versions and the related run-selections are given.

6.2 KM3Py

KM3Py is the superordinate namespace of Python based packages which were particularly developed for the KM3NeT project. All data and informations of the packages within this namespace can be retrived at [29].

6.2.1 KM3Pipe

The KM3Pipe module has been developed for data processing purposes within the KM3NeT project. It uses a pipeline structure, which is shown via an exemplary code given in Listing 6.1. It is independent from JPP [28] but compatible to its data formats. Thus, it can be used to read the hit information and reconstruction tables. The module also contains different functionalities, which are convienient for data processing. Notable here is the reader for the detector information, which can be used to calibrate the hit information and provides the whole detector geometry.

6.2.2 KM3Flux

The KM3Flux package is a tool for providing the energy and zenith dependent atmospheric neutrino flux. It is based on a predefined lookup table file and includes also a interpolation functionality. The main lookup table is based on the measured atmospheric neutrino flux by experiments at the Frejus site, which is near Toulon and therefore close to the KM3NeT/ORCA detector site. The data from different experiments including the used data from Frejus site can be retreived from [30].
The interpolation uses bi-splines to the third order on a rectangular grid directly applied to the read flux values. As the flux is expected to follow also a powerlaw spectrum (comparable to (3.1)), the range of flux values spans 6 orders of magnitude for $E \in \mathcal{O}(\mathrm{GeV})$ at the spectal index $\gamma \approx -3$. This systematic was used to modify the interpolation algorithm to gain a better interpolation quality. The discrete flux from the lookup table was multiplied by a factor of E^{α} to flatten the flux, to interpolate just the shape which deviates from the power law distribution. This also can be expressed as

$$\Phi(E) = I\left[\Phi_{\mathrm{in}}(E) \times E^{\alpha}\right] \times E^{-\alpha}\,, \tag{6.1}$$

where $\Phi_{\mathrm{in}}(E)$ is the discrete flux from the lookup table, $\Phi(E)$ is the interpolated flux, I states the application of the interpolation and α is the used spectral index for the flattening. In order to find an appropriate value for α the orders of magnitude of the flux within the parameter space of energy and zenith were minimised. In Figure 6.1a the distribution of this magnitude range over α is given. The remaining 1.5 orders of magnitude at the minimum mainly result from the zenith distribution, which was not included in the flattening. In Figure 6.1b the relative differences of the cubic bivariante spline interpolation with and without the flattening at the minimised parameter $\alpha = 2.85$ is given.

6.3 OscProb

The calculation of the transition probabilities of neutrino flavour states (see section 2.2) is done using the software OscProb. It was developed by Joao Coelho and includes multiple features with respect to different neutrino models and the propagation through matter. For matter oscillations it also contains an implementation of the PREM model [11] to include the neutrino propagation through the earth (see Section 2.4).

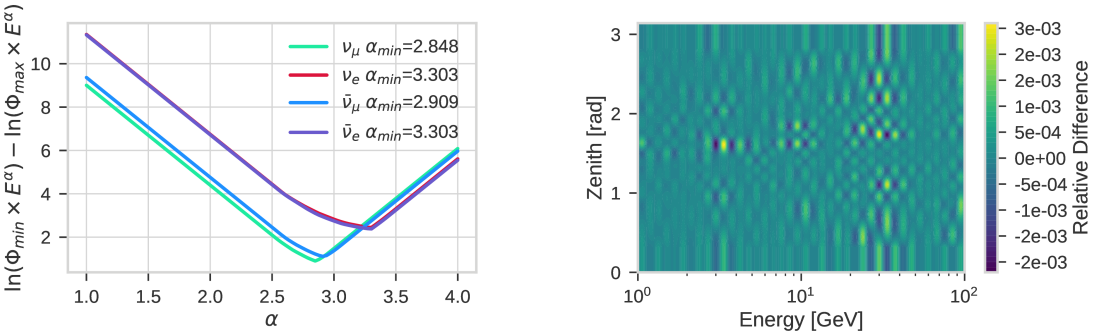

(a) Orders of magnitude in the flattened flux over the spectral index α.

(b) Relative differences of the interpolation with and without the flattening. ($\alpha = 2.85$)

Figure 6.1: Interpolation characterisation using the atmospheric ν_μ flux based on the Frejus data.

6.4 Clouseau

The software package Clouseau was developed by the author and used for analysis of the KM3NeT data. In Figure 6.2 the processing chain structure is shown. The data files are provided as ROOT files, which are first converted to HDF5. This functionality is already provided as command line tool within the `km3pipe` package. The converted files contain the hit information and the full reconstruction information. As it was outlined in Section 6.1 the JFit

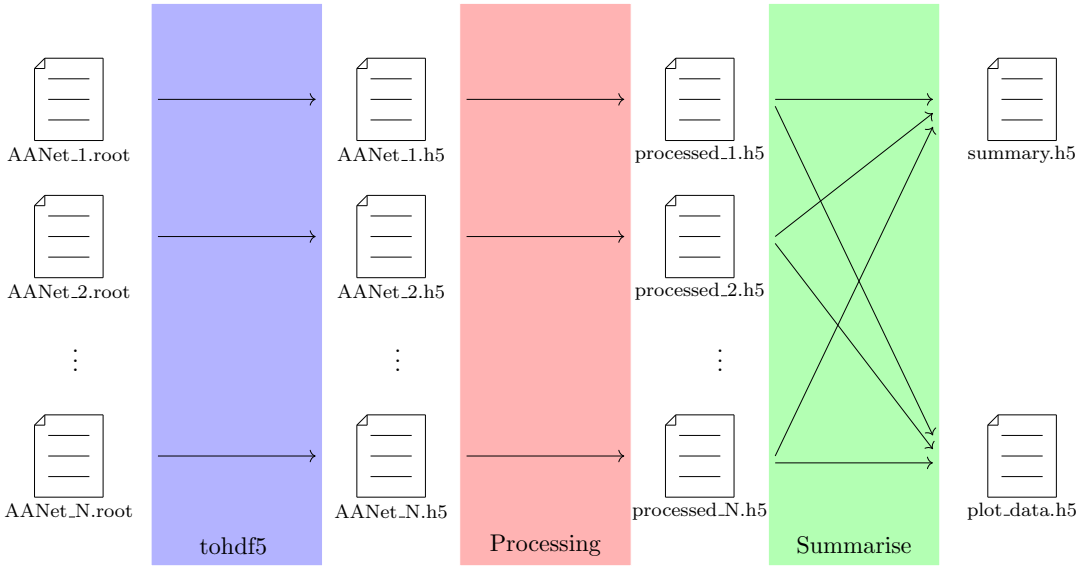

Figure 6.2: Data processing scheme of the clouseau package.

reconstruction result consists of several different reconstruction sequences with multiple results for each event. The processed files contain a new table with specific event features, for those the full file information is required or the resource The table with the JFit reconstructions is kept, but it is reduced to the best result with respect to the likelihood value for each reconstruction chain.

In the summary step, the processes are single threaded and iterate over all processed files as the total number of is required for the normalising the neutrino events. In the `plot_data.h5` single values togetheir with their weight are stored, so these can be binned directly to histograms. The `summary.h5` files contain the best JGandalf reconstruction of with respect to the likelihood,

which are reconstructed as upgoing. It is stored together with the extracted features in a single file. Thus, this can be used to get a fast a access to the data and to develop the selection cuts.

6.5 StrangeLove

In order to process detector data from the ANTARES experiment for the application of the IFT methods, the development of the python module named `strangelove` was initiated by the author. It consists of general modules within the data processing environment of km3pipe to read the *AntDST* data file format. These AntDST files are basically ROOT-files, with a specific internal data structure.
The usage of the km3pipe environment also provides an easy possibility to convert the AntDST files into HDF5 file format, which is shown in Listing 6.1.

```
1  import km3pipe as kp
2  from strangelove.io import AntaresPump
3
4  pipe = kp.Pipeline()
5  pipe.attach(AntaresPump, filenames=['AntDST1.root', 'AntDST2.root'])
6  pipe.attach(kp.io.HDF5Sink, filename='output.h5')
7  pipe.drain()
```

Listing 6.1: Exemple code for the usage of the AntaresPump for processesing AntDST files using a km3pipe based pipeline.

Additionally to the main branch for common usage, the repository also contains the IFT code in the branch "ift". An overview about the main components in the IFT branch of `strangelove` is given in the Table 6.1.

Element	Package Location	Description
Generic components		
↳ ANTARES	`strangelove/antares.py`	ANTARES related methods
↳ IFT	`strangelove/ift.py`	IFT related methods
Skymap Notebook	`notebooks/Skymap.ipynb`	Detailed setup of the skymap script split up in several steps
Skymap Script	`scripts/skymap/skymap.py`	Integrated script for HPC usage
Sky Config	`scripts/skymap/sky_fields.toml`	Hyper-prior configuration for the sky fields
Energy Config	`scripts/skymap/energy_fields.toml`	Hyper-prior configuration for the energy fields

Table 6.1: Overview of IFT relevant components and modules in the `strangelove` package.

6.6 NIFTy

The NIFTy (**N**umerical **I**nformation **F**ield **T**heor**y**) package contains the numerical tools for applying the concepts of IFT (see Chapter 4) to measurement data. This package has been developed by the group of Torsten Enßlin and can be downloaded at [31].

6.6.1 Kullback Leibler Minimisation

A crucial point for the application of the IFT framework to data is the numerical minimisation of the Kullback-Leibler (KL) divergence, which was theoretically outlined in Section 4. The gradient of the KL divergence based on a Gaussian approximate distribution, which was given

in Equation (4.17), is evaluated using sampling methods. The reduced expression for the KL given in Equation (4.16) is hereby evaluated by calculating the arithmetic mean of the posterior at multiple signal positions around the current mean $\bar{s}$, meaning

$$\langle \mathcal{H}(d,s) \rangle_{\mathcal{G}(\bar{s}-s,\Theta)} \approx \frac{1}{N} \sum_{i=1}^{N} \mathcal{H}(d, \bar{s} + \Delta s_i)\,. \tag{6.2}$$

The gradient is hereby calculated by evaluating Equation (6.2) at different positions as a function of $\bar{s}$. The minimisation algorithm consists of the following steps, which are iterated several times:

1. Pick a predefined number of samples $\{\Delta s_i\}$, which is technically done by sampling the fields $\xi_f \curvearrowleft \mathcal{G}(\bar{\xi}, \mathbb{1})$, $\zeta_f \curvearrowleft \mathcal{G}(\bar{\zeta}, \mathbb{1})$ according to the reparametrisation
2. Apply Newton minimiser with respect to $\bar{s}$ to find a new mean position
3. Store the new mean position $\bar{s}$ and repeat these steps to gain new samples around the updated mean position

An important remark concerning the memory usage of the chosen samples: the samples $\{\Delta s_i\}$ are also fields defined on the same base space like the signal field s. For numerical purposes those fields are discretised to a grid, where every mapped value has to be kept in the memory. Additionally to the input data, the mean of the signal s and the samples $\{\Delta s_i\}$, which are each of the size $|\{f|f \in s\}| \times \text{size}(d)$ also have to be stored in the memory. Thus, the grid size has to be reasonably chosen, so that enough resources are available to store the samples in the memory during computation.

Part II

Investigations on first KM3NeT/ORCA detector data

In this part the investigations for the data from the first deployed ORCA detection units (DUs) is presented. Within the work on this thesis reconstrunction on data and monte-carlo simulations for a one and two DU was fully available. Those are analysed with respect to the reconstruction quality and first neutrino candidates are identified.

7 Single Detection Unit Setup

In this chapter the data measured with one DU is analysed. As a single DOM is already sufficient to measure atmospheric muons [32] on a statistical basis, it is obvious to use this minimal detector configuration of a single DU for selecting first neutrino like events also referred as neutrino candidates. The main challenge of a single DU setup is the one dimensional distribution of the instrumentation. This leads to a limited geometrical resolution of the photo sensors for the emitted light distribution close to the DU. For this reason it was focused on the JFit reconstruction (see Section 6.1), because track-like events as they emit a light structure with a larger extent boosted in a certain direction.
The aim of this study is to find these neutrino candidates using different event selection strategies.
In order to develop those, Monte Carlo simulations of atmospheric muons and neutrinos are used for comparison and interpretation of the measurement data. The run selections and the associated livetimes of the used reconstruction versions are listed in Appendix A.1.

7.1 Initial Reconstruction Distribution

The selection of neutrino candidates is limited to events which are propagating in upward direction through the instrumented volume. Those are so-called upgoing events and should only appear for particles resulting from a neutrino interaction. This is due to the earth being a sufficient shield for other high energetic particles, which could emit Čherenkov light. Thus, the track direction with respect to the zenith represents one important reconstruction parameter. It is given for measured data and associated Monte Carlo simulations of this configuration in Figure 7.1.
The reconstructed zenith distribution of the Monte Carlo simulation of atmospheric muons shows a contribution in the upgoing regime $\cos\theta < 0$. Those reconstruction results are misreconstructed muons, which are occurring because of the limited spatial distribution of the optical modules along one axis.
The signal to background ratio based on Monte Carlo data in the upgoing regime ($\cos(\theta) < 0$) is $S/B = 1.75 \times 10^{-3}$. Thus, a selection strategy for suppressing the misreconstructed muon events and other background events is required to extract neutrino candidates from the data.

7.2 Preceding Analysis

The starting point for the neutrino selection from the KM3NeT/ORCA data, is the selection, developed by Dmitry Zaborov [33]. The new and independent python based analysis by the author (see Section 6.4) was used to reproduce those results first. Thus, an independent review of the results was gained, while it also was used for testing purposes of the new software.
The used selection features are given including the applied limits in Table 7.1. Additionally to those selection features a precut has been applied, which requires at least one solution for JPrefit, JSimplex, JGandalf and JStart for an event. It was also required for the different reconstruction results to be sorted in decreasing order with respect to the likelihood.

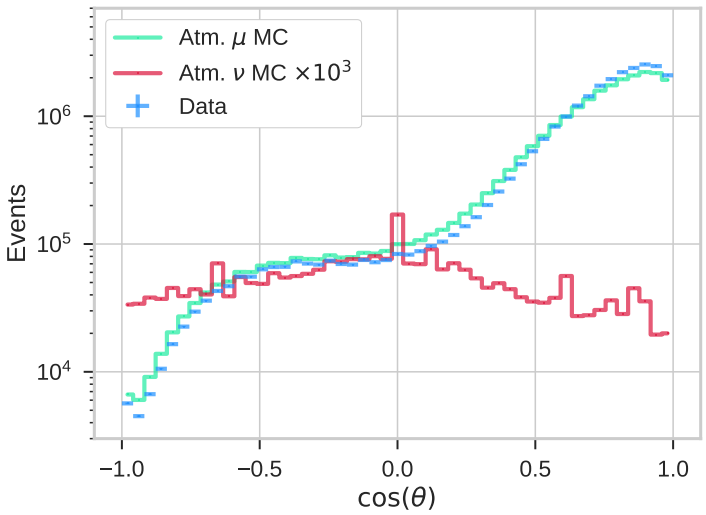

Figure 7.1: Zenith distribution as the cosine of the best JGandalf reconstruction with respect to the likelihood value for measurement and Monte Carlo (v5.8) data. In order to provide a comparison to the expected distribution, the reconstruction results for the Monte Carlo simulations of atmospheric neutrinos (red) and muons (green) are provided in addition to the results for the detector data (blue).

Features	**Limit**	**Eased**	**Description**
$\cos(\theta)$	< -0.5	-	Cosine of the reconstructed track zenith
$\langle z_{\text{triggered}} \rangle$	$> 40\,\text{m}$	$> 30\,\text{m}$	Mean z coordinate of the triggered hits
r_{vertex}	$< 20\,\text{m}$	$< 30\,\text{m}$	Radial distance from the DU of the reconstructed vertex position
down-mask	$\{1, 3\}$	$\{1, 3, 5\}$	Flags which reconstruction step has at least one downgoing solution (1: JPrefit, 2: JSimplex, 4: JGandalf)
$\mathcal{L}_{\text{up}}$	> 40	> 30	Best likelihood value of the upgoing JGandalf reconstructions
$\max(\mathcal{L}_{\text{up}}) - \max(\mathcal{L}_{\text{down}})$	> 15	> 10	Difference between the best JPrefit upgoing and down-going solution with respect to the likelihood value
$\text{first}(t_{\text{ToT}})$	$< 50\,\text{ns}$	$< 150\,\text{ns}$	Time-over-threshold (ToT) value of the first triggered hit
$\max(t_{\text{ToT}})$	$< 70\,\text{ns}$	$< 150\,\text{ns}$	Maximum ToT value of the triggered hits
$\Lambda_{\text{JGandalf}}$	< 100	-	JGandalf quality parameter
β_0	< 0.1	-	JGandalf quality parameter on the angular precision

Table 7.1: Overview of the used selection features and limiting values within the selection developed by D. Zaborov [33]. Given are also loosened limits which were applied to infer the individual dependencies with respect to the absolute selection.

In order to get a better match of Monte Carlo simulation results with respect to the vertical coordinates, the reference point was set to the lowest DOM of the DU. The results of the selection based on the identical run selection for the reconstruction version v0.3 and v5.8 are given in Table 7.2.

Type	$\cos\theta < -0.5$			$\cos\theta < 0$		
Reco. Version	v0.3		v5.8	v0.3		v5.8
Measurement	15 ± 3.9	(10)	11 ± 3.3	21 ± 4.6	(13)	18 ± 4.2
Atmospheric Muon MC	0	(0)	2.55	1.05	(1)	6.12
Atmospheric Neutrino MC	13.86	(7.36)	16.8	15.82	(8.33)	19.5
↳ ν_μ CC	9.08	(4.89)	13.1	10.13	(5.44)	15.1
↳ ν_e CC	2.41	(1.17)	1.68	2.84	(1.36)	1.96
↳ ν_τ CC	1.38	(0.83)	1.01	1.64	(0.96)	1.23
↳ ν NC	0.99	(0.47)	1.01	1.22	(0.57)	1.21

Table 7.2: Resulting number of events based on the used reconstruction versions and the run selection. In brackets the results of the original analysis for direct comparison are given [33]. The Poissonian errors are given for the measured data.

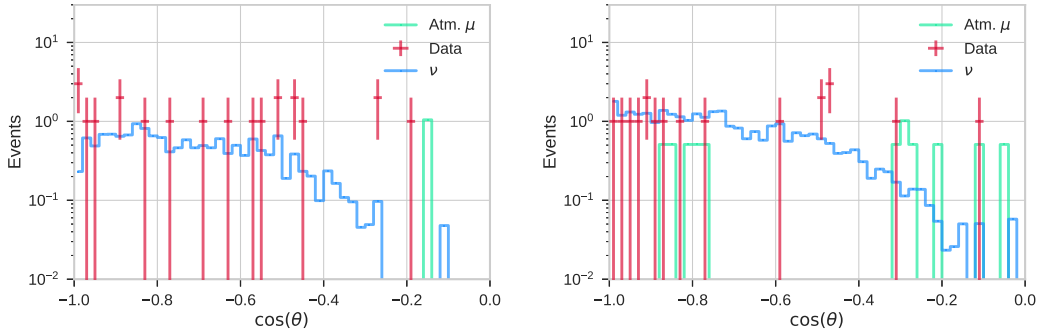

Figure 7.2: Final zenith distribution for both used reconstruction versions 0.3 (left) and 5.8 (right).

The results of this study for the same configuration and reconstruction version v0.3 like in the analysis [33] show a higher number of events for data and neutrino Monte Carlo. The vertical hit positions over time, so-called event displays, of the additional measured events using version v0.3 within this study by the author are shown in Figure 7.3.
The first event from run 2441 can be identified as an atmospheric muon, because of the large number of hits on the upper part of the DU and a downgoing hit pattern. The upgoing reconstruction is caused by a partial hit selection. To cover this phenomenon by a selection feature, the ratio of used hits for the reconstruction and the total number of hits is studied in Section 7.4. The events from run 2609 and 3201 show a perfect upgoing pattern both having a hit aligned with the arrival time hypothesis of the light at the lowest DOM. Thus, those events can also be caused by an atmospheric muon passing horizontally below the DU. The event in run 3035 is kept as neutrino candidate.
It is assumed that those events have been removed in [33] after checking by eye.
When the same configuration was applied using the reconstruction version v5.8, the number of measured events decreases, whereas 4 events are not contained within the measured events passing the cuts using v0.3. Those are shown in Figure 7.4. An overview of all resulting measured events for the selection cuts of [33] is given in Table 7.3. When comparing the Monte Carlo expectations, the number of simulated neutrino events is increased by about a factor of two compared to [33]. Two main differences in the modelling of the neutrino event weights can lead to the deviations from the previous results, which are the used flux and the oscillation model. In this study the Honda flux at scales measured at Frejus in solar minimum taken from

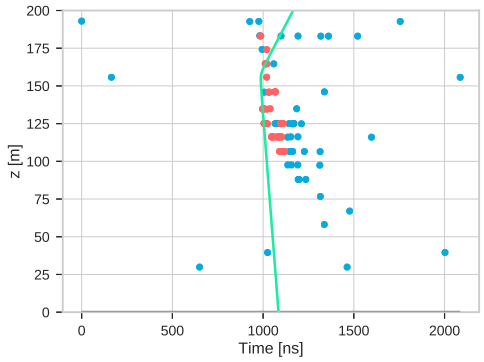

(a) Run-ID: 2441, Event-ID: 16072

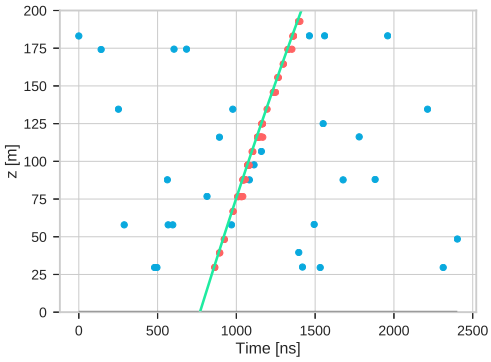

(b) Run-ID: 2609, Event-ID: 3665

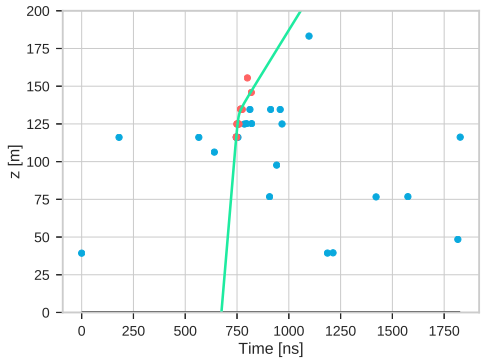

(c) Run-ID: 3035, Event-ID: 17967

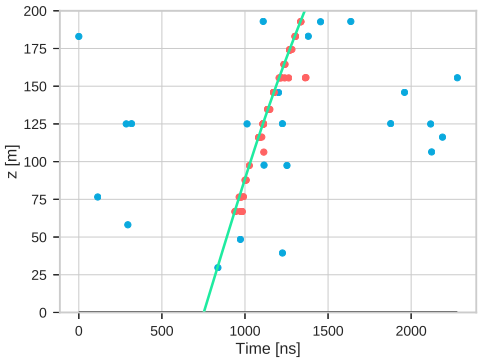

(d) Run-ID: 3201, Event-ID: 13108

Figure 7.3: Event displays for the additionally emerged events for $\cos\theta < -0.5$ in the applied selection cuts. It contains triggered (red) and snapshot hits (blue) and the arrival time hypothesis of the Čherenkov light cone based on the best JGandalf reconstruction (green).

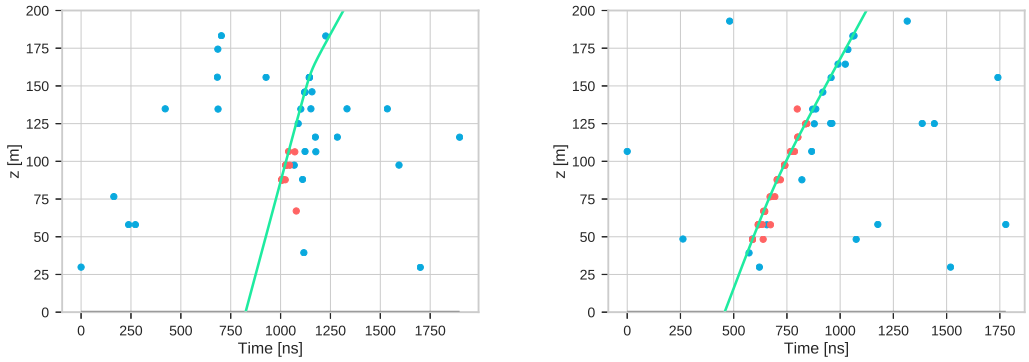

(a) Run-ID: 2627, Event-ID: 14749

(b) Run-ID: 2690, Event-ID: 15083

(c) Run-ID: 2889, Event-ID: 3988

(d) Run-ID: 3177, Event-ID: 13251

Figure 7.4: Event displays for the additionally emerged upgoing ($\cos\theta < 0$) events in the applied selection cuts. It contains triggered (red) and snapshot hits (blue) and the arrival time hypothesis of the Čherenkov light cone based on the best JGandalf reconstruction (green).

Run	**Event Id (v0.3)**	**Event Id (v5.8)**	$\cos\theta$ (v0.3)	$\cos\theta$ (v5.8)
2290	5585	-	0.70	-
2293	210	-	0.62	-
2441	16072	-	0.56	-
2546	9043	-	0.20	-
2555	1353	1353	0.50	0.48
2609	3665	-	0.98	-
2623	5161	-	0.26	-
2627	-	14749	-	0.93
2658	5579	-	1.00	-
2689	20299	20298	0.58	0.58
2690	-	15083	-	0.98
2722	12065	12064	0.83	0.83
2884	14120	14121	0.46	0.47
2889	-	3988	-	0.31
2904	8711	8711	0.88	0.87
2965	13608	13608	0.46	0.48
2973	11163	11161	0.96	0.96
3012	21459	21459	0.97	0.90
3035	17577	17577	0.77	0.77
3035	17967	17967	0.51	0.47
3086	19454	19453	0.89	0.89
3089	11477	11475	0.44	0.48
3174	12158	12158	0.27	0.11
3177	-	13251	-	1.00
3201	13108	-	0.98	-

Table 7.3: Neutrino candidate run and event ids for the preceding selection cuts applied for version 0.3 and 5.8. The event ids are given for both versions, because the data has been retriggered, which can lead to different event numbering within a run. The additional events for version v0.3 (see Figure 7.3) are marked in yellow.

[34] was used. The flavour oscillation model includes all three flavour types, whereas in [33] just a flavour oscillation model including $\{\mu, \tau\}$ is used.
In general the expected numbers from the Monte Carlo simulations lie within a $1\,\sigma$ range for v0.3 and $2\,\sigma$ range for v5.8, based on the Poissonian error of the measured data.
The number of misreconstructed atmospheric muons using v0.3 in both zenith regimes matches the results in [33], whereas for v5.8 the number of muons increases. As the underlying model for atmospheric muons is not changed the numbers of the expected neutrino events is increased by a factor of two compared to [33], the cut features, i.e. the chosen limits, were studied in detail. In order to get comparable final numbers, for each selection feature loosened limits have been defined. Those loosened limits are not chosen with respect to a fixed normalisation, but based on the distributions gained from the basic selection limits. Those loosened limits are also given in Table 7.1 and the resulting events numbers are listed in Table 7.4.

Cut	**Limit**	**observed**		**atm. μ MC**		**atm. ν MC**	
		v0.3	v5.8	v0.3	v5.8	v0.3	v5.8
$\langle z_{\text{triggered}} \rangle$	$> 30\,\text{m}$	27 (20)	19 (11)	1.0 (0)	8.1 (3.6)	17.7 (15.5)	22.1 (19.0)
r_{vertex}	$< 30\,\text{m}$	30 (23)	28 (19)	3.1 (2.1)	18.4 (10.7)	21.3 (17.1)	27.8 (22.7)
$\mathcal{L}_{\text{down}}$-mask	$\{1, 3, 5\}$	36 (21)	23 (15)	3.1 (2.1)	7.7 (3.1)	16.6 (14.4)	20.7 (17.8)
$\mathcal{L}_{\text{up}}$	> 30	26 (18)	21 (11)	3.1 (2.1)	13.8 (5.6)	17.6 (15.1)	21.1 (17.8)
$\mathcal{L}_{\text{up}} - \mathcal{L}_{\text{down}}$	> 10	54 (33)	44 (24)	7.3 (3.13)	32.1 (14.3)	28.9 (22.4)	33.1 (25.2)
t_{ToT}	$< 150\,\text{ns}$	35 (28)	27 (20)	4.2 (3.1)	12.8 (7.7)	17.9 (15.5)	22.6 (19.3)
$\max(t_{\text{ToT}})$	$< 150\,\text{ns}$	28 (21)	22 (15)	2.1 (1.1)	8.2 (4.1)	16.5 (14.5)	20.7 (17.7)

Table 7.4: Number of events using individually loosened limits on the same selection cuts. Given are the total numbers in the upgoing regime $\cos\theta < 0$ and the numbers for $\cos\theta < -0.5$ are given in brackets.

The increase gained based on the geometric features is within the scale of the increase of the target mass, which is for $\langle z_{\text{trg}} \rangle$ about 1.1 and for r_{vtx} about 2.25.
Within the likelihood based features no major increase for the additional downgoing flag configuration 5, i.e. a downgoing solution for the combination of JPrefit and JGandalf is available, is present. For the loosened limit of $\mathcal{L}_{\text{up}} > 30$ no major increase is observed. The largest increase of events is observed for the feature $\mathcal{L}_{\text{up}} - \mathcal{L}_{\text{down}}$, whereas this loosened limit is kept for the final selection (see Section 7.6). This is done in order to avoid a too strong bias via a single feature.
The loosened limits for the time-over-threshold (ToT) values

7.3 Preselection

Based on the preceding analysis a preselection was defined to ensure a basic quality level and comparability. The features and the associated limiting values are listed in Table 7.5.

Cut	**Limit**	**Description**
JGandalf Solution	Available	The event reconstructions have at least one JGandalf solution
$n_{\text{DOM}}^{\text{trg}}$	≥ 3	The event has triggered at least 3 different DOMs
$\max(t_{\text{ToT}}^{\text{trg}})$	< 100	The maximum threshold of a PMT signal is required to be lower than 100 ns

Table 7.5: Feature cut limits for the introduced preselection, which is applied for all custom selections in the following.

The reconstructed JGandalf values are referred to, thus the existence of at least one JGandalf solution for the event is required.
In order to require a sufficient spatial extent of the received light pattern, a minimal number of triggered DOMs is required and set to $n_{\text{DOM}}^{\text{trg}} \geq 3$. In Figure 7.5 the distribution of the number

of triggered DOMs is shown, where it can be seen that the number of events rejected by this preselection cut is small compared to the total number of events.
The ToT value of the PMT signals was limited to a maximum of 100 ns. This selection cut is used to eliminate events at high luminosity, e.g. generated by a PMT itself, so-called sparking PMTs, or by bioluminescence. The value was chosen based on the maximum ToT distribution of the upgoing events, where a local peak at about 170 ns is present.

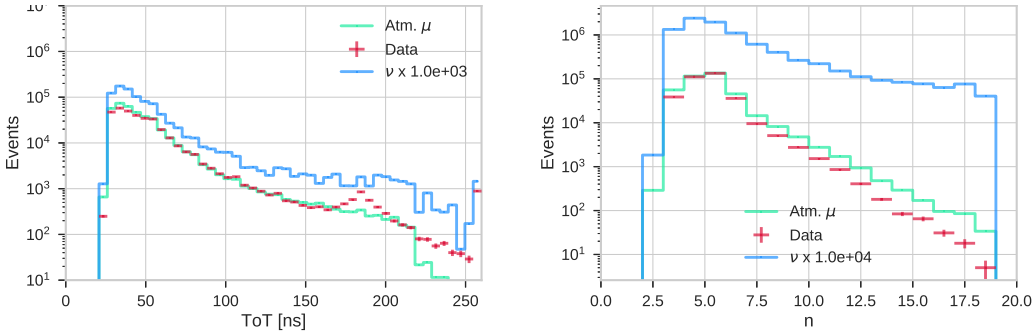

Figure 7.5: Event distributions of the preselection features, i.e. the maximum time-over-threshold (left) and the number of triggered DOMs (right) for upgoing events.

7.4 Geometric Selection

In the geometric selection only features directly related to the detector and event geometry are used. Thus, it is attempted to develop a reasonable candidate selection, neglecting quantities encoding the information about the reconstruction process itself. In Table 7.6 the used features and the chosen limits of this selection are listed. The resulting event numbers are given in Table 7.7 and the associated zenith distribution is given in Figure 7.6.

Selection Cut	Limit	Description
$\langle z_{\text{triggered}} \rangle$	$> 40\,\text{m}$	The mean z coordinate of all triggered hits
r_{vertex}	$< 30\,\text{m}$	The radial distance of the reconstructed vertex position
$n_{10\,\text{ns}}$	> 25	Lower limit of the total number of on-time hits
$R_{\text{On-time}}$	> 0.8	Ratio between on-time hits and hits within a range of $\pm 100\,\text{ns}$ around the best JGandalf hypothesis (see Equation (7.3))

Table 7.6: Feature cut limits for the geometric selection.

In this selection the muon rejection was not optimised in order to limit the number of used features and to avoid applying too strong limits. This is done with respect to the final custom selection, where these features are planned to be part of.
Within the steeper upgoing regime ($\cos\theta < -0.5$) the number of Monte Carlo events are within $0.25\,\sigma$ of the gained number of measured events. In general for the upgoing events this value is at $2.4\,\sigma$.
The geometrical features of the mean vertical position of the triggered hits and the radial distance of the reconstructed vertex from the preceding selection was applied. These features provide a good data Monte Carlo agreement and a certain value range with containing indicators for separating muons and neutrinos.
A large number of misreconstructed muon events have a mean vertical position of triggered hits below 30 m, which is shown in Figure 7.7. The limit has been applied from [33] and set to 40 m. Above this feature value the distribution for the muon Monte Carlo is about to be equally distributed (see Figure 7.7).

Type	$\cos\theta < -0.5$	$\cos\theta < 0$
Measurement	102 ± 10.1	235 ± 15.3
Atmospheric Muon MC	54.2	164.6
Atmospheric Neutrino MC	45.2	107.4
↳ ν_μ CC	37.7	69.6
↳ ν_e CC	3.4	9.8
↳ ν_τ CC	2.2	3.2
↳ ν NC	2.0	5.4

Table 7.7: Resulting number of events for the geometric selection. The Poissonian errors are given for the measured data numbers.

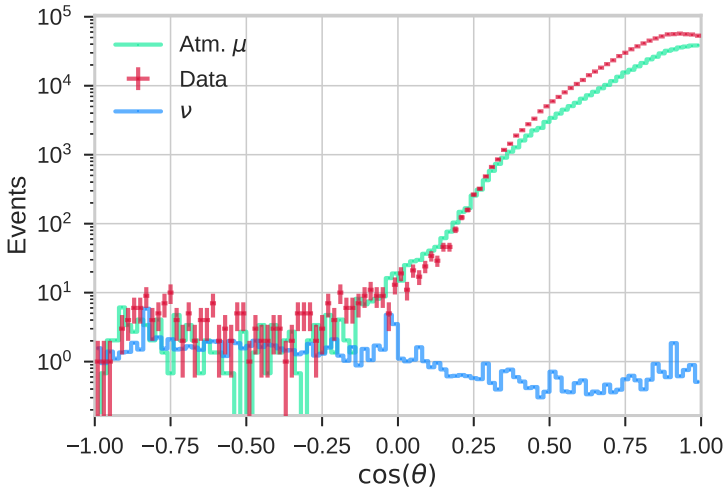

Figure 7.6: Zenith distribution as cosine of the best JGandalf reconstruction.

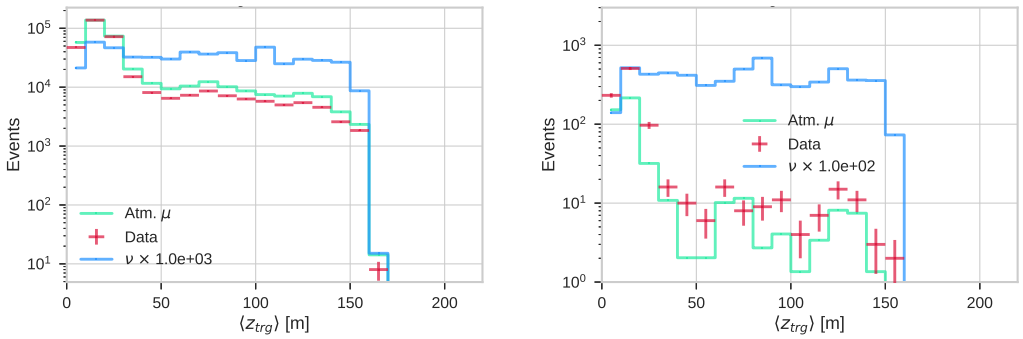

Figure 7.7: Distribution of the mean vertical position of the triggered hits for upgoing events (left) and for the event selection (right).

For the radial distance of the reconstructed vertex to the line the number of neutrinos is increased for values smaller than 30 m, whereas the number of muons is decreased (see Figure 7.8).

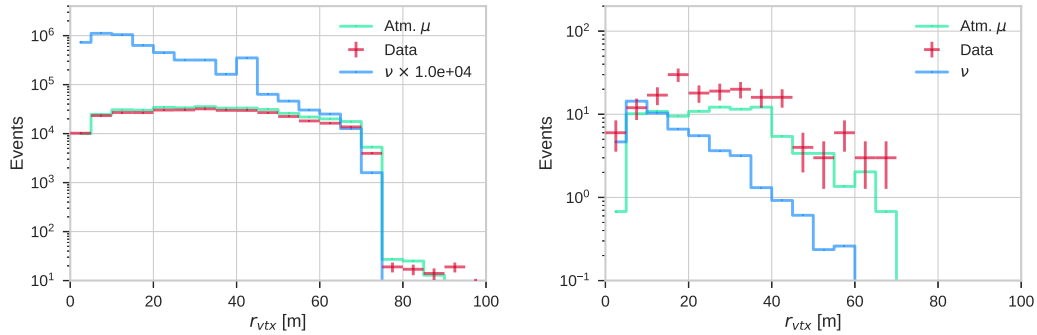

Figure 7.8: Distribution of the radial distance of the DU to the reconstructed vertex position for upgoing events (left) and for the event selection (right).

7.4.1 Time Residuals

The time residual of one photon event measured at the PMT (hit) is defined as the time difference between the actual time of the hit signal and the expected time of the Čherenkov light cone to reach the PMT based on the reconstructed track parameters. In Figure 7.9 the

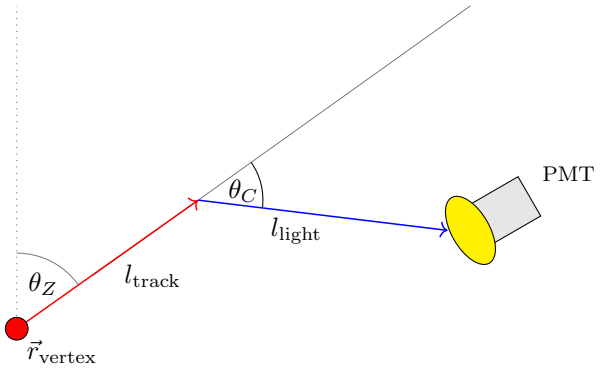

Figure 7.9: Schematic drawing of the path lengths used for calculating the time residuals.

geometry of the paths based on the track hypothesis based on the Čherenkov cone structure (see Figure 5.1) is given. The time residual t_{res} for an individual hit is given by

$$t_{\text{res}} = (t_{\text{hit}} - t_0) - \left(\frac{l_{\text{track}}}{c} + \frac{n_{\text{sea}}\, l_{\text{light}}}{c} \right) , \tag{7.1}$$

where t_{hit} is the time of the hit and t_0 being the reconstructed time of the neutrino interaction. The lengths l_{track} and l_{light} are the paths of the particle emitting the Čherenkov light and the emitted Čherenkov photon. The refractive index in the sea water is given by $n_{\text{sea}} = 1.3499$. The time residuals represent an individual parameter for each hit, which differs for each event. In order to extract a single quantity characterising the event, the number of hits $n_{t_{\text{res}}}$ with a time residual within a certain range is determined for each event. The limits were set to

$$t_{\text{lim}} \in \{10\,\text{ns}, 20\,\text{ns}, 30\,\text{ns}, 50\,\text{ns}, 100\,\text{ns}, 150\,\text{ns}, 200\,\text{ns}\} . \tag{7.2}$$

The hits close within a 10 ns time difference to the expected timing according to the track hypothesis are called on-time hits in the following. In Figure 7.10 a correlation plot of on-time

hits and the likelihood of the best upgoing JGandalf reconstruction is shown. Based on this relation the $\mathcal{L}_{\text{up}}$ cut was replaced in this selection by the requirement of each event having more than 25 on-time hits.

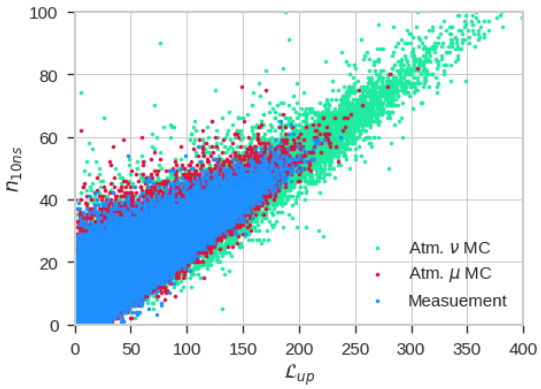

Figure 7.10: Correlation plot for the number of on-time hits and the likelihood value of the best upgoing JGandalf reconstruction for measured events and Monte Carlo simulations.

The first derived parameter based on the number of hits within a certain time residual range is

$$R_{\text{On-time}} = \frac{n_{10\,\text{ns}}}{n_{100\,\text{ns}}}\,, \tag{7.3}$$

which expresses the ratio between on-time hits and the remaining hits received in a reasonable timespan of $\pm 100\,\text{ns}$ around the expectation. The main idea about this feature is to cover misreconstruction based on an inconvenient hit selection, which was observed in Figure 7.3a. The value in this example is $R_{\text{On-time}} = 0.39$. The distributions for this feature are shown in Figure 7.11. The numbers for neutrino events is increasing above $R_{\text{On-time}} > 0.6$ and

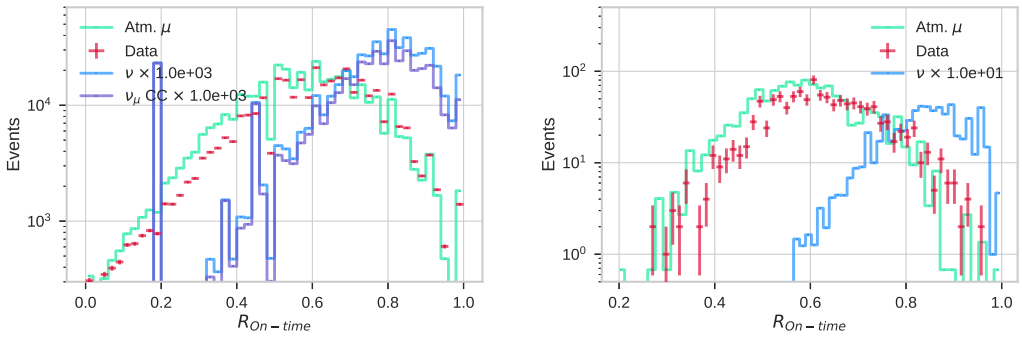

Figure 7.11: Distribution of the parameter $R_{\text{On-time}}$ defined in Equation (7.3) for all upgoing events before (left) and after the event selection (right).

in combination with the selection cuts the muon and neutrino Monte Carlo show two well separated peaks. Thus, this feature was used for the selection, requiring $R_{\text{On-time}} > 0.8$.
Another approach for a feature to tackle the hit selection problem is the ratio of the number of event hits used in the best JGandalf reconstruction n_{JGandalf} and the number of on-time hits, which is given by

$$R_{\text{JG}} = \frac{n_{\text{JGandalf}}}{n_{10\,\text{ns}}}\,. \tag{7.4}$$

where n_{JGandalf} is the number of hits used by the JGandalf reconstruction. The distributions for this feature are shown in Figure 7.12. The distribution for the upgoing events shows an edge at $R_{\text{JG}} = 1$, which is expected, as the hit selection should at least consist of the on-time hits.

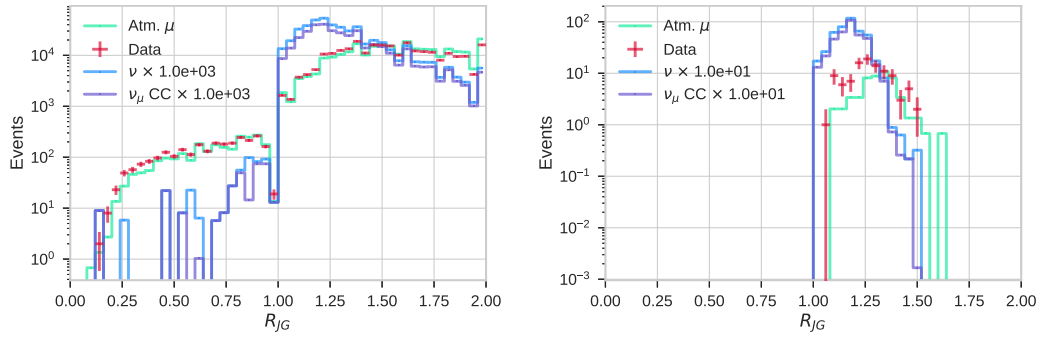

Figure 7.12: Distribution of the parameter R_{JG} defined in Equation (7.3) for all upgoing events before (left) and after the event selection (right).

This feature also shows a good data Monte Carlo agreement with respect to the atmospheric muon expectation.
For the final geometric selection, this feature is neglected, because of a missing significant separation after applying the selection cuts.

7.5 Quality Selection

Complementary to the approach of selecting neutrino candidates exclusively based on geometric features, it is also attempted to get a reasonable selection based on reconstruction quality parameters. This is mainly composed out of features based on the likelihood value, listed in Table 7.8.

Selection Cut	**Limit**	**Description**
$\max(\mathcal{L})/n_{\mathrm{DoF}}$	> 2.8	Likelihood divided by the number of degrees of freedom
$\max(\mathcal{L}_{\mathrm{up}})$	> 100	Best likelihood value for a JGandalf upgoing solution
$\max(\mathcal{L}_{\mathrm{up}}) - \max(\mathcal{L}_{\mathrm{down}})$	> 20	Difference between the best JPrefit up-going and down-going solution with respect to the likelihood value
$\Lambda_{\mathrm{JGandalf}}$	< 100	Additional quality parameter of JMuon reconstruction chain
down-mask	$\{1\}$	Flags which reconstruction step has at least one down-going solution, which requires here just JPrefit to have a downgoing solution. (1: JPrefit, 2: JSimplex, 4: JGandalf)

Table 7.8: Selection features and cut limits for a selection based only on quality parameters.

The resulting numbers are given in Table 7.9. Within this selection the numbers of the measured events and the Monte Carlo prediction disagree by at least $2\,\sigma$ for both considered zenith

Type	$\cos\theta < -0.5$	$\cos\theta < 0$
Measurement	21 ± 4.6	34 ± 5.8
Atmospheric Muon MC	6.8	25.7
Atmospheric Neutrino MC	28.0	32.4
↳ ν_μ CC	24.6	27.3
↳ ν_e CC	1.5	2.2
↳ ν_τ CC	0.9	1.1
↳ ν NC	0.9	1.7

Table 7.9: Resulting number of events for the quality selection. The Poissonian errors are given for the measured data numbers.

regimes with respect to the Poissonian error of the measured event numbers. Within the zenith angle distribution (see Figure 7.13) an increase of the expected neutrinos based on the Monte Carlo simulation towards the zenith in the upgoing regime is present.

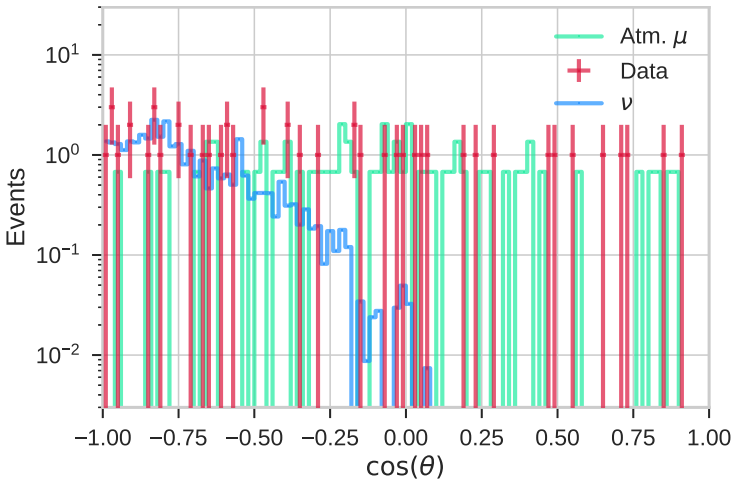

Figure 7.13: Zenith distribution given in terms of the cosine for the best JGandalf reconstruction with respect to the likelihood value for measurement and Monte Carlo (v5.8) data. In order to provide a comparison to the expected distribution, the reconstruction results for the Monte Carlo simulations are provided additionally to the results for the detector data.

The distributions of the likelihood over the number of degrees of freedom n_{DoF} is shown in Figure 7.14. The number of degrees of freedom is given by the used number of hits for the reconstruction minus the number of reconstructed parameters. The number of reconstructed parameters is 5 for JGandalf, i.e. the three components of the track direction and two components of to fix the track position at an artificial receptor point.
The distribution of the neutrino Monte Carlo predicts a peak at $\max(\mathcal{L})/n_{\mathrm{DoF}} > 3$, which is well separated from the peak in the muon Monte Carlo distribution at $\max(\mathcal{L})/n_{\mathrm{DoF}} \approx 2.5$. In the data distribution only a small shift of the peak compared to the muon Monte Carlo is present, which is mostly caused by smaller feature values of data in the regime $\max(\mathcal{L})/n_{\mathrm{DoF}} < 2$. Apart from this deviation the feature distribution for data and muon Monte Carlo agrees.
After applying the selection cuts, the separation of the peaks in the distributions for muon and neutrino Monte Carlo has diverged. In the regime $\max(\mathcal{L})/n_{\mathrm{DoF}} < 3$ the data is overestimated by the muon Monte Carlo, but the transition to the regime where the neutrino events are dominant is also visible in the data distribution. Thus, the limit has been set to $\max(\mathcal{L})/n_{\mathrm{DoF}} > 2.8$, which is the position the neutrino distribution exceeds the muon distribution.
In Figure 7.15 the distribution for the best upgoing likelihood of the JGandalf reconstruction $\mathcal{L}_{\mathrm{Up}}$ is shown. The peak for neutrinos is shifted to $\mathcal{L}_{\mathrm{Up}} > 40$ after the applied selection. The limit was raised to $\mathcal{L}_{\mathrm{Up}} > 100$, because at this feature value the neutrino Monte Carlo distribution exceeds the muon Monte Carlo distribution. The difference between the best likelihood of the best up- and downgoing JPrefit reconstruction is required to be $\mathcal{L}_{\mathrm{Up}} - \mathcal{L}_{\mathrm{Down}} > 15$, because at this point the expectation by neutrino Monte Carlo exceeds the expectation by the muon Monte Carlo after applying the selection cuts.
The event number for misreconstructed muons is monotonically increasing for increasing $\Lambda_{\mathrm{JGandalf}}$. The event number for neutrinos has a peak at $\Lambda_{\mathrm{JGandalf}} = 1$. Based on this knowledge about the initial distribution the events at $\Lambda_{\mathrm{JGandalf}} > 100$ are rejected, which excludes two muon events in the selection (see Figure 7.17).
The final cut of this quality selection is the mask, which flags the reconstruction stages whether a downgoing solution for an event is present. JPrefit uses a regular grid for the starting values,

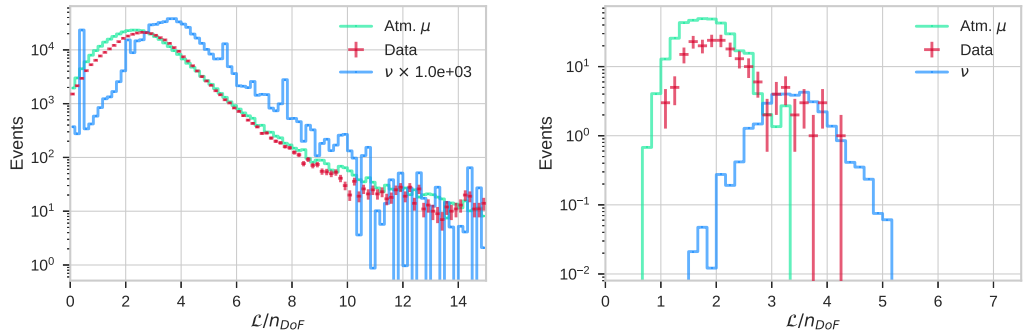

Figure 7.14: Distribution of the observable $\mathcal{L}/n_{\mathrm{DoF}}$ for all upgoing events before (left) and after the event selection (right).

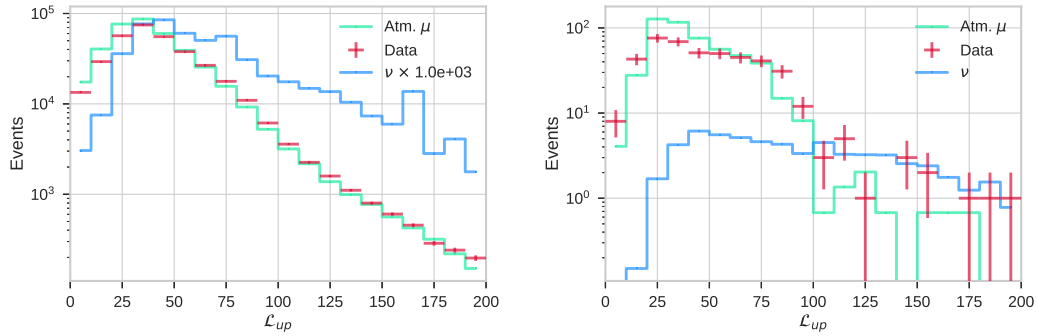

Figure 7.15: Distribution of the observable $\mathcal{L}_{\mathrm{Up}}$ for all upgoing events before (left) and after the event selection (right).

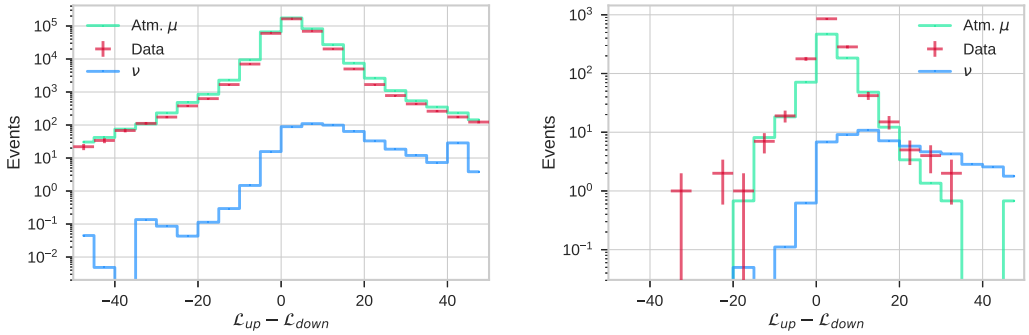

Figure 7.16: Distribution of the observable $\mathcal{L}_{\mathrm{Up}} - \mathcal{L}_{\mathrm{Down}}$ for all upgoing events before (left) and after the event selection (right).

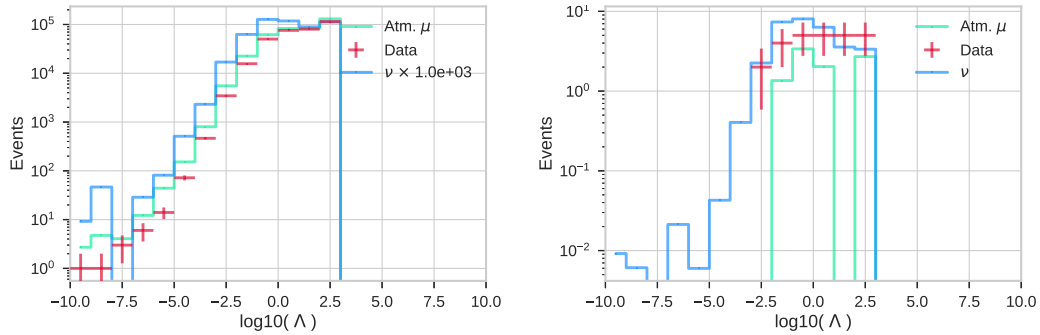

Figure 7.17: Distribution of the observable $\Lambda_{\mathrm{JGandalf}}$ for all upgoing events before (left) and after the event selection (right).

which makes this stage the one that most likely has a downgoing solution. The associated mask value is 1, which is has also the most events and the best neutrino to muon ratio, according to the distribution given in Figure 7.18. Thus, this feature it is required to be one.

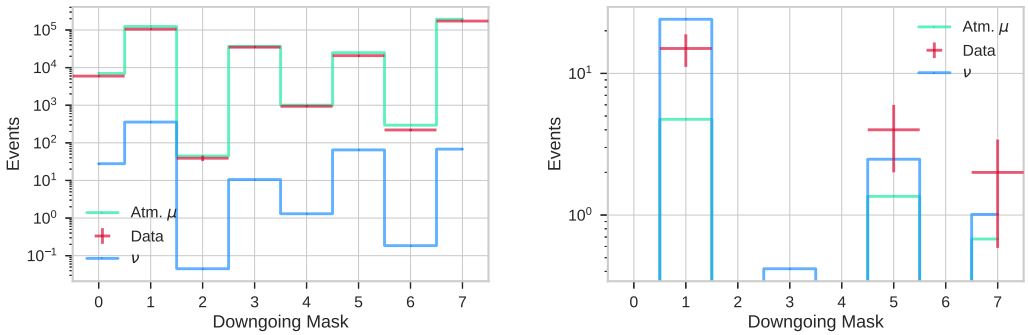

Figure 7.18: Distribution of the mask indicating the reconstruction stages of JFit (see Section 6.1), which contain a downgoing solution, for all upgoing events before (left) and after the event selection (right).

7.6 Custom Selection

Finally, a custom selection using both types of features was created. The used features and the associated limits are listed in Table 7.10. The resulting event numbers are given in Table

Selection Cut	Limit	Description
$\langle z_{\text{triggered}} \rangle$	$> 30\,\text{m}$	The mean z coordinate of all triggered hits
r_{vertex}	$< 30\,\text{m}$	The radial distance of the reconstructed vertex position.
$R_{\text{On-time}}$	> 0.7	Ratio between on-time hits and hits within a range of $\pm 100\,\text{ns}$ around the best JGandalf hypothesis (see Equation (7.3))
$\max(\mathcal{L})/n_{\text{DoF}}$	> 1.9	Likelihood divided by the number of degrees of freedom
$\max(\mathcal{L}_{\text{up}})$	> 80	Best likelihood value for a JGandalf upgoing solution
$\max(\mathcal{L}_{\text{up}}) - \max(\mathcal{L}_{\text{down}})$	> 10	Difference between the best JPrefit up-going and down-going solution with respect to the likelihood value

Table 7.10: Selection features and cut limits for the custom selection based on both types of parameters.

7.11 and the associated zenith distribution is given in Figure 7.19. The muon rejection for the angular regime close to the horizon, i.e. $\cos\theta \in [-0.5, 0]$, has only a signal to background ratio in the Monte Carlo prediction of $S/B = 2.63$ and the number of measured events is about $3\,\sigma$ smaller than the combined number of Monte Carlo events.
As it is focused on the steeper upgoing regime, the signal to background ratio is here $S/B = 7.97$ and the deviation between data events and Monte Carlo is only $1.7\,\sigma$. This selection yields an event rate of $\nu = 0.4\,\text{d}^{-1}$, which exceeds the $\nu = 0.13\,\text{d}^{-1}$ of the preceding analysis (see Section 7.2). In Figure 7.20 the features used for the geometrical selection (see Section 7.4) are shown. The mean vertical position of the triggered hits shows the first muon event at $\langle z_{\text{trg}} \rangle > 40\,\text{m}$ and a good agreement of data to the neutrino Monte Carlo in this regime. Thus, the cut on this feature is removed.
For the radial distance of the reconstructed vertex to the DU, the contribution of misreconstructed muons at larger distances is still present. The upper limit is applied from the geometrical selection at 30 m, which could have been loosened as the expected neutrino contribution is expected to be still higher than for the muons. This conservative choice is also done in order to use this feature to select events with a clear light pattern, because this distances are already

Type	$\cos\theta < -0.5$	$\cos\theta < 0$
Measurement	52 ± 7.2	75 ± 8.5
Atmospheric Muon MC	5.4	16.3
Atmospheric Neutrino MC	55.8	70.7
↳ ν_μ CC	48.2	58.8
↳ ν_e CC	3.3	5.3
↳ ν_τ CC	2.2	2.9
↳ ν NC	2.1	3.7

Table 7.11: Resulting number of events for the custom selection. The Poissonian errors are given for the measured data.

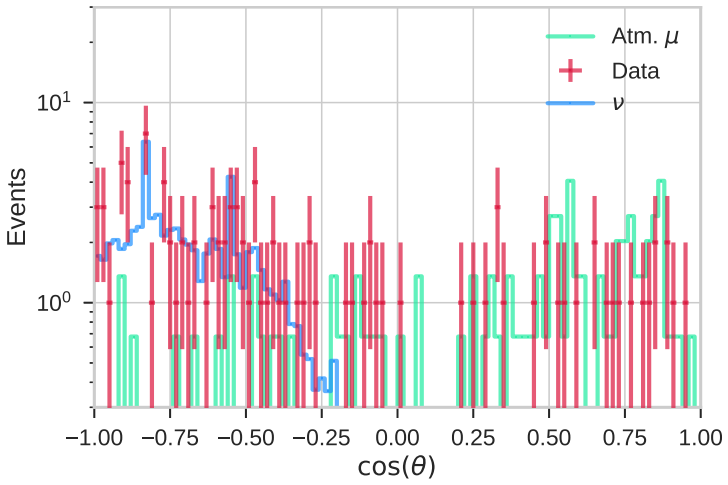

Figure 7.19: Zenith distribution given as cosine of the best JGandalf reconstruction with respect to the likelihood value for measurement and Monte Carlo (v5.8) data. In order to provide a comparison to the expected distribution, the reconstruction results for the Monte Carlo simulations are provided additional to the results for the detector data.

in the order of magnitude of the absorption length in water. and the radial distance of the reconstructed vertex. The distributions for the number of on time hits and the ratio $R_{\text{On-time}}$ do not show well separated shapes for neutrino and muon Monte Carlo in this selection. Thus, those are also left out for this selection.

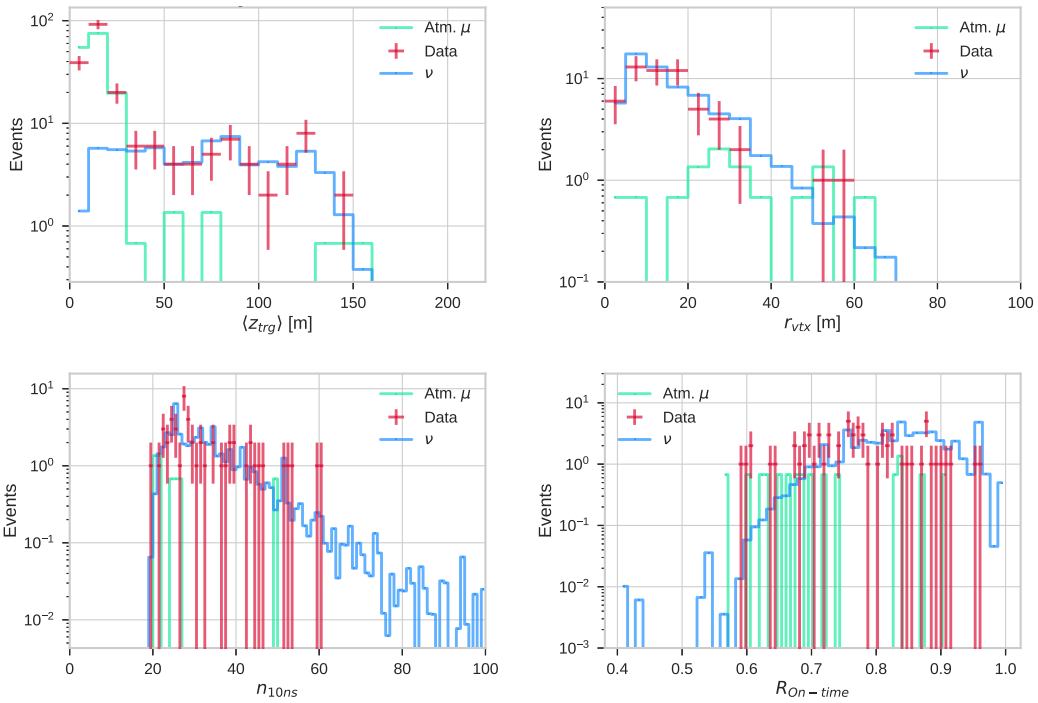

Figure 7.20: Distribution of the geometrical features used within the geometric selection after appling the custom selection cuts (see Section 7.4).

In Figure 7.21 the features used for the quality selection (see Section 7.5) are shown.
The distribution of the best JGandalf likelihood over the number of degrees of freedom feature shows two well separated peaks, which are also present in data. Thus, this feature is kept and the limit was loosened to $\mathcal{L}/n_{\text{DoF}} > 1.9$.
The parameter $\mathcal{L}_{\text{Up}} - \mathcal{L}_{\text{Down}}$ is required to be larger than 10, because at this point the expectation by neutrino Monte Carlo events exceeds the expectation of the muons.
In the same way the cut value of the feature of the best likelihood of an upgoing JGandalf reconstruction is chosen, which is set to $\mathcal{L}_{\text{Up}} > 80$. The distribution of the parameter $\Lambda_{JGandalf}$ shows a constant background in the regime $\left[10^{-3}, 10^{3}\right]$ and therefore no dominant muon regime can be rejected by this feature. The data also describes the neutrino Monte Carlo and thus no cut on this parameter was applied.

7.7 Final Comparison

In order to merge the results from this chapter, i.e. the different selections, the resulting events now should be compared. The custom selection and the preceding selection are based on a different run selection. Thus, the final comparable overview is given in terms of the detection rates, which are given in Table 7.12.
When comparing the neutrino candidate rates of the custom selection to those of the preceding selection, they are larger by about a factor of two. The downside of this increase is the expected rate of muons based on the Monte Carlo simulations. The overall muon rate in the upgoing regime of the custom selection is larger by a factor of 15. This also becomes apparent when checking the associated event displays by eye.

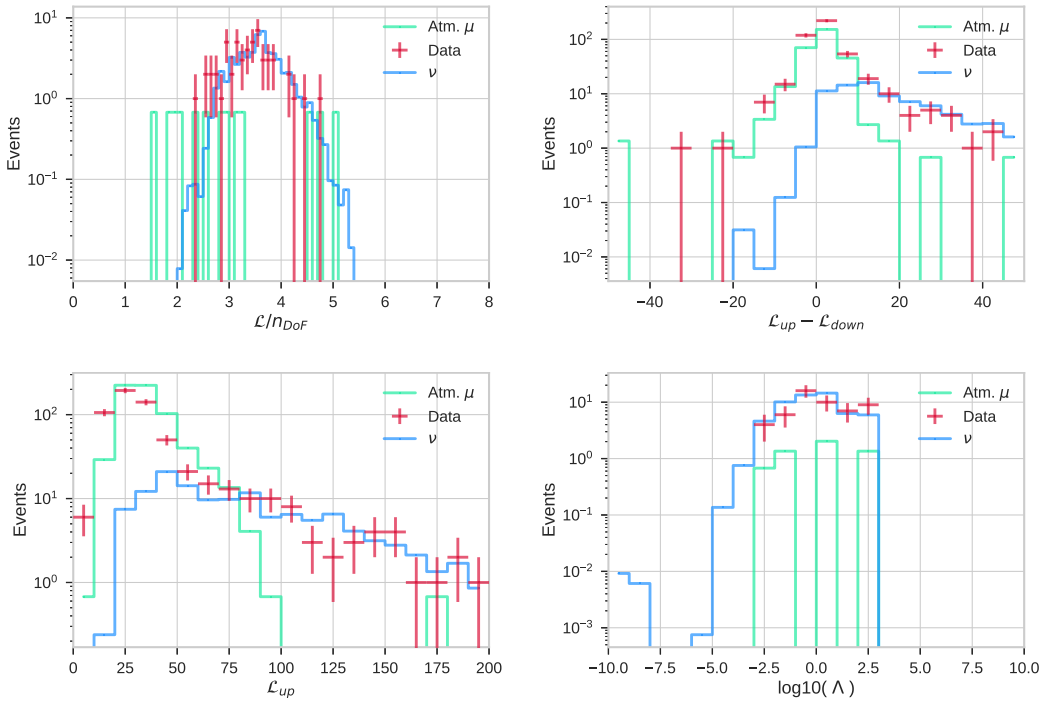

Figure 7.21: Distribution of the quality features used within the quality selection after applying the custom selection cuts (see Section 7.5).

Type	**Neutrino Candidate** [s^{-1}]	**Muon Monte Carlo** [s^{-1}]
Preceding		
↳ $\cos\theta \in [-1, 0]$	$0.24 \pm 5.6 \times 10^{-2}$	8.18×10^{-2}
↳ $\cos\theta \in [-1, -0.5]$	$0.15 \pm 4.4 \times 10^{-2}$	3.41×10^{-2}
Custom		
↳ $\cos\theta \in [-1, 0]$	$0.56 \pm 6.39 \times 10^{-2}$	0.12
↳ $\cos\theta \in [-1, -0.5]$	$0.39 \pm 5.41 \times 10^{-2}$	4.06×10^{-2}
Geometric		
↳ $\cos\theta \in [-1, 0]$	1.77 ± 0.12	1.23
↳ $\cos\theta \in [-1, -0.5]$	$0.77 \pm 7.59 \times 10^{-2}$	0.41
Quality		
↳ $\cos\theta \in [-1, 0]$	$0.26 \pm 4.36 \times 10^{-2}$	0.19
↳ $\cos\theta \in [-1, -0.5]$	$0.16 \pm 3.46 \times 10^{-2}$	5.11×10^{-2}

Table 7.12: Overview of the neutrino candidate and muon Monte Carlo rates based on v5.8.

Within the steep upgoing regime ($\cos\theta < -0.5$) this rate is strongly suppressed compared to the total muon rate in the upgoing regime and only increased by $\Delta\nu = 0.6 \times 10^{-2}$.
As the different selection strategies are based on the aim of finding neutrino candidates, a neutrino event should easily pass those selections. Thus, it is now checked, whether the individual events occur in the selections. The events occurring at least in two of the custom selections are listed in Table 7.13.
The overlap to the preceding analysis is only given by three events, which are also contained in the quality and the custom selection. Also no events are present in the geometric and the quality selection only. The events which emerge in all three newly developed selections are shown in Figure 7.22. The candidate event in run 4282 is most likely being caused by a sparking PMT. The indication is given by the multiple hits after the first triggered hit.
The candidate event contained in run 4360 fits very good to the reconstructed hypothesis, but it starts at the bottom of the detector. This also can be caused by a high energetic muon passing horizontally below the detector.

Run	**Event Id**	**Custom**	**Geometric**	**Likelihood**	**Preceding**
2430	17032	×	×		
2574	9662	×	×		
2613	22751	×	×		
2658	5579	×	×		
2689	20298	×		×	
2690	15083	×		×	
2849	5990	×		×	
2926	54	×	×	×	
2957	3866	×	×		
2976	4307	×	×		
3169	5587	×	×		
3177	13251	×		×	
4157	15880	×		×	
4222	20255	×	×	×	
4226	12888	×	×		
4242	8183	×		×	
4263	4399	×		×	
4282	15425	×	×	×	
4331	3857	×	×		
4360	8328	×	×	×	
4424	16918	×	×		
4460	19226	×	×		
4491	20890	×	×		
4614	24195	×	×		
4619	31335	×		×	
4634	14858	×	×		
4659	11895	×	×		
4677	37634	×		×	
4693	16014	×	×		
4693	39840	×	×		

Table 7.13: Measured events passing at least two of the selection types. Also the occurrence in the preceding analysis using v5.8 in [33] is shown.

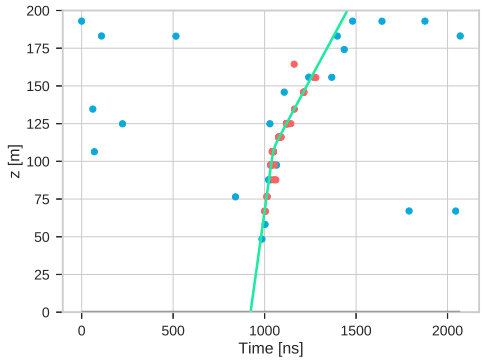

(a) Run-ID: 2926, Event-ID: 54

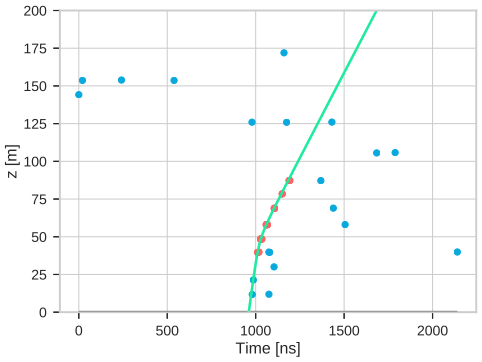

(b) Run-ID: 4222 Event-ID: 20255

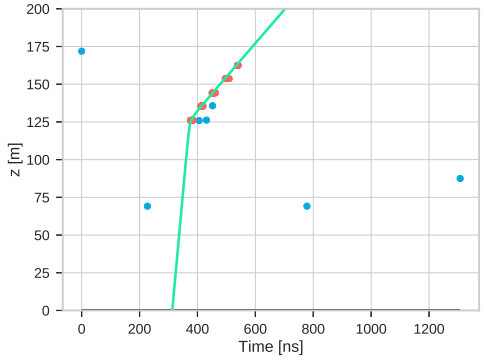

(c) Run-ID: 4282 Event-ID: 15425

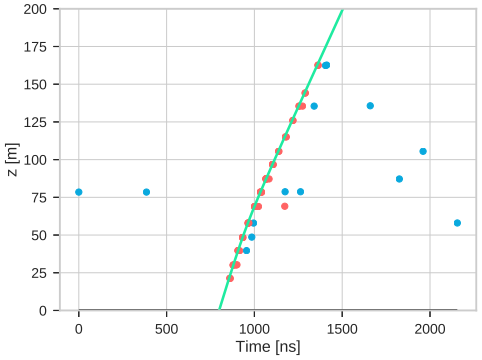

(d) Run-ID: 4360 Event-ID: 8328

Figure 7.22: Event displays for the events which occured in all newly developed selections within this thesis. It contains triggered (red) and snapshot hits (blue) and the arrival time hypothesis of the Čherenkov light cone based on the best JGandalf reconstruction (green).

8 Two Detection Unit Setup

In the period of the thesis reconstructed data from measurement and Monte Carlo simulations for a configuration consisting of two DUs was also available. Within the period of this study no comparable set of neutrino Monte Carlo simulations were available (see Section A.4). Thus, it is attempted to develop a reasonable neutrino candidate selection based on the available measurement data and muon Monte Carlo simulations.
The zenith distribution of the best JGandalf event reconstruction with respect to the maximum likelihood for this detector configuration is shown in Figure 8.1. The agreement of data and

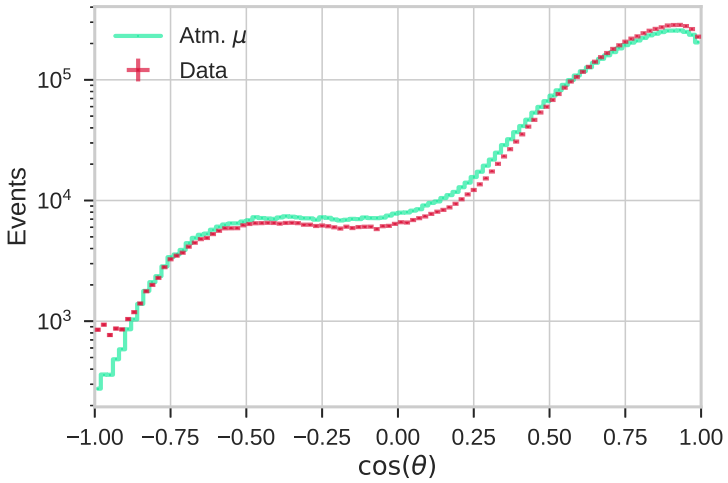

Figure 8.1: Zenith distribution for two DUs given as of the cosine of the best JGandalf reconstruction with respect to the likelihood value of measurement (red) and Monte Carlo data (green).

muon Monte Carlo is also given for this configuration and the reconstructed events in the upgoing regime for atmospheric muons are still present.
The most obvious starting point for applying a certain analysis to the data from the two detection unit configuration is the application of the muon rejection cuts applied to the one line data.

8.1 Preceding Analysis

In Figure 8.2 the resulting zenith distributions of the preceding selection cuts [33] are given. The individual event and run ids are given in Table 8.2. The distribution indicates good atmospheric muon rejection in the upgoing regime, because no muon event in this regime passed the selection cuts. This leads to feature distributions, which do not contain any muon events and thus no information about the necessity and validity of the selection cut limit. It is also a disadvantage in terms of the available livetime in the used selection of about 16 d, which does not provide much statistics at all.
When checking the event displays of the measured events in this event selection by eye they

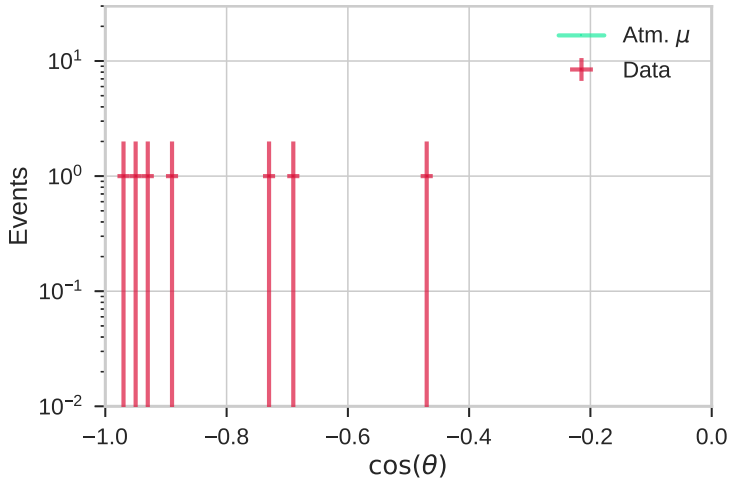

Figure 8.2: Final zenith distribution in the upgoing regime of the applied preceding selection (see Section 7.2) given as the cosine of the best JGandalf reconstruction with respect to the likelihood value for measurement (red) and Monte Carlo data (green). The Poissonian errors are given for the measured data.

show indicators for being background events. They are shown in Figure 8.3, whereas those are highlighted for different reasons.
The event given in Figure 8.3a contains two hits at $z < 50\,\mathrm{m}$ on DU3, which could also be an edge of a conic section of an event at a different zenith.
In Figure 8.3b one event is shown which has many hits on the same height level on DU4, whereas all other contained hits occur after the first hit on this level. This behaviour can also be caused by a sparking PMT.
The last event (see Figure 8.3c) was highlighted due to the low number of hits used for the reconstruction. In this specific case, the hits are distributed over a height of about $\Delta z \approx 125\,\mathrm{m}$.

Loosened Limits

In order to optimise these selection cuts in terms of the event numbers for the two-DU configuration the limits are loosened again. In particular the minimum of the mean vertical position of the triggered hits is set to 30 m, the minimal radial distance to one of the DUs is increased to 30 m and $\mathcal{L}_{\mathrm{Up}} - \mathcal{L}_{\mathrm{Down}}$ is required to be greater than 10.
The resulting distributions of the loosened features in the standard preceding analysis are shown in Figure 8.4.
The resulting zenith distribution for these modifications of the preceding selection cuts are shown in Figure 8.5. For the loosened limits 34 measured events in the whole upgoing regime are passing the cuts, whereas 9.1 muon events are expected within this regime. In the steeper regime of $\cos\theta < -0.5$, 23 measured events are passing the cuts and 6.4 muon events are expected from simulations.
The associated identities, i.e. the run and the event id, are also listed in Table 8.2.

8.2 Custom Selection

It is also attempted to set up a custom selection for the two-DU configuration, which is based on the selection cuts of the loosened limits of the preceding analysis. Again, the preselection outlined in Section 7.2 was used to reach a minimum event quality before determining the limits for this custom selection. The used features are applied again from the selections using

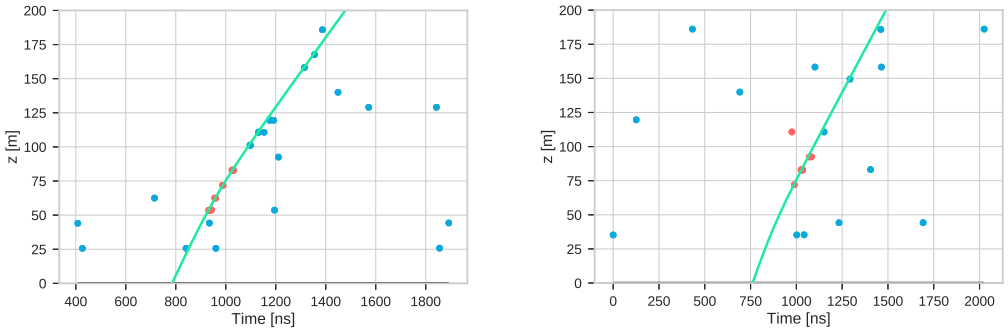

(a) Run-ID: 4836, Event-ID: 16354

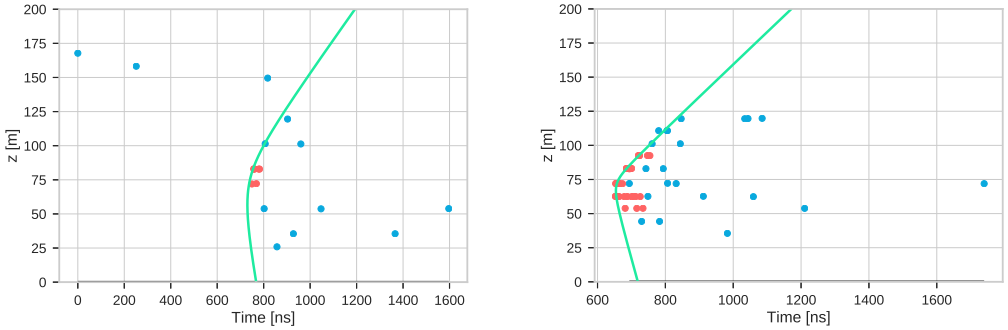

(b) Run-ID: 4890, Event-ID: 14476

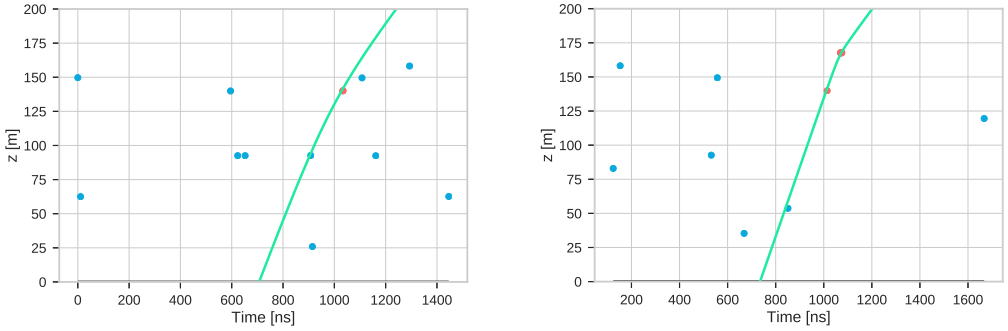

(c) Run-ID: 5018, Event-ID: 8787

Figure 8.3: Event displays for noticeable events using two detection units (DUs) and the selection cuts developed by Dmitry Zaborov. Each subfigure contains two event displays for DU3 (left) and DU4 (right). Every event display contains triggered (red) and snapshot hits (blue) and the arrival time hypothesis of the Čherenkov light cone based on the best JGandalf reconstruction (green).

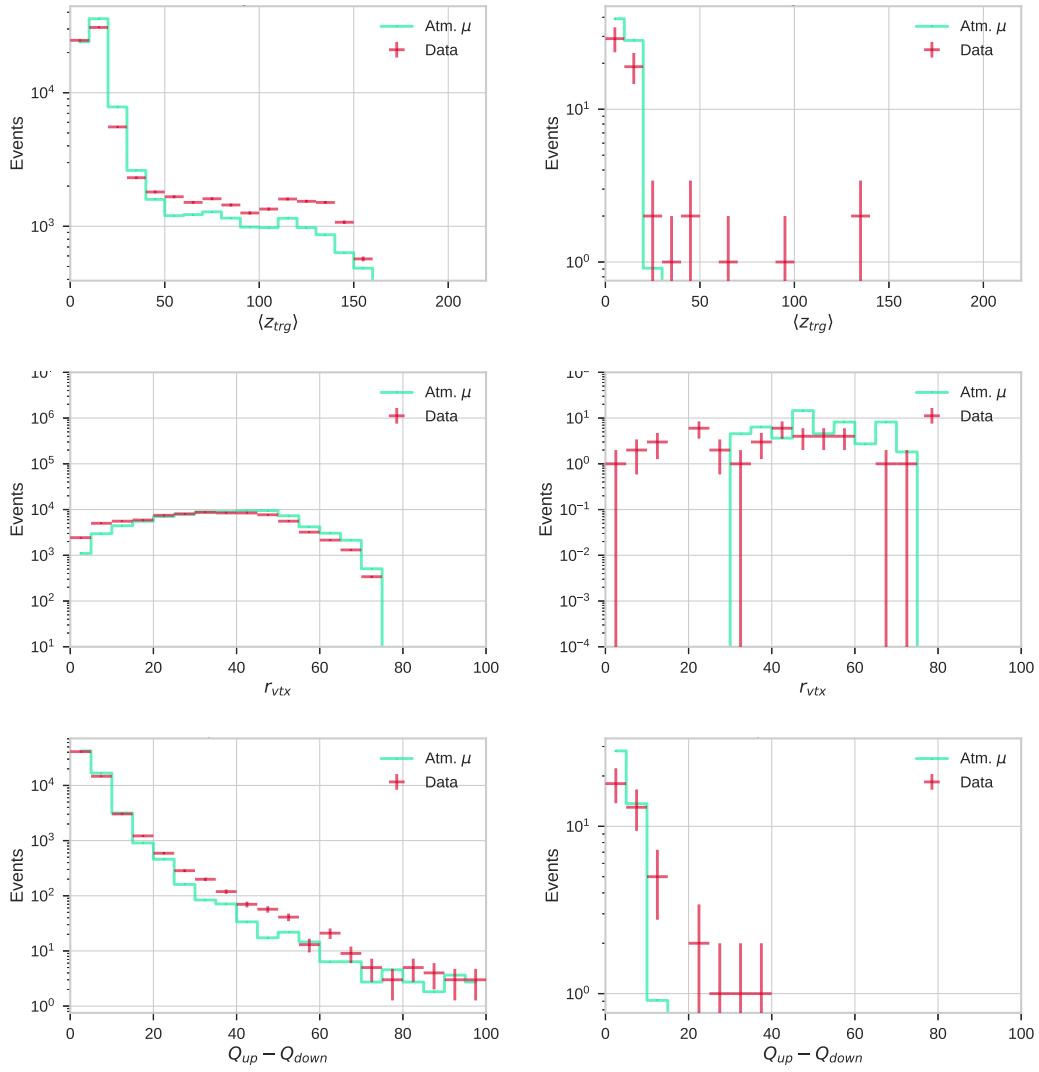

Figure 8.4: Distribution of the loosened features of the preceding selection, i.e. $\langle z_{\mathrm{trg}} \rangle$, r_{vtx} and $\mathcal{L}_{\mathrm{Up}} - \mathcal{L}_{\mathrm{Down}}$, for all upgoing events (left) and after the event selection (right).

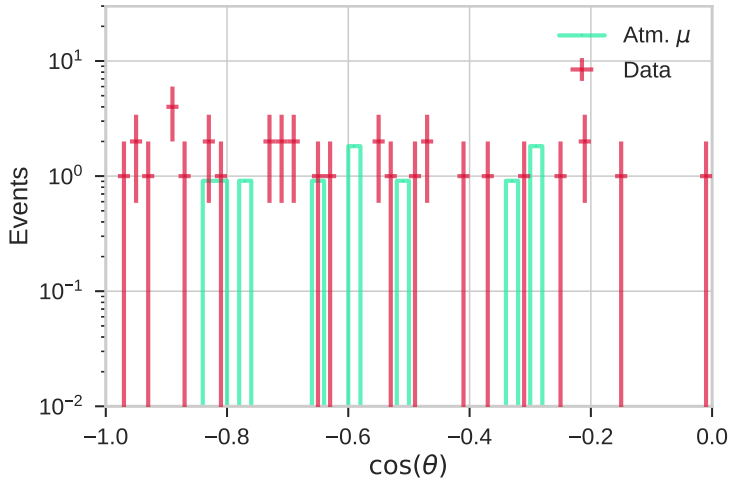

Figure 8.5: Final zenith distribution in the upgoing regime of the applied preceding selection (see Section 7.2) using loosened limits given as the cosine of the best JGandalf reconstruction with respect to the likelihood value for measurement (red) and Monte Carlo data (green). The Poissonian errors are given for the measured data.

a one-DU configuration (see Chapter 7) and the chosen limits for the selection cuts are listed in Table 8.1. In general the loosened features have been applied, whereas the other features of

Selection Cut	**Limit**	**Description**
$\langle z_{\text{triggered}} \rangle$	$> 30\,\text{m}$	Mean z coordinate of all triggered hits
r_{vertex}	$< 30\,\text{m}$	Radial distance of the reconstructed vertex position.
$R_{\text{On-time}}$	> 0.65	Ratio between on-time hits and hits within a range of $\pm 100\,\text{ns}$ around the best JGandalf hypothesis (see Equation (7.3))
$\max(\mathcal{L})/n_{\text{DoF}}$	> 2.3	Likelihood divided by the number of degrees of freedom
$\max(\mathcal{L}_{\text{up}})$	> 40	Best likelihood value for a JGandalf upgoing solution
$\max(\mathcal{L}_{\text{up}}) - \max(\mathcal{L}_{\text{down}})$	> 10	Difference between the best JPrefit up-going and down-going solution with respect to the likelihood value

Table 8.1: Custom selection features for two DUs without the use of any multi DU specific selection features.

the preceding analysis have been removed from the selection. As new features the on-time hit ratio $R_{\text{On-time}}$ and the likelihood over the number of degrees of freedom $\mathcal{L}/n_{\text{DoF}}$ are used.
The resulting zenith distribution is shown in Figure 8.6 and the individual events, i.e. the associated event and run id, are listed in Table 8.2.
Within this selection 20 measured events pass the cuts in the upgoing regime, where 14 of those have a zenith of $\cos\theta < -0.5$. This compares to 5 misreconstructed muon events, which equals a number of 4.6 due to the livetime normalisation. Four of these muon events are in the horizontal regime specifically at $\cos\theta > -0.2$.
After checking by eye the event displays, three events have been removed by hand from this selection. They are also marked in Table 8.2. Thus, finally this selection provides a measured candidate event rate of $\nu = 1.01 \pm 0.24\,\text{s}^{-1}$ at a muon rate from the simulation of $\nu_{MC} = 0.28 \pm 0.13\,\text{s}^{-1}$. The errors for both values are statistical errors assuming a Poissonian distribution for these integer distributions with a comparable low number of events. The distributions of the geometric features are shown in Figure 8.7. The mean vertical position of the triggered hits for the misreconstructed muon events still show an accumulation at $\langle z_{\text{trg}} \rangle < 30\,\text{m}$, which is also represented in the data by an excess in this regime.

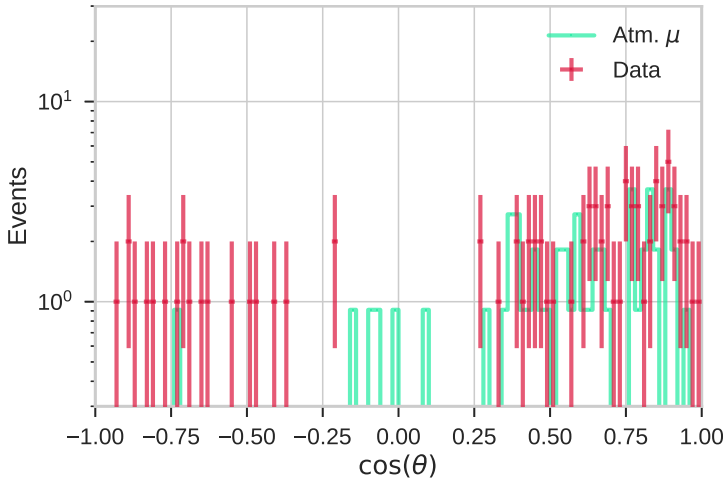

Figure 8.6: Final zenith distribution of the custom selection given as the cosine of the best JGandalf reconstruction with respect to the likelihood value for measurement (red) and Monte-Carlo data (green). The Poissonian errors are given for the measured data.

The radial distance for the two-DU configuration provides the smallest radial distance of the reconstructed vertex to one of the two DUs. The distribution for the upgoing events shows a displacement of both shapes with the measurement data being shifted to smaller distances. This is expected within distances of $r_{\text{vtx}} < 30\,\text{m}$ as it is expected to yield an increase of the neutrino contribution in this regime. This expectation holds for the distribution after the applied selection cut although this distribution contains little statistics. As the cluster of muon events in this final distribution above $r_{\text{vtx}} > 35\,\text{m}$, this feature cut is kept at $r_{\text{vtx}} < 30\,\text{m}$.
The on-time hit ratio cut was also kept, but the limit was loosened to $R_{\text{On-time}} > 0.65$. As in the final selection distribution no major contribution of muons was discoverable. At this cut limit one muon event is rejected and a lower bound on the hit selection was set. The distributions of the quality features are shown in Figure 8.7. The distribution for the difference of the best up- and downgoing likelihood shows the most statistics for the muon Monte Carlo. The agreement of measurement and muon Monte Carlo data is satisfied in the regime of $|\mathcal{L}_{\text{Up}} - \mathcal{L}_{\text{Down}}| < 10$. For larger values more events in the measured data pass the remaining selection cuts, which is expected for the neutrino events, when compared to the results of the single DU selections (see Chapter 7). Thus, this selection feature was used and the limit was set to $\mathcal{L}_{\text{Up}} - \mathcal{L}_{\text{Down}} > 10$.
Within the upgoing event distribution of $\mathcal{L}/n_{\text{DoG}}$ the shift of the peak in the measurement towards higher values is also present for this detector configuration. The lower limit is chosen with $\mathcal{L}/n_{\text{DoG}} > 2.3$ as this is at the data peak and it is the lower limit of the main cluster of data events after the selection.
The limit of the best upgoing JGandalf likelihood was set to $\mathcal{L}_{\text{Up}} > 40$ as this rejects too strong increases of the data events at lower values of this feature. This increase is expected to result from atmospheric muons comparing it to the position of the simulated muon events and to the distribution of the one-DU configuration (see Figure 7.15).

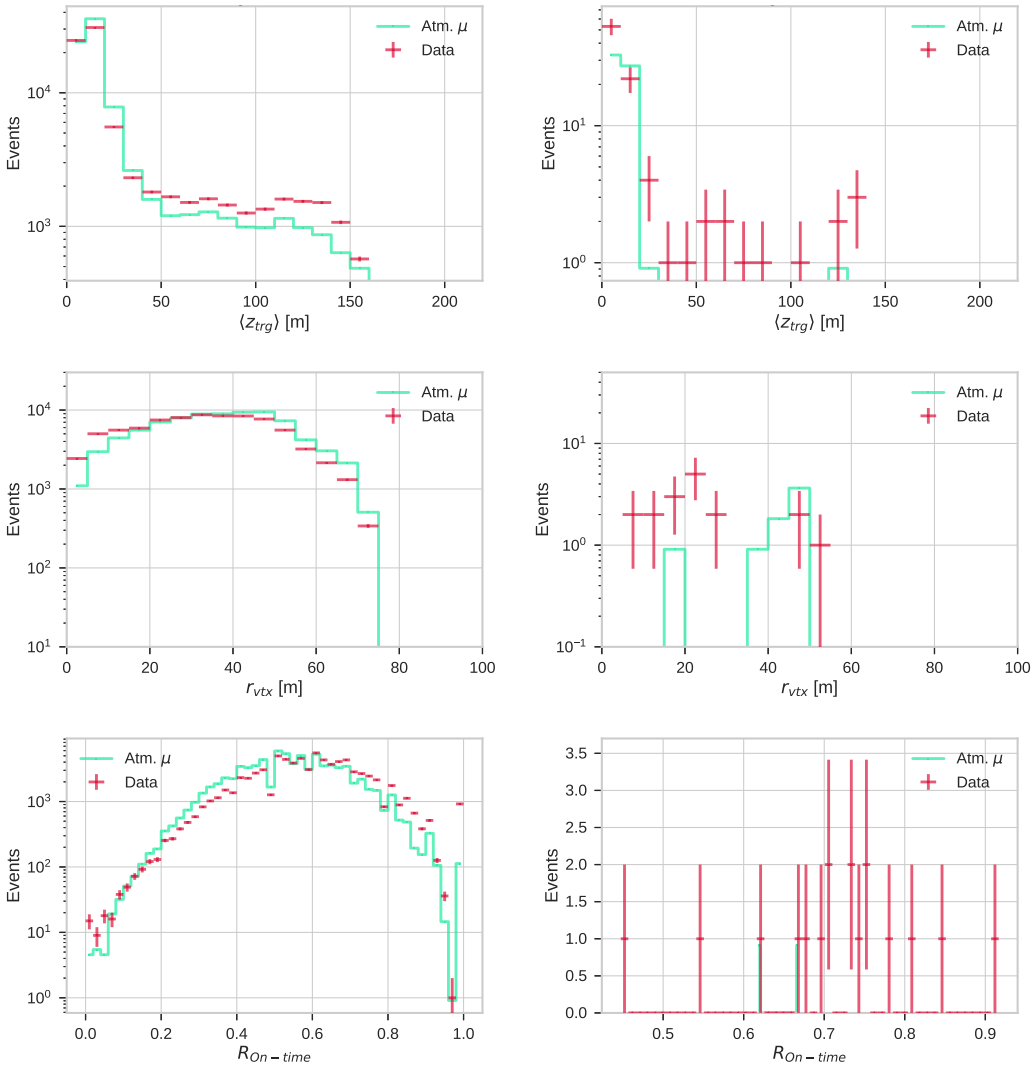

Figure 8.7: Distributions of the different geometric features used in the custom two-DU selection for all upgoing events before (left) and after the event selection (right). The plots consist of measured data (red) and Monte Carlo simulations of atmospheric muons (green).

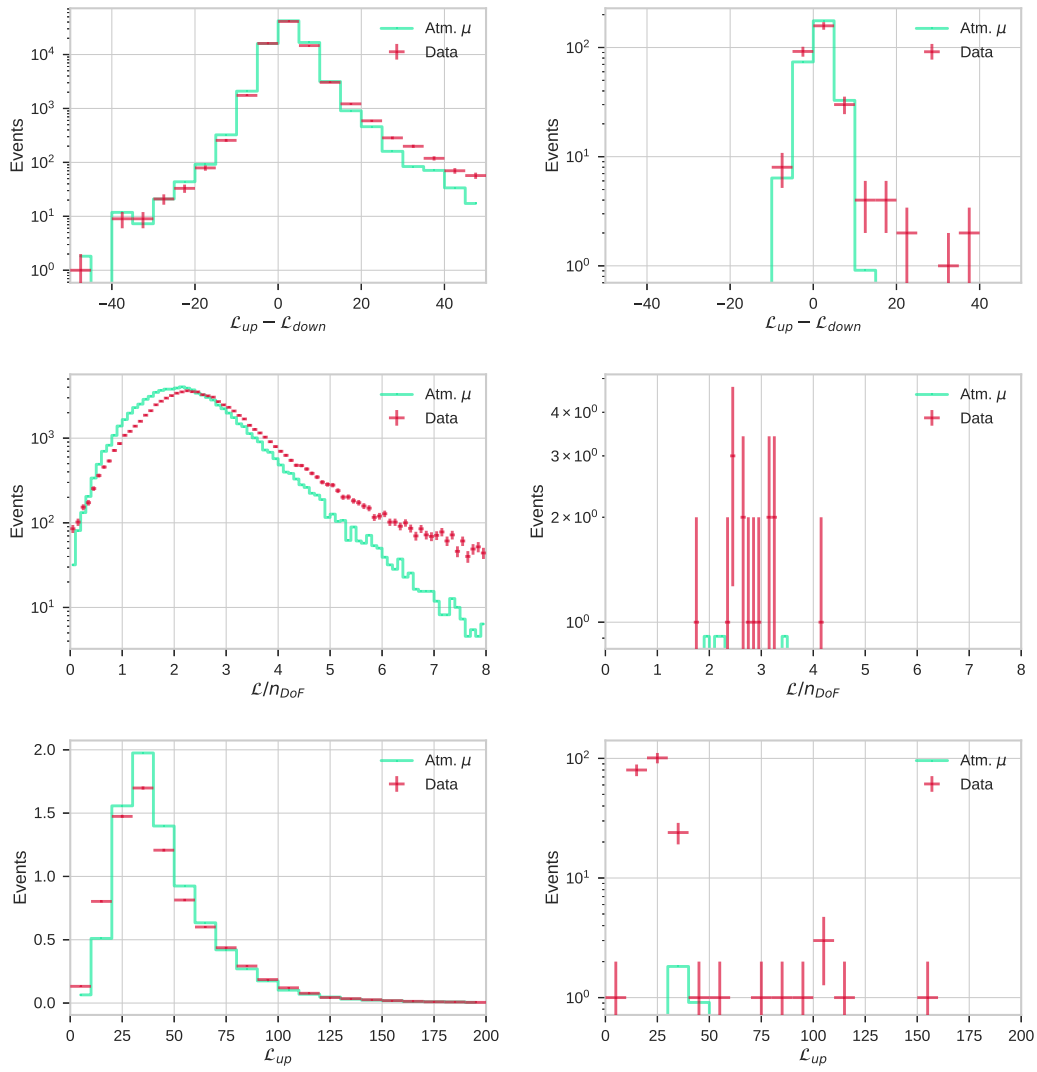

Figure 8.8: Distributions of the different quality features used in the custom two-DU selection for all upgoing events before (left) and after the event selection (right). The plots consist of measured data (red) and Monte Carlo simulations of atmospheric muons (green).

Run	Event Id	$\cos\theta$	Custom	Preceding	Preceding (Eased Limits)
4786	14547	0.54			×
4804	30445	0.49	×		×
4806	23126	0.89	×		×
4836	16354	0.97		×	×
4838	16072	0.14			×
4840	9602	0.21	×		×
4867	18452	0.46	×		×
4876	6581	0.68		×	×
4883	21247	0.90			×
4885	27610	0.90	×	×	×
4890	14476	0.46		×	×
4892	22072	0.76	×		
4893	6095	0.95		×	×
4895	5318	0.83			×
4897	12218	0.70	×		×
4903	6450	0.20	×		×
4904	15753	0.90			×
4925	14790	0.54	×		×
4926	17558	0.84			×
4948	6651	0.89	×		
4959	25505	0.83	×		
4975	13767	0.01			×
4982	10744	0.70	×		×
4983	8141	0.68	×		×
4985	19865	0.26			×
4994	13719	0.95			×
4996	24155	0.41	×		×
5007	15932	0.80	×		
5011	27984	0.73			×
5018	8787	0.93	×	×	×
5021	28046	0.38	×		×
5022	27459	0.65	×		×
5029	19635	0.80			×
5031	515	0.73	×	×	×
5037	13803	0.62	×		×
5060	12730	0.31			×

Table 8.2: Measured event ids for the preceding [33] selection cuts, the preceding selection cuts with loosened limits and the custom selection cuts using the two DU dataset. One notable event (see Figure 8.3) which also occurs in the custom selection is marked in yellow.

Part III

Application of IFT methods to neutrino data

In the following part a first attempt was done to use IFT based methods on neutrino data. Specifically, the resulting night sky images from applying different assumptions on the correlation structure was analysed. The study was done within the ANTARES experiment.

9 ANTARES Neutrino Sky

The idea of using information field theory (IFT) for investigating the neutrino sky based on ANTARES data is inspired by the Ph.D. Thesis of Stefan Geißelsöder which is titled "Model-independent search for neutrino sources with the ANTARES neutrino telescope" [35]. In this model-independent search the data was studied for significant structures without considering a certain prior model.
The following study is not model independent as some prior is postulated, which consists of a certain correlation structure, even though no previous knowledge on night-sky structures or sources are included in the analysis.

9.1 Data & Correlation Structure

In order to use the NIFTy framework (see Section 6.6) the input data needs to describe a discrete field distribution. The measurement data is given as a set of events, which consist of the reconstructed directional infomation $\hat{n}$ and energy E each. Thus, the data is converted to a multi-dimensional histogram to provide the information pixelised as a discrete field. The directional information $\hat{n}$ is encoded to one dimension using HealPix [36] and the energy value is binned on logarithmic scale.
HealPix was used in ring mode set to $N_{\text{side}} = 32$, which equals 12288 directional pixels. The energy was discretised into 20 pixels within a range of 1 GeV to 1 PeV, which yields 245, 760 pixels over both dimensions in total. This yields a memory size of about 1 Mb per sample during the minimisation process. The studied fluxes are very faint, which leads to a low number of events. To avoid a larger amount of empty bins compared to the total number of pixels, a more coarse discretisation has been choosen.
The mapping from a certain direction and energy to the histogram value at a certain position is denoted as

$$d : \hat{n} \otimes E \mapsto \mathbb{N}^+ . \tag{9.1}$$

The target domain being positive integer numbers is required by the Poissonian likelihood (see Chapter 4). In order to reconstruct a signal field using NIFTy, its structure has to be defined. For every used Gaussian field the hyperpriors need to be provided, which makes the parametrisation complex for a larger amount of those fields. It was decided to use two Gaussian fields f_{bg}, the background field, and f_{ps}, the point-source field, which are modelled by an amplitude operator each. The composition of the signal field $s : \hat{n} \otimes E \mapsto \mathbb{R}$ is then given by

$$s = R^{(\hat{n})} \circ \left[R^{(E)}_{\text{ps}} \circ \exp\left(f_{\text{ps}}\right) + R^{(E)}_{\text{bg}} \circ \exp\left(f_{\text{bg}}\right) \right] . \tag{9.2}$$

where f_{bg} and f_{ps} are Gaussian fields. The signal is composed of the exponentials of those fields, which provides the signal value being the mean of the Poissonian distribution to be positive definite. The exponential is also a bijective map on $\mathbb{R} \to \mathbb{R}^+$. Due to the exponential energy spectrum and the wide value range, these exponentials provide a more linear regime for the reconstructions of the Gaussian fields.
The operator $R^{(\hat{n})}$ applies the signal response to the directional domain, which is based on the general visibility of upgoing events at the ANTARES site averaged over time (see Figure 9.1a).

The operators $R_{\text{ps}}^{(E)}$ and $R_{\text{bg}}^{(E)}$ are the signal responses on the energy domain, which follow

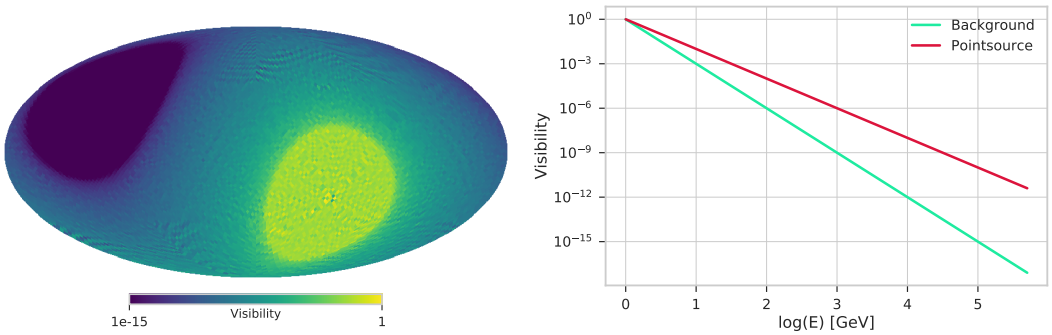

(a) Signal response $R^{(\hat{n})}$.

(b) Signal response $R_{\text{ps}}^{(E)}$ and $R_{\text{bg}}^{(E)}$.

Figure 9.1: The overall visibility of the ANTARES detector for upgoing events in galactic coordinates averaged over time. This visibility was used as spatial response in the $\hat{n}$ domain R_{sky}. The blindspot was set to an arbitrary low value greater than zero, because the expectation value of the used Poissionian distribution is undefined at zero.

the expected power law distribution (see Equation (3.1)). The response distribution for these operators is shown in Figure 9.1b. All response distributions are equipped with a minimum value of 10^{-15}. This minimum is required by the used Poisson distribution, which is undefined at 0 and would lead numerically to a NAN value for the evaluated Hamiltonian.
In order to display the contribution of both fields to the reconstructed signal, the two partial signals

$$s_{\text{ps}} = R^{(\hat{n})} \circ R_{\text{ps}}^{(E)} \circ \exp\left(f_{\text{ps}}\right) \tag{9.3}$$

and

$$s_{\text{bg}} = R^{(\hat{n})} \circ R_{\text{bg}}^{(E)} \circ \exp\left(f_{\text{bg}}\right) \tag{9.4}$$

are introduced.
The starting values and the parameter range for the hyperpriors of the signal fields f_{PS} and f_{BG} are listed in Table 9.1.

Parameter	**Name**	$f_{\text{PS}}^{(\hat{n})}$	$f_{\text{PS}}^{(E)}$	$f_{\text{BG}}^{(\hat{n})}$	$f_{\text{BG}}^{(E)}$	**Description**
spectral bins	`n_pix`	128	128	128	128	Number of spectral pixels
gaussian variance	`a`	2.0	2.0	2.0	2.0	Constant broadening factor
frequency cut-off	`k0`	0.3	0.2	0.3	0.2	Frequency miniminum
slope	`sm`	-1.5	-1.5	-2.5	-1.5	Correlation structure
↳ variance	`sv`	0.8	1.0	0.8	1.0	
y-intercept	`im`	1.0	1.5	2.0	1.0	Field value contrast
↳ variance	`iv`	0.4	0.6	0.8	0.5	

Table 9.1: Hyper priors of the used power-law operators, which define the constraint correlation structure of the reconstructed fields.

9.2 Flux Normalisation & Test Statistics

As it was outlined in Chapter 3, i.e. in Equation (3.1), the different fluxes in the considered environment are expected to follow power laws at different spectral indices γ. The flux normalisation Φ_0 provides a quantity to specify the magnitude of those fluxes, which is defined

by

$$\tilde{\Phi} = \frac{\mathrm{d}\Phi}{\mathrm{d}E_\nu \mathrm{d}\Omega} = \Phi_0 \left(\frac{E_\nu}{E_{\mathrm{ref}}} \right)^{-\gamma} . \tag{9.5}$$

The parameter E_{ref} is set to 1 TeV for comparability reasons. Thus, the mean number of events based on this flux normalisation and the measurement time T is given by

$$\langle n \rangle = T \int_{E_{\mathrm{min}}}^{\infty} dE \, A_{\mathrm{eff}}(E) \, \tilde{\Phi} \, , \tag{9.6}$$

where A_{eff} is the effective target area of the detector and the used minimal energy is set to $E_{\mathrm{min}} = 1\,\mathrm{GeV}$.
In order to get a single quantity to classify the reconstruction quality with respect to the well known source position of the toy skymap a certain test statistic needs to be defined. Thus, the results of using different field distributions can be compared directly. As the reconstructed fields are continuous, no specific event distribution according to a specific flux model needs to be considered. When integrating over the energy dimension, an increase of the reconstructed field s_{ps} value at the point source location should appear.
In order to analyse this increase at a specific location, the point-source position of the toy skymap is compared to the neighbouring pixels. It was chosen to use 8 ring layers aroung the pixel, which equals 512 pixels and about 4 % of the total solid angle. For those pixels the mean and standard deviation of the s_{ps} value is calculated and a significance value for each point-source position is determined.

9.3 Toy Sky Map

In order to test the setup under well-defined conditions, the toy skymap was set up for testing and optimising the parameters towards using them on certain event selections from the measurement. The convergence of the NIFTy tools highly depends on the starting values, i.e. the hyper-prior parameters of the reconstrcuted fields. This toy sky map was composed of point-source and background like neutrino events. The details of these distributions are outlined in the following. In Figure 9.2 an exemplary test sky map in galactic coordinates is shown.
The detector livetime of the toy model sky map is set to 3125 d, which is equal to the livetime of the public event selection which is studied in Section 9.4.

Random Point-Source Sky

The mock point-source sky consists of a predefined number of sources, which are positioned on the sky map first. The positioning can be selected to be completely random or to form clusters. The clustering can be parametrised by an opening angle, which has to be provided to define the size of the structures. The spectral index of the point source flux is set to $\gamma_{\mathrm{PS}} = 2$ and the energy of the received events was chosen according to this spectrum. For a given spectral index and flux normalisation the mean number of received events is given by Equation (9.6), which is used to choose the individual number of received events for each source following the Poisson distribution. The direction of the events is chosen according to a certain angular pointspread around the source they originate from. The used pointspread was set to 0.4° as this is the value also given for the public dataset.
The blind spot of the detector, which is caused by the field of sensitivity being just 2π looking downwards through the earth, can directly be seen in the background field (see Figure 9.2). The positioning of the point-sources is applied directly to the galactic sky map without rejecting the blind spot region directly. For each source the number of received detector events is randomly chosen following a Poisson distribution, based on the mean number of events as it was derived in Equation (9.6). The fluxes used within this study are listed in Table 9.2.

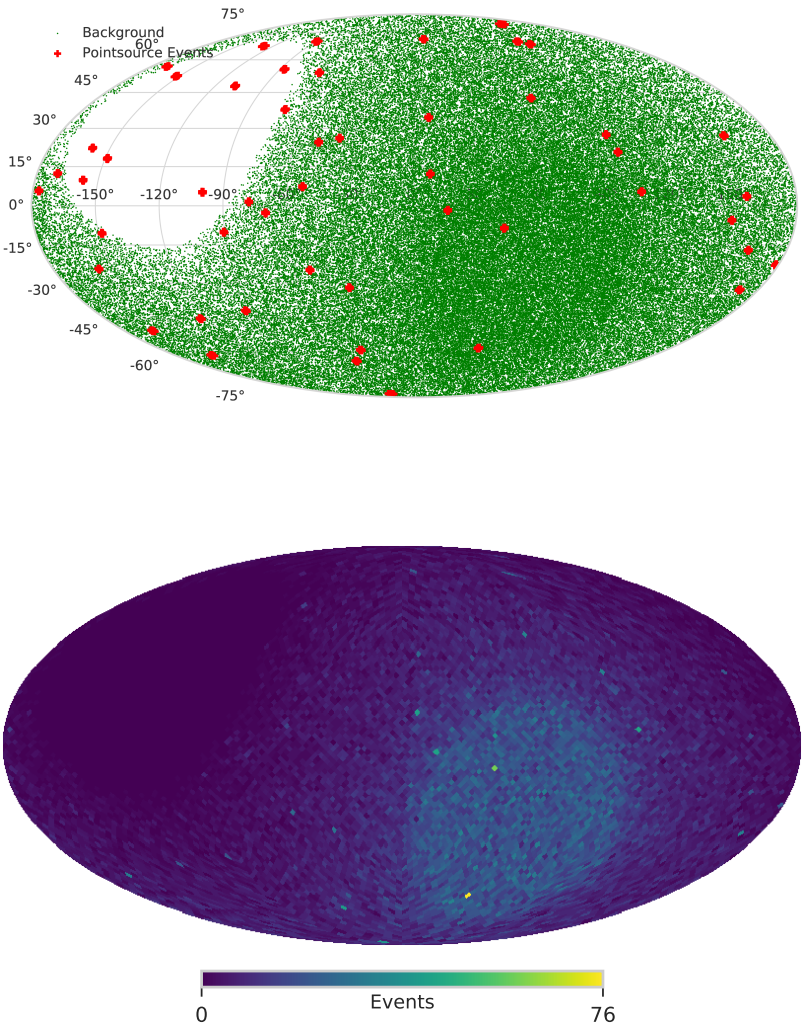

Figure 9.2: Mock sky map (top) in galactic coordinates with randomly placed point sources at $\Phi_0 = 4.77 \times 10^{-11}\,\mathrm{TeV}^{-1}\,\mathrm{cm}^{-2}\,\mathrm{s}^{-1}$ and their associated detector events (red). The green dots mark isotropic background events based on a time dependent event rate. Also the pixelised events in the directional domain integrated over energy is shown (bottom).

Flux Φ_0 $[\mathrm{TeV}^{-1}\,\mathrm{cm}^{-2}\,\mathrm{s}^{-1}]$	**Events** $\langle n \rangle$
4.77×10^{-12}	5
9.53×10^{-12}	10
1.91×10^{-11}	20
2.86×10^{-11}	30
3.81×10^{-11}	40
4.77×10^{-11}	50

Table 9.2: Used fluxes and the associated mean number of events measured within the live-time of 3125 d and a minimal Energy of $E_{\mathrm{min}} = 1\,\mathrm{GeV}$.

Diffuse Neutrino Background

The generation of events from the diffuse neutrino flux with respect to the direction is adapted from the implementation and event selection by Stefan Geißelsöder. The diffuse neutrino flux was supposed to be isotropic with a mean event rate of $\nu = 7.3\,\mathrm{d}^{-1}$ and a flux of

$$E^3 \times \Phi_{\mathrm{Atm}} = 6 \times 10^{-2} \mathrm{TeV}^2\,\mathrm{cm}^{-2}\,\mathrm{s}^{-1}\,, \tag{9.7}$$

which is consistent with the value specified in the plot given in Figure 3.6. In this model it is assumed that this neutrino background is caused by atmospheric neutrinos, thus the spectral index for the energy distribution was set to $\gamma_{\mathrm{BG}} = 3$. This rate is fluctuating over time due to multiple effects. Those can be split up into periodic and temporary effects. Such a temporary effect is for example an unscheduled downtime of the detector, which is not supposed to generate significant structures in the background distribution. Periodic effects, e.g. caused by thermal fluctuations of the atmospheric density or due to a reduced detection efficiency caused by bioluminescence, are included in the generation of the diffuse flux based on measured data and are shown in Figure 9.3.

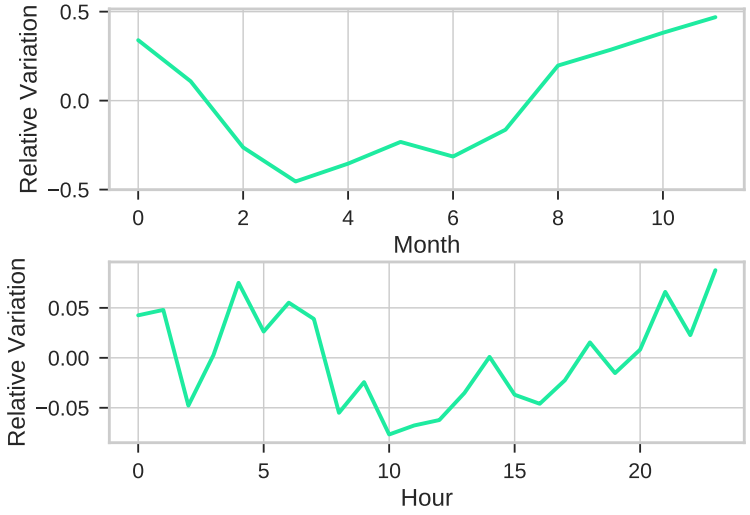

Figure 9.3: Relative rate variations for the simulated neutrino background per month (top) and per day hour (bottom).

Background Results

First, the reconstruction script is tested without any point-source contribution. This procedure is done with respect to occuring structures caused by missing features in the applied response. In general those missing features can be a physical effect which is not considered within the response. The responses are modelled for each domain individual and correlated effects are also not considered. In the toy model only the visibility was encoded to the response in the directional domain, thus the time dependent background rate variation is an example for such an effect.
The initial data and the resulting distributions for the background reconstruction is shown in Figure 9.4.
The energy distribution shows that the used energy range is too wide compared to the flux shape and the rate of background events. As the field is reconstructed with cyclic boundaries, the energy range is kept. Thus, possible effects based on this technical constraint are shifted to higher energies. In this higher regime those effects are weakened, because those field values are

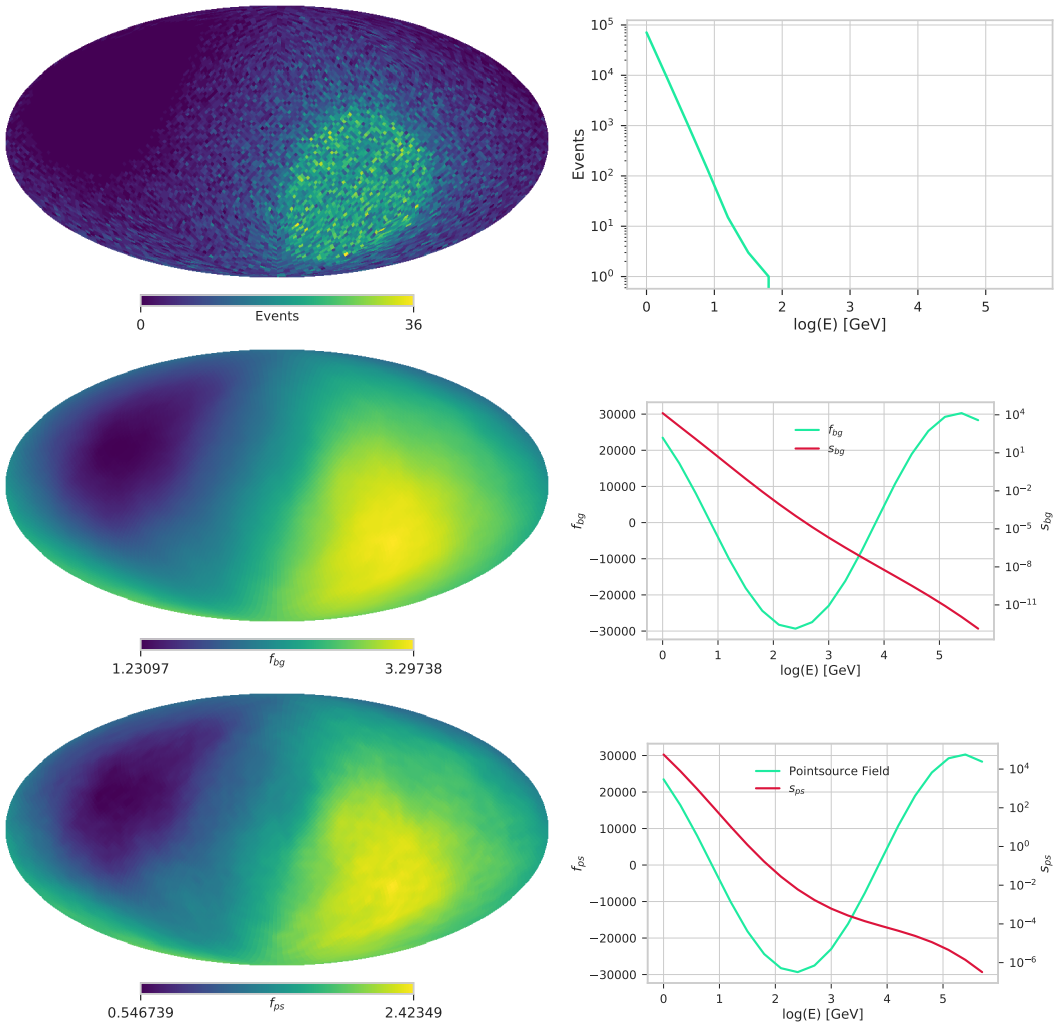

Figure 9.4: Distributions resulting from the background test with the pixelised input data (upper), the reconstruced background field (middle) and the reconstruced point-source field (lower). Every distribution is integrated over energy domain (left) and over directional domain (right).

multiplied to a power law based energy response, which is multiple orders of magnitudes lower for higher energies.
The energy distribution for the background field is expected to be flat for a certain constant, because this would lead to the power law spectrum, the data was generated with. The non flat distribution can be explained because of the combination with the pointsource field. The decrease for the pointsource spectrum is expected, because the initial distribution only contains background events and an additional one over energy term is required besides the pointsource energy response in order to fit to the data. The dipole structure is still present in the reconstructed field in both distributions of the directional domain, whereas the value range in the expected regime of about 10 % compared to the range of the initial pixelised data. This is in the same order of magnitude as rate variations (see Figure 9.3).

Pointsource Results

The resulting point-source signal field s_{ps} (see Equation (9.3)) distributions containing pointsources at the fluxes given in Table 9.2 are analysed as it was outlined in Section 9.2. Following this determination of this significance, the mean and the standard error of those values is determined. Those results are plotted over the flux, which is shown in Figure 9.5. Three resulting directional

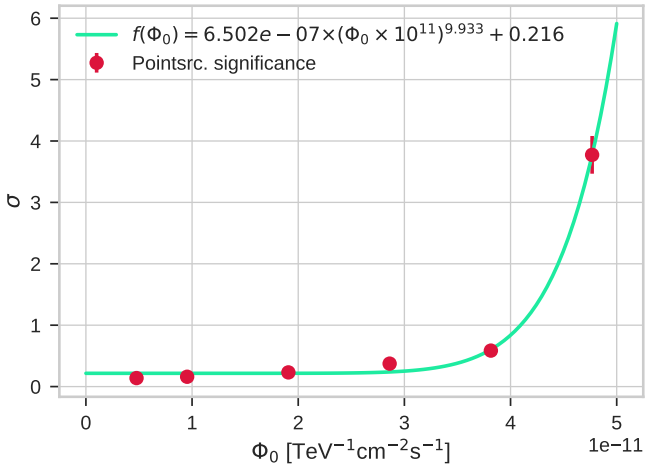

Figure 9.5: Significance of the pointsource field f_{PS} based on the Gaussian field distribution.

fields are shown in Figure 9.6, where the resulting fields of the directional domain for the minimal and maximal simulated fluxes are given. As the significance value already drops below the data point at $\Phi_0 = 4.77 \times 10^{-11}\,\mathrm{TeV}^{-1}\,\mathrm{cm}^{-2}\,\mathrm{s}^{-1}$ the result for $\Phi_0 = 3.81 \times 10^{-11}\,\mathrm{TeV}^{-1}\,\mathrm{cm}^{-2}\,\mathrm{s}^{-1}$ is also given.
The point-source placed in the blind spot are not removed from the determination of the significance in order to have a veto region to check the significance values at those positions, which are expected to be close to zero.
This exception can possibly be violated, because of the non-zero value this region is set with respect to the Poissionian likelihood. Thus, the reconstruction could contain structures at the blind spot based on large values of a misreconstructed field.
In the reconstructed point-source field, i.e. the signal s_{PS}, the blind spot values are at the minimum of the value range and the significances of the point-source are close to 0 as it is expected.

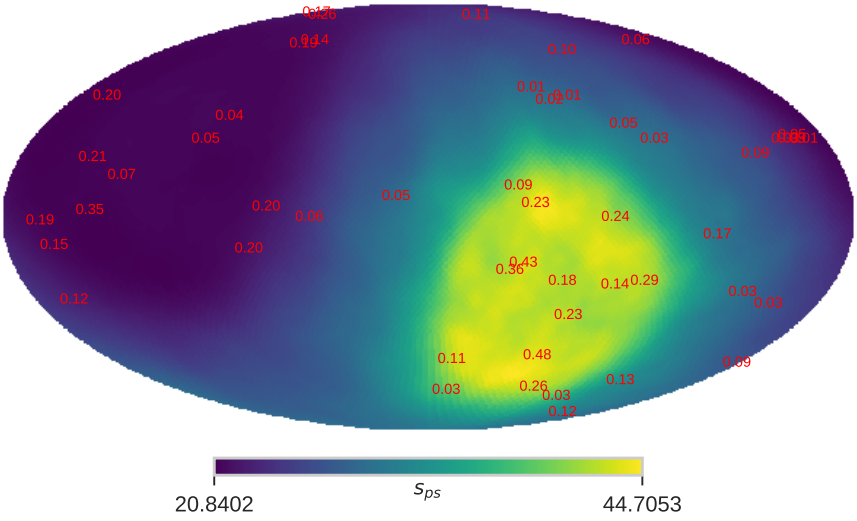

(a) $\Phi_0 = 4.77 \times 10^{-12}\,\mathrm{TeV}^{-1}\,\mathrm{cm}^{-2}\,\mathrm{s}^{-1}$

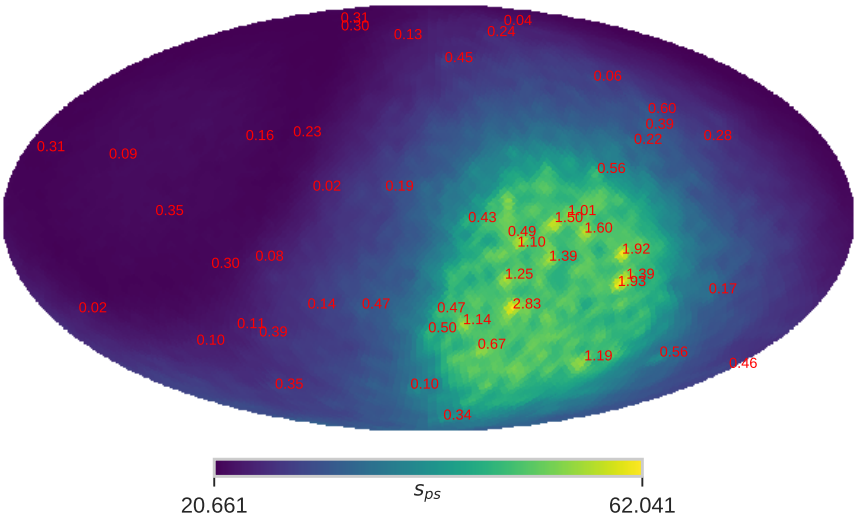

(b) $\Phi_0 = 3.81 \times 10^{-11}\,\mathrm{TeV}^{-1}\,\mathrm{cm}^{-2}\,\mathrm{s}^{-1}$

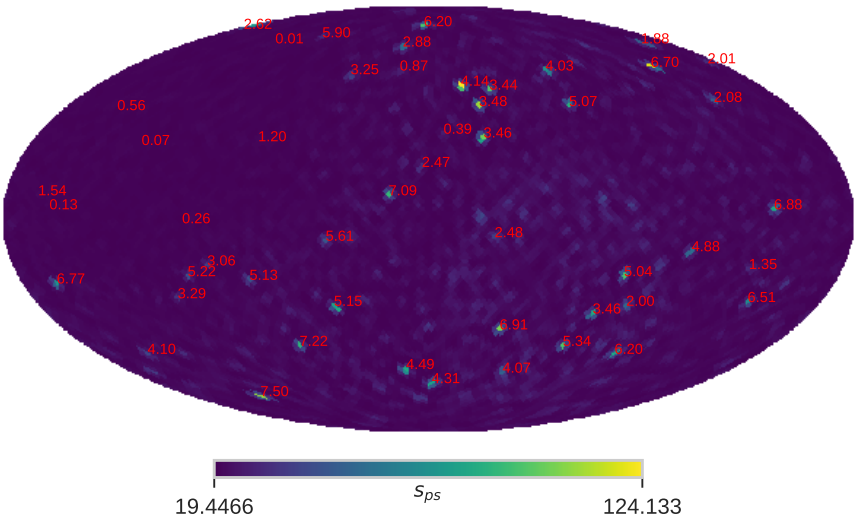

(c) $\Phi_0 = 4.77 \times 10^{-11}\,\mathrm{TeV}^{-1}\,\mathrm{cm}^{-2}\,\mathrm{s}^{-1}$

Figure 9.6: Reconstructed point-source signal field s_{ps} results at different fluxes. For each simulated point-source the significance with respect to the field values of the next pixels are determined. Each value is plotted next to the initial point-source position.

9.4 Event Selection & Detector Data Results

The application of the IFT to actual measurements of the ANTARES detector requires a event selection. In this study no individual selection was done, but the selection for doing point source research, which was recently published, was used. The data of this public selection can be retrieved at [37] and is based on the publications [38, 39]. The directional distribution of

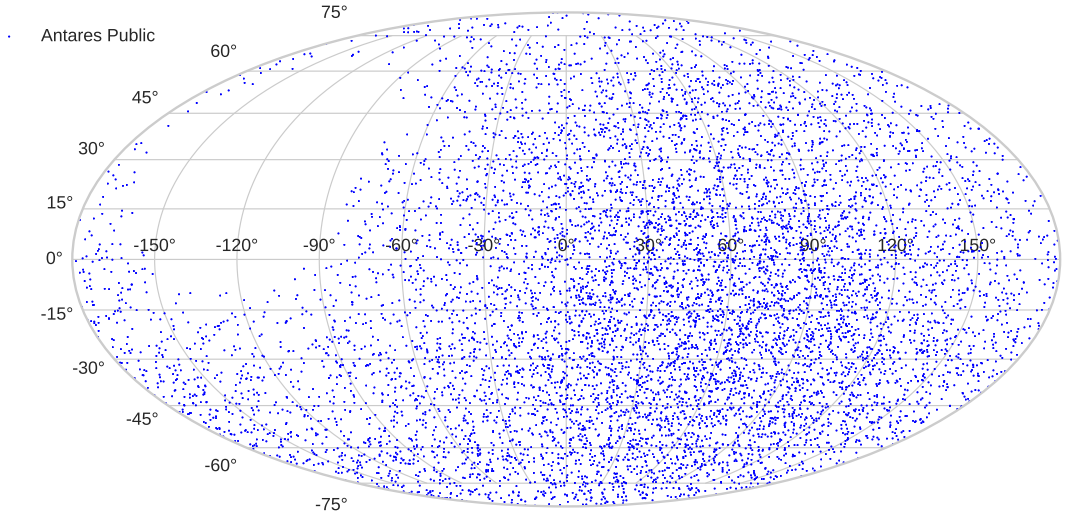

(a) Spacial distribution of the event directions in galactic coordinates.

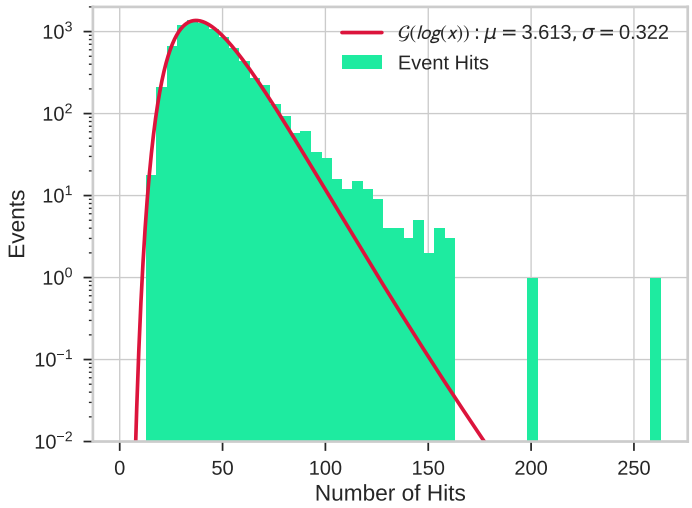

(b) Number of hits per event, with fitted Gaussian distribution on logarithmic x-axis being the approximate distribution.

Figure 9.7: Parameter distributions of the events from the public ANTARES dataset [37].

the event selection is shown in Figure 9.7a. The energy is given indirectly via the number of received hits, which distribution is also given in Figure 9.7b. Thus, the energy domain and response has to be modified with respect to the properties of the hit numbers. The number of pixels for this domain is kept constant with an amount of 20. This event selection is specifically conditioned for point-source research, hence the used signal model is modified. Now only one

inferred Gaussian field f is used and the signal is composed by

$$s = R^{(\hat{n})} \circ R^{(\mathrm{NHits})} \circ \exp(f), \tag{9.8}$$

where $R^{\hat{n}}$ is the spatial response applied from the toy model (see Figure 9.1a) and $R^{(\mathrm{NHits})}$ is the hit number response. The response is taken from the hit number distribution as it is shown in Figure 9.7b, which was normalised the maximum value being one.
The hyper-priors and in particular the slope of the power spectrum is varied to gain different structures for comparison. Those different configurations are shown in Table 9.3.

Parameter	**Name**	**1. Config**		**2. Config**		**3. Config**	
		$f^{(\hat{n})}$	$f^{(NHits)}$	$f^{(\hat{n})}$	$f^{(NHits)}$	$f^{(\hat{n})}$	$f^{(NHits)}$
spectral bins	`n_pix`	64	64	64	64	64	64
gaussian variance	`a`	3.0	3.0	3.0	3.0	3.0	3.0
frequency cut-off	`k0`	0.4	0.4	0.4	0.4	0.4	0.4
slope	`sm`	-0.5	-2.0	-1.5	-2.0	-3.5	-2.0
↳ variance	`sv`	0.5	1.0	0.5	1.0	0.5	1.0
y-intercept	`im`	0.5	1.0	0.5	1.0	0.5	1.0
↳ variance	`iv`	0.3	0.5	0.3	0.5	0.3	0.5

Table 9.3: Hyper priors of the used slope operators, which define the correlation structure on one of the consisted domains on the space.

In Figure 9.8 the reconstructed fields based on the public dataset are shown. For all hyper-prior configurations an elevation on close to the position of the equator is present along with the expected dipole structure, caused by the visibility. Those structures are attributed to the simplified detector response, which is mostly related to the declination dependent detector response. This problem could not be resolved by implementing the provided declination dependent effective area.

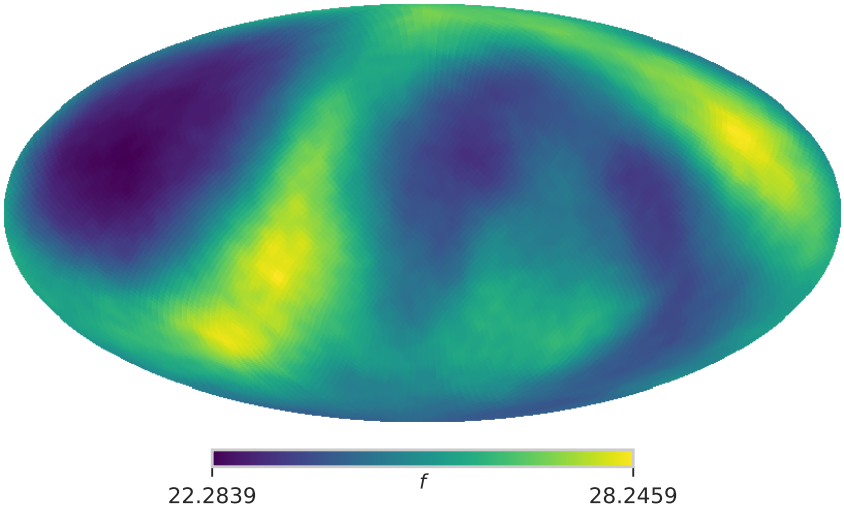

(a) `sm` $= -0.5$

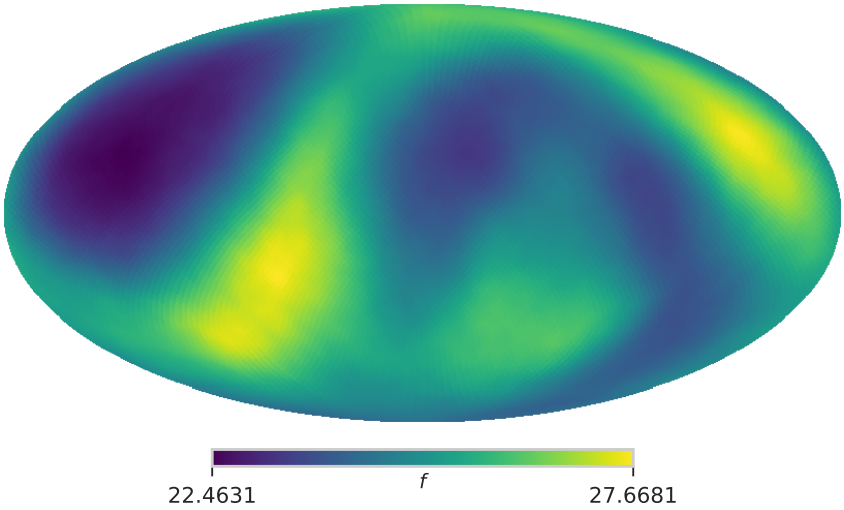

(b) `sm` $= -1.5$

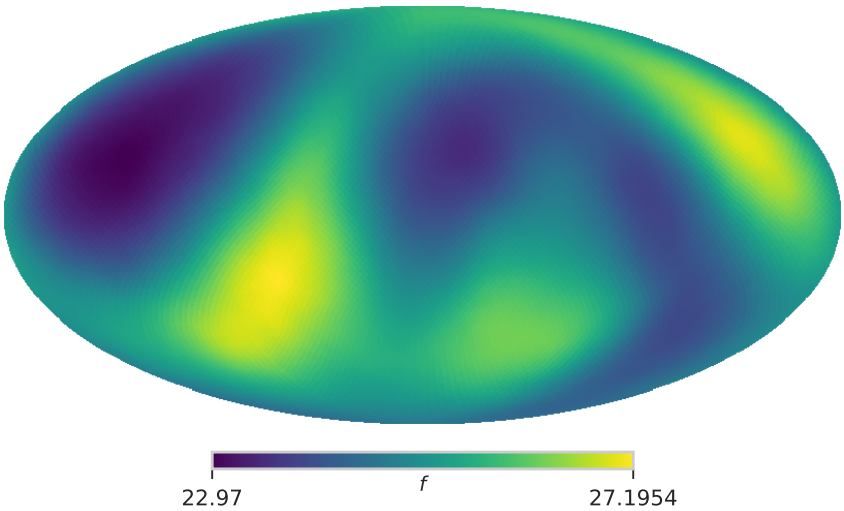

(c) `sm` $= -3.5$

Figure 9.8: Exponential of the reconstructed field $\exp(f)$ at different slope parameters `sm`. The response of the directional domain just containing the visibility at the ANTARES detector location for upgoing events (see Figure 9.1a).

10 Conclusion & Outlook

In this thesis As starting point the neutrino selection of [33] is reproduced independently. The own neutrino candidate selection using first KM3NeT/ORCA data yielded a measured event rate of $\nu = 0.39\,\mathrm{s}^{-1}$ in the regime of $\cos\theta < -0.5$, which has a statistical error of 10 % using a single detection unit at a livetime of 133 d. This doubles the rate of the preceding analysis [33] without a final evaluation of the neutrino candidate events by checking the event displays by eye.
For the custom two DU selection a rate of one measured candidate event per day has been found, which has an error of 25 %. This statistical error will decrease for a dataset based on a longer detector livetime, which for this dataset was 16.7 d. An evaluation of the detector efficiency and the related systematic error was not performed within this thesis. Some of the events had to be checked by eye to ensure, that no obvious background events appear in the final selection.
The timeline of the ORCA detector, which is presented in Table 5.1, shows that already four DUs are running at present. Thus, it is desired to continue the analysis using data from this configuration. In order to classify the measurement data, Monte Carlo simulations are mandatory, hence it is suggested to focus on the details of the simulations of atmospheric muons within subsequent research.

In the second part of this master project it was tested whether information field theory can help to detect point sources using ANTARES like neutrino data. The main problem is related to the magnitude of the expected fluxes, which are very small. In order to reach a local significance of $3\,\sigma$ a point-source flux of $\Phi_0 = 4.65 \times 10^{-11}\,\mathrm{TeV}^{-1}\,\mathrm{cm}^{-2}\,\mathrm{s}^{-1}$ is required. In comparison to the exemplary point-source flux, given in Equation (3.11), this would require a very bright source. The sky map distributions resulting from the ANTARES public dataset show that in this concrete application an elaborate response model of the detector is required. It also turns out that the correct choice of parameters, e.g. the right value ranges, pixel numbers and hyper-priors, is very challenging.
Further projects applying IFT methods to ANTARES data are currently planned in collaboration with the MPA Garching.

A Appendix

A.1 Data Selecton & Detector Livetime

In the following the details about the used detector data are outlined.

A.1.1 ORCA

In Table A.1 an overview over the different detector configurations and the livetimes of the used run selections are given.

Run Selection	Detector ID	Detection Units	Reco. Version	Livetime
1	00000029	DU2	v0.3, v5.8	78 d
2	00000029	DU2	v5.8	65.36 d
3	00000043	DU1	v5.8_r2	68.48 d
4	00000043	DU3, DU4	v5.9	16.68 d

Table A.1: Overview over the used configurations, livetimes and used data versions for the ORCA data analysis.

The run selection for the single DU analysis was applied from [33], which is associated to the run selection number 1 in the Table A.1, consists of following run configuration names:

```
HV-DARKROOM-TUNED-TM-HRV1500-MHIT-L1-3DS-3DM-ADF2WAV-ORCA02
HV-DARKROOM-TUNED-TM-HRV1500-MHIT-L1-3DS-3DM-MXS-ADF2WAV-ORCA02
HV-DARKROOM-TUNED-TM-HRV1800-MHIT-L1-3DS-3DM-MXS-ADF2WAV-ORCA02
HV-DARKROOM-TUNED-TM-HRV2000-MHIT-L0-3DS-3DM-ADF2WAV-ORCA02
HV-DARKROOM-TUNED-TM-HRV2000-MHIT-L1-3DM-NOPMTIDCHECK-ORCA02
HV-DARKROOM-TUNED-TM-HRV2000-MHIT-L1-3DS-3DM-MXS-ADF
PHYS.1709v1-TUNED.NOPMTCHECK.HRVETO.3D_T
PHYS.1709v2-TUNED.HRV19.3D_T_S
PHYS.1710v2-TUNED.HRV19.3D_T_S_MX.NBMODULES8
PHYS.1710v3-TUNED.HRV19.3D_T_S_MX.NBMODULES5
PHYS.1710v4-TUNED.HRV19.3D_T_S_MX.NBMODULES4
PHYS.1710v5-TUNED.HRV19.3D_T_S_MX.NBMODULES3
PHYS.1710v5-TUNED.HRV19.MX.NBM3.TMAXL20
PHYS.1710v6-TUNED.HRV19.3D_T_S_MX.DEBUG
PHYS.1710v6-TUNED.HRV19.3D_T_S_MX.NBM3.L0
PHYS.1711v1-HVTUNED.TH_MOD_3_PMT.L0
PHYS.1711v1-TUNED.HRV19.3D_T_S_MX_SN
PHYS.1711v2-HVTUNED.HV+TH_MOD_3_PMT.L0
PHYS.1711v2-TUNED.HRV19.3D_T_S_MX_SN
PHYS.1711v3-TUNED.L1_WRITE_20.3D_T_S_MX_SN
PHYS.1711v3-TUNEDSEA.ALL_PMTS_TH_MOD_3_PMT.L0
PHYS.1711v4-TUNED.L1_WRITE_20.3D_T_S_MX_SN
PHYS.1712v1-TUNED.L1_WRITE_20.3D_T_S_MX_SN.ACOU
```

2	3	4	2274	2276	2280	2282	2284	2286	2288	2289	2290	2291	2292
2293	2294	2295	2296	2297	2298	2299	2300	2301	2302	2303	2304	2305	2306
2307	2308	2309	2310	2311	2312	2313	2314	2315	2316	2317	2318	2319	2320
2321	2322	2323	2324	2325	2326	2327	2328	2329	2330	2331	2332	2333	2334
2335	2336	2337	2338	2339	2340	2346	2347	2348	2349	2350	2351	2352	2353
2354	2355	2356	2357	2358	2359	2360	2362	2363	2364	2365	2366	2367	2368
2369	2370	2371	2372	2373	2374	2375	2376	2377	2378	2379	2380	2381	2382
2383	2384	2385	2386	2387	2388	2389	2390	2391	2392	2393	2394	2395	2396
2397	2398	2399	2400	2401	2402	2403	2404	2405	2406	2407	2408	2409	2410
2411	2412	2413	2414	2415	2416	2417	2418	2419	2420	2421	2422	2423	2424
2425	2426	2427	2428	2429	2430	2431	2432	2433	2434	2435	2436	2437	2438
2439	2440	2441	2442	2443	2444	2445	2446	2447	2448	2449	2450	2451	2452
2453	2454	2455	2456	2457	2458	2459	2460	2461	2462	2463	2464	2465	2466
2467	2468	2469	2470	2471	2472	2473	2474	2475	2476	2477	2478	2479	2480
2481	2482	2483	2484	2485	2486	2487	2488	2489	2490	2491	2492	2493	2494
2495	2496	2497	2498	2499	2500	2501	2502	2503	2504	2505	2506	2507	2508
2509	2510	2511	2512	2513	2514	2515	2516	2517	2518	2519	2520	2521	2522
2523	2524	2525	2526	2527	2528	2529	2530	2531	2532	2533	2534	2535	2536
2537	2538	2539	2540	2541	2542	2543	2544	2545	2546	2547	2548	2549	2550
2551	2552	2553	2554	2555	2556	2557	2558	2559	2560	2561	2562	2563	2564
2565	2566	2567	2568	2569	2570	2571	2572	2573	2574	2575	2576	2577	2578
2579	2580	2581	2582	2583	2584	2585	2586	2587	2588	2589	2590	2591	2592
2593	2594	2595	2596	2597	2603	2604	2605	2606	2607	2608	2609	2610	2611
2612	2613	2614	2615	2616	2617	2618	2619	2620	2621	2622	2623	2624	2625
2626	2627	2628	2629	2630	2631	2632	2633	2634	2635	2636	2637	2638	2639
2640	2641	2642	2643	2644	2645	2646	2647	2648	2649	2650	2651	2652	2653
2654	2655	2656	2657	2658	2659	2669	2670	2671	2672	2673	2674	2675	2676
2677	2678	2679	2680	2681	2682	2683	2684	2686	2687	2688	2689	2690	2691
2692	2693	2694	2695	2696	2697	2698	2699	2700	2701	2702	2703	2704	2705
2706	2707	2708	2709	2710	2711	2712	2713	2714	2715	2716	2717	2718	2719
2720	2721	2722	2723	2724	2725	2726	2727	2728	2729	2730	2731	2732	2733
2734	2735	2736	2737	2738	2739	2740	2741	2742	2743	2744	2754	2755	2756
2757	2758	2759	2760	2761	2762	2763	2764	2765	2766	2767	2768	2769	2770
2771	2772	2773	2774	2775	2776	2777	2778	2779	2780	2781	2782	2783	2784
2785	2786	2787	2788	2789	2790	2791	2792	2793	2794	2795	2796	2797	2798
2799	2800	2801	2802	2803	2804	2805	2806	2807	2808	2809	2810	2811	2812
2822	2823	2824	2825	2826	2827	2828	2829	2830	2831	2832	2833	2834	2835
2836	2837	2838	2839	2840	2841	2842	2843	2844	2845	2846	2847	2848	2849
2850	2851	2852	2853	2854	2855	2864	2865	2866	2867	2868	2869	2870	2871
2872	2873	2874	2875	2876	2877	2878	2879	2880	2881	2882	2883	2884	2885
2886	2887	2888	2889	2890	2891	2892	2893	2894	2895	2896	2897	2898	2899
2900	2901	2902	2903	2904	2905	2915	2916	2917	2918	2919	2920	2921	2922
2923	2924	2925	2926	2927	2928	2929	2930	2931	2932	2933	2934	2935	2936
2937	2938	2939	2940	2941	2942	2943	2955	2956	2957	2958	2959	2960	2961
2962	2963	2964	2965	2966	2967	2968	2969	2970	2971	2972	2973	2974	2975
2976	2977	2978	2979	2980	2981	2982	2983	2984	2985	2995	2996	2997	2998
2999	3000	3001	3002	3003	3004	3005	3008	3009	3010	3011	3012	3013	3014
3015	3016	3017	3018	3019	3020	3021	3022	3023	3024	3025	3026	3027	3028
3029	3030	3031	3032	3033	3034	3035	3036	3037	3038	3039	3040	3041	3042
3043	3044	3045	3046	3047	3048	3049	3050	3051	3052	3053	3054	3055	3056
3057	3058	3059	3069	3070	3071	3072	3073	3074	3075	3076	3077	3078	3079
3080	3081	3082	3083	3084	3085	3086	3087	3088	3089	3090	3091	3092	3093
3094	3095	3098	3099	3100	3101	3102	3103	3104	3105	3106	3107	3108	3109
3110	3111	3112	3113	3114	3115	3116	3117	3118	3119	3120	3121	3122	3123
3124	3125	3126	3127	3128	3129	3130	3131	3141	3142	3143	3144	3145	3146
3147	3148	3149	3150	3151	3152	3153	3154	3155	3156	3157	3158	3159	3160
3161	3162	3163	3164	3165	3166	3167	3168	3169	3170	3171	3172	3173	3174
3175	3176	3177	3178	3179	3180	3181	3182	3183	3184	3185	3186	3187	3188
3189	3190	3191	3192	3193	3194	3195	3196	3197	3198	3199	3200	3201	3202
3203	3204	3205	3206	3207	3208	3209	3210	3211	3212	3213	3214	3215	3216
3217	3218	3219	3229	3230	3231	3232	3233	3234	3235	3236	3237	3238	3239
3240	3241	3242	3243	3244	3245	3246	3247	3248	3249	3250	3251	3252	3253
3254	3255	3256	3257	3258									

Table A.2: Run list of the selection 1 (see Table A.1).

The run configuration names for the run selection number 2:

```
PHYS.1711v1-TUNED.HRV19.3D_T_S_MX_SN
PHYS.1711v4-TUNED.L1_WRITE_20.3D_T_S_MX_SN
PHYS.1710v4-TUNED.HRV19.3D_T_S_MX.NBMODULES4
PHYS.1709v2-TUNED.HRV19.3D_T_S
PHYS.1711v3-TUNED.L1_WRITE_20.3D_T_S_MX_SN
PHYS.1710v2-TUNED.HRV19.3D_T_S_MX.NBMODULES8
PHYS.1710v3-TUNED.HRV19.3D_T_S_MX.NBMODULES5
PHYS.1709v1-TUNED.NOPMTCHECK.HRVETO.3D_T
PHYS.1711v2-TUNED.HRV19.3D_T_S_MX_SN
PHYS.1710v5-TUNED.HRV19.3D_T_S_MX.NBMODULES3
```

2424	2425	2426	2427	2428	2429	2430	2433	2434	2437	2438	2439	2440	2441
2442	2443	2444	2445	2446	2447	2448	2449	2450	2454	2455	2456	2457	2458
2459	2460	2461	2462	2463	2465	2466	2467	2468	2469	2470	2471	2473	2474
2477	2478	2479	2480	2481	2482	2483	2484	2485	2486	2487	2488	2489	2490
2491	2492	2493	2494	2495	2496	2497	2498	2499	2500	2503	2504	2505	2507
2508	2509	2514	2515	2520	2521	2522	2523	2525	2527	2528	2529	2530	2531
2532	2533	2534	2536	2537	2538	2540	2541	2542	2543	2544	2545	2546	2547
2549	2550	2551	2552	2553	2554	2555	2556	2557	2558	2559	2562	2564	2566
2567	2568	2569	2570	2571	2572	2573	2574	2575	2576	2577	2578	2579	2580
2581	2582	2583	2584	2585	2586	2587	2588	2589	2590	2592	2596	2597	2606
2607	2608	2609	2610	2611	2612	2613	2614	2615	2616	2617	2619	2620	2621
2622	2623	2624	2625	2626	2627	2629	2630	2631	2632	2633	2634	2635	2637
2638	2639	2640	2642	2643	2644	2645	2646	2647	2649	2650	2652	2654	2655
2656	2657	2658	2659	2673	2678	2683	2687	2688	2689	2690	2691	2692	2693
2694	2695	2696	2699	2700	2701	2702	2703	2708	2709	2712	2713	2714	2715
2716	2717	2719	2721	2722	2723	2724	2725	2726	2727	2729	2730	2731	2732
2733	2734	2735	2737	2740	2741	2742	2743	2744	2756	2758	2759	2760	2761
2762	2765	2766	2767	2768	2770	2771	2772	2773	2774	2775	2776	2777	2778
2779	2781	2782	2783	2784	2785	2786	2787	2788	2789	2790	2791	2792	2793
2794	2795	2796	2797	2798	2799	2800	2801	2802	2803	2804	2805	2806	2807
2808	2809	2811	2812	2826	2827	2828	2829	2831	2832	2833	2834	2840	2841
2843	2844	2845	2848	2849	2850	2852	2864	2865	2867	2868	2869	2870	2871
2872	2879	2882	2883	2884	2886	2887	2888	2889	2890	2892	2893	2894	2895
2896	2897	2898	2899	2900	2901	2902	2903	2904	2905	2919	2920	2921	2922
2923	2924	2925	2926	2927	2928	2933	2934	2935	2936	2937	2938	2939	2940
2941	2943	2956	2957	2958	2959	2960	2961	2962	2963	2964	2965	2966	2967
2968	2969	2970	2971	2972	2973	2974	2975	2976	2977	2978	2979	2980	2981
2982	2983	2984	2985	2998	2999	3000	3001	3002	3003	3004	3005	3009	3010
3011	3012	3013	3014	3015	3016	3018	3019	3020	3021	3022	3023	3024	3029
3030	3031	3032	3033	3034	3035	3036	3037	3038	3039	3040	3041	3043	3044
3047	3048	3049	3051	3054	3055	3057	3059	3072	3073	3075	3076	3077	3078
3079	3080	3081	3082	3083	3084	3086	3089	3090	3091	3092	3093	3100	3101
3102	3103	3104	3105	3106	3107	3108	3109	3110	3111	3112	3113	3114	3115
3116	3117	3118	3119	3120	3121	3122	3123	3124	3125	3126	3127	3128	3129
3131	3166	3167	3168	3169	3170	3173	3174	3175	3177	3179	3180	3181	3182
3183	3184	3185	3186	3187	3188	3189	3190	3191	3192	3193	3194	3195	3196
3198	3199	3201	3202	3203	3204	3205	3207	3208	3210	3211	3212	3214	3218
3232	3233	3234	3235	3236	3237	3238	3241	3243	3244	3245	3246	3247	3248
3249													

Table A.3: Run list of the selection 2 (see Table A.1).

The run configuration names for the run selection number 3:

```
PHYS.1903v3-TUNEDSEA.190308-ACOU4Waves-L1-ADF.DUMP.SELECTED
PHYS.1903v1-TUNEDSEA.190308-ACOU4Waves-AllTrigger-L1
PHYS.1902v3-TUNED.HV.DR-ACOU4Waves-AllTrigger-L1
PHYS.1904v3-TUNEDSEA.190308-ACOU4Waves-AllTrigger-L1.20-Mod_Th
PHYS.1904v2-TUNEDSEA.190308-ACOU4Waves-AllTrigger-L1-Mod_Th
PHYS.1903v2-TUNEDSEA.190308-ACOU4Waves-AllTrigger-L1
PHYS.1904v1-TUNEDSEA.190308-ACOU4Waves-AllTrigger-L1.20
```

4127	4132	4135	4136	4137	4138	4143	4149	4155	4157	4162	4165	4166	4169
4172	4174	4176	4178	4179	4202	4203	4204	4206	4216	4217	4218	4219	4220
4221	4222	4223	4224	4225	4226	4227	4228	4230	4231	4233	4236	4238	4241
4242	4243	4245	4251	4252	4255	4256	4257	4258	4260	4263	4264	4272	4273
4274	4275	4276	4277	4278	4279	4280	4281	4282	4288	4290	4291	4292	4293
4294	4295	4296	4297	4298	4299	4300	4301	4302	4303	4304	4305	4306	4307
4308	4309	4310	4311	4312	4313	4315	4316	4317	4318	4319	4320	4321	4322
4323	4324	4325	4326	4327	4328	4329	4330	4331	4332	4333	4335	4345	4346
4347	4348	4349	4350	4351	4352	4353	4354	4355	4356	4357	4358	4359	4360
4361	4362	4365	4366	4367	4368	4369	4370	4371	4372	4373	4374	4375	4376
4377	4378	4379	4380	4381	4382	4385	4386	4387	4388	4389	4390	4391	4392
4393	4394	4395	4396	4397	4398	4399	4400	4401	4402	4403	4404	4405	4406
4407	4408	4409	4410	4411	4412	4413	4414	4415	4416	4417	4418	4419	4420
4421	4422	4423	4424	4425	4426	4427	4428	4429	4430	4431	4432	4433	4434
4435	4436	4437	4438	4439	4440	4445	4446	4447	4448	4449	4450	4451	4452
4453	4454	4455	4456	4457	4458	4459	4460	4461	4462	4463	4464	4465	4466
4467	4468	4469	4470	4471	4472	4473	4474	4475	4476	4477	4478	4479	4480
4481	4483	4485	4486	4487	4488	4489	4490	4491	4492	4493	4494	4495	4496
4497	4498	4499	4500	4501	4502	4506	4507	4508	4509	4510	4511	4512	4513
4514	4515	4516	4517	4518	4519	4520	4521	4524	4525	4526	4527	4528	4529
4530	4531	4532	4533	4534	4535	4536	4537	4538	4539	4540	4541	4542	4543
4544	4545	4546	4547	4548	4549	4550	4551	4552	4553	4554	4555	4556	4557
4558	4559	4560	4561	4562	4566	4567	4568	4569	4570	4571	4572	4573	4574
4575	4576	4577	4578	4579	4580	4581	4582	4583	4584	4585	4586	4587	4588
4589	4590	4591	4592	4593	4594	4595	4596	4597	4598	4599	4600	4601	4602
4603	4604	4605	4606	4607	4611	4612	4613	4614	4615	4616	4617	4618	4619
4620	4621	4622	4623	4624	4625	4626	4627	4628	4629	4630	4631	4632	4633
4634	4635	4636	4637	4638	4642	4643	4644	4645	4646	4647	4648	4649	4652
4653	4654	4658	4659	4660	4661	4662	4663	4664	4665	4666	4667	4668	4669
4670	4671	4672	4676	4677	4678	4679	4680	4681	4682	4683	4684	4685	4686
4687	4688	4689	4690	4691	4692	4693	4694	4695	4696	4697	4698	4699	4700
4701	4702	4703	4707	4708	4709	4710	4711	4712	4713	4714	4715	4716	

Table A.4: Run list of the selection 3 (see Table A.1).

For the two DU detector configuration all available runs have been used, which run ids are given in Table A.5.

4793	4888	5038	5032	4840	4982	4833	4954	4895	4905	4813	4913	4864	5035
4879	4896	4971	4942	4835	4807	4960	4919	4966	4928	5025	4801	5042	4892
4936	4842	4887	4901	5033	5007	4884	5058	4868	4980	4970	5062	4874	4803
5037	4984	4939	5056	5026	4994	5051	5047	4809	4897	4972	5006	4806	4976
4882	4983	4862	4845	5002	4908	5060	4974	4986	5005	5023	4805	4894	4883
4878	5001	4869	4945	4998	5017	4924	5034	4995	4959	4875	5022	4933	4880
4949	4808	4967	4787	4917	4859	4996	4873	4904	4863	4786	4963	4792	5057
4856	5010	4929	5052	4906	4981	4885	4990	5043	4961	4973	4802	4975	4890
4889	4962	5054	5009	5045	4938	5020	4903	4871	4946	4789	4997	5029	5027
4804	4902	4969	4931	5061	5046	4926	4943	4838	4977	4947	4930	4927	4900
4940	4867	4920	4898	5053	4993	4886	4810	5028	4836	4944	5059	5055	4925
5063	4899	4991	4788	4989	4987	4932	4865	4979	4948	4988	4955	5004	4855
4837	4958	5008	5011	4985	5031	4893	4891	4952	5024	4814	4791	5000	5018
4876	4858	5064	4999	5048	4790	5041	4978	4964	5036	5019	5021	4866	5049
4857	4957	5039	5003	5040	4800	4937	4839	5050	5030	4992	4881	4834	4956
4941													

Table A.5: Run list of the selection 4 (see Table A.1).

A.2 Position Map

In Figure A.1 the map with marked locations of the KM3NeT/ORCA and the ANTARES detector are shown.

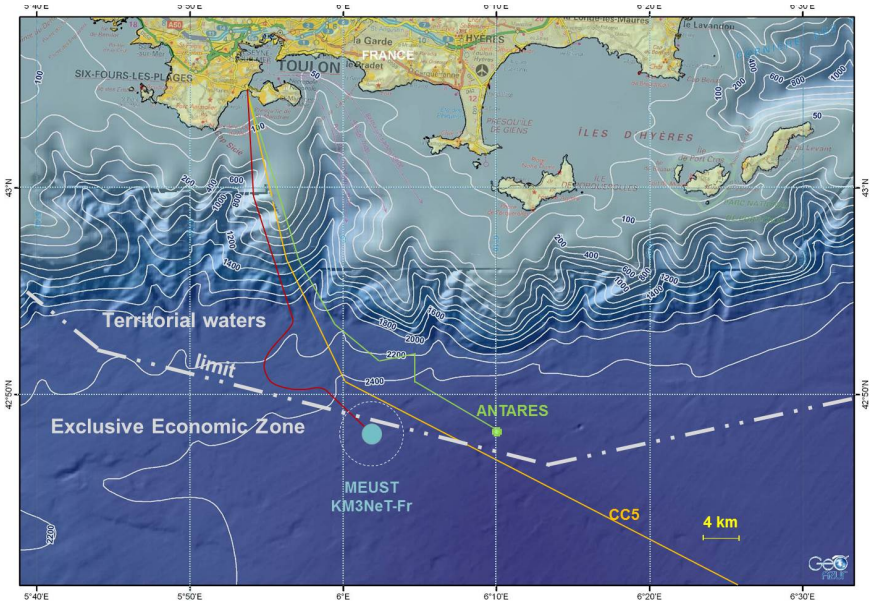

Figure A.1: Map showing the detector locations of ANTARES and KM3NeT/ORCA at the french coast near the city of Toulon. Contour lines indicating the depth of the seafloor. Taken from [40].

A.3 KM3Flux

In this part the complementary set of plots of the flattened flux interpolations outlined in Section 6.2.2 are given.

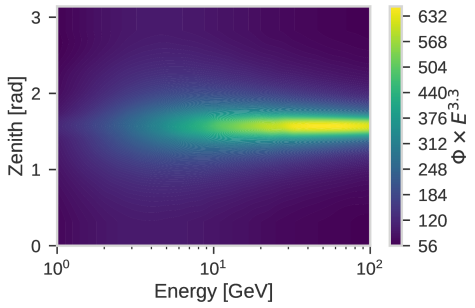

(a) Atmospheric ν_e flux

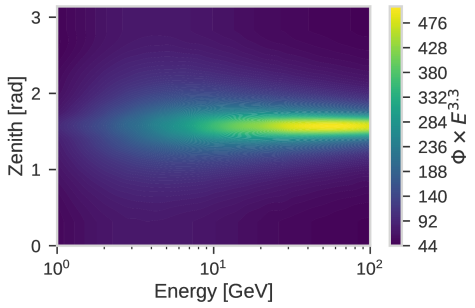

(b) Atmospheric $\bar{\nu}_e$ flux

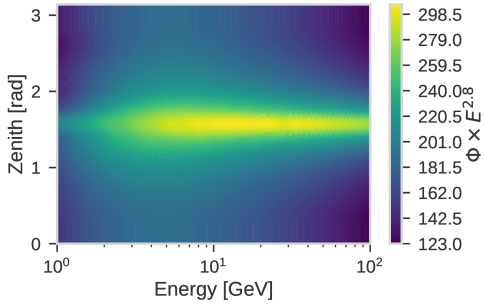

(c) Atmospheric ν_μ flux

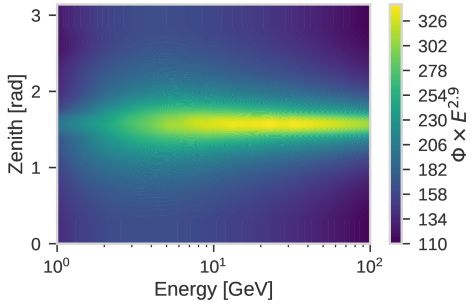

(d) Atmospheric $\bar{\nu}_\mu$ flux

Figure A.2: Interpolated flattened neutrino flux over zenith and energy for the different neutrino types generated in the atmosphere based on the measurements taken in Frejus at solar minimum.

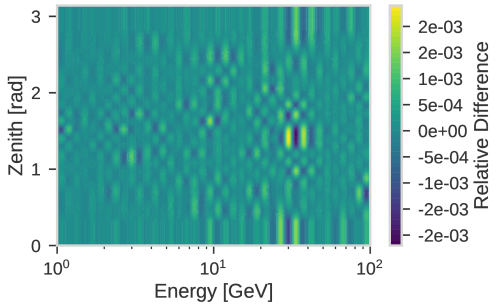

(a) ν_e

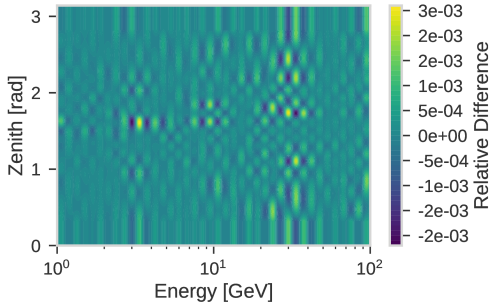

(b) $\bar{\nu}_e$

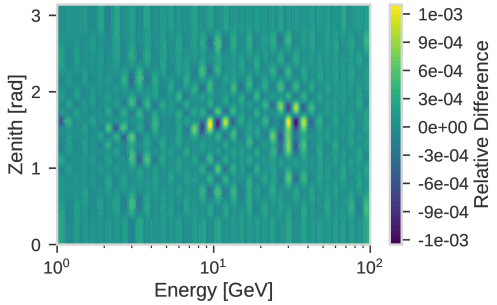

(c) ν_μ

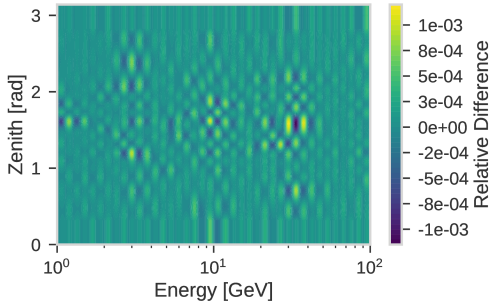

(d) $\bar{\nu}_\mu$

Figure A.3: Relative differences of the neutrino flux interpolation with and without the flattening applied for the different neutrino types generated in the atmosphere based on the measurements taken in Frejus at solar minimum [34].

A.4 Simulation Discrepancies

In order to check the data for obvious unphysical content, which would lead to destroy the physical output, various parameters have been studied. Within the azimuth distribution of the neutrino Monto-Carlo simulations of the two DU configuration, the distribution shown in Figure A.4 was identified. As the notch in the distribution covers about 180°, this distribution would indicate a single-sided increased sensitivity of the detector. As such a distribution is at least

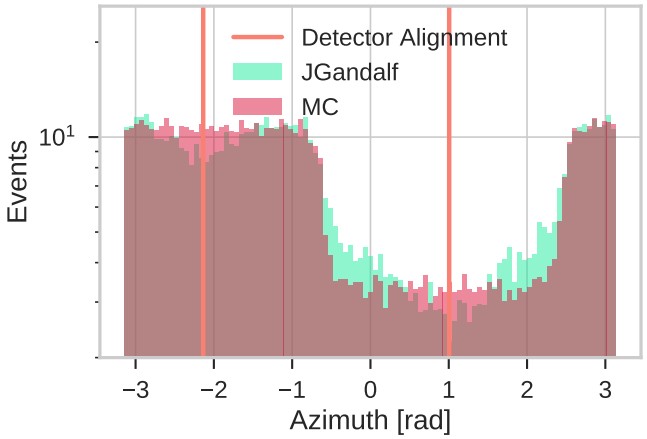

Figure A.4: Azimuth distribution of the simulated neutrino events with the Monte-Carlo truth and the best JGandalf reconstruction.

notable, it is traced back along the different simulation stages. In Figure A.5 the distribution of the neutrino generator and the triggered events after the detector simulation is shown. The

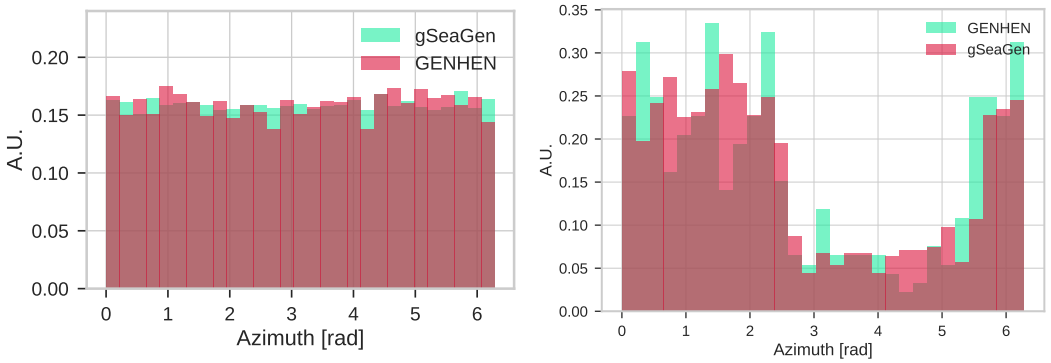

Figure A.5: Azimuth distribution of two exemplary event generation files (left) and triggered files after the light generation (right) for both types of neutrino generators.

problem has been reported in the analysis section of the ELOG with the ticket number 540.

A.5 Event Identities

In this section the unique event identities according the presented selections are listed.

A.5.1 One-DU Configuration

Run	Event	Run	Event	Run	Event	Run	Event	Run	Event
2290	5585	2293	210	2441	16072	2546	9043	2555	1353
2609	3665	2623	5161	2658	5579	2689	20299	2722	12065
2884	14120	2904	8711	2965	13608	2973	11163	3012	21459
3035	17577	3035	17967	3086	19454	3089	11477	3174	12158
3201	13108								

Table A.6: Run IDs and event IDs of the neutrino candidate events resulting from the preceding selection using v0.3 (see Section 7.2).

Run	Event	Run	Event	Run	Event	Run	Event	Run	Event
2289	1315	2290	5585	2291	1406	2293	210	2305	5431
2314	4185	2441	16072	2491	1173	2546	9043	2555	1353
2609	3665	2623	5161	2658	5579	2689	20299	2722	12065
2884	14120	2904	8711	2959	17637	2965	13608	2973	11163
3012	21459	3035	17577	3035	17967	3086	19454	3089	11477
3174	12158	3201	13108						

Table A.7: Run IDs and event IDs of the neutrino candidate events resulting from the preceding selection with loosened $\langle z_{\mathrm{trg}} \rangle$ using v0.3 (see Section 7.2).

Run	Event	Run	Event	Run	Event	Run	Event	Run	Event
2290	5585	2293	210	2441	16072	2484	2649	2488	16182
2508	12916	2546	9043	2555	1353	2609	3665	2623	5161
2658	5579	2689	20299	2690	15084	2722	12065	2849	5989
2884	14120	2904	8711	2965	13608	2973	11163	3012	21459
3035	17577	3035	17967	3086	19454	3089	11477	3121	8326
3169	5587	3174	12158	3177	13251	3201	13108	3233	17541

Table A.8: Run IDs and event IDs of the neutrino candidate events resulting from the preceding selection with loosened r_{vertex} using v0.3 (see Section 7.2).

Run	Event	Run	Event	Run	Event	Run	Event	Run	Event
2290	5585	2293	210	2355	6540	2370	3209	2400	12151
2441	16072	2524	15786	2546	9043	2555	1353	2570	6330
2609	3665	2623	5161	2658	5579	2689	20299	2703	1107
2722	12065	2871	4804	2884	14120	2885	16275	2889	3988
2904	8711	2926	54	2926	22526	2965	6453	2965	13608
2973	11163	3000	8064	3012	21459	3035	17577	3035	17967
3086	19454	3089	11477	3174	12158	3201	13108	3247	19367

Table A.9: Run IDs and event IDs of the neutrino candidate events resulting from the preceding selection with loosened downgoing mask using v0.3 (see Section 7.2).

Run	Event	Run	Event	Run	Event	Run	Event	Run	Event
2290	5585	2293	210	2441	16072	2522	17971	2546	9043
2555	1353	2609	3665	2623	5161	2658	5579	2689	20299
2722	12065	2730	2853	2732	11912	2740	6604	2884	14120
2896	14020	2904	8711	2965	13608	2973	11163	3012	21459
3035	17577	3035	17967	3086	19454	3089	11477	3174	12158
3201	13108								

Table A.10: Run IDs and event IDs of the neutrino candidate events resulting from the preceding selection with loosened $\mathcal{L}_{\mathrm{Up}}$ using v0.3 (see Section 7.2).

Run	Event	Run	Event	Run	Event	Run	Event	Run	Event
2290	5585	2293	210	2430	17031	2441	16072	2443	6826
2450	7351	2480	7074	2503	9778	2522	7048	2538	18338
2543	11827	2546	945	2546	9043	2555	1353	2609	3665
2623	5161	2636	10279	2658	5579	2689	20299	2722	12065
2725	20923	2735	2275	2743	19117	2759	12750	2803	13658
2811	13222	2827	7570	2843	6789	2872	5566	2884	14120
2904	8711	2965	13608	2968	21533	2973	11163	2975	3972
2982	9192	3012	21459	3028	14609	3031	9973	3035	17577
3035	17967	3086	19454	3089	11477	3092	18306	3099	5647
3106	20265	3130	1525	3174	12158	3201	13108	3201	19152
3215	11432	3218	2940	3233	22373	3234	4140		

Table A.11: Run IDs and event IDs of the neutrino candidate events resulting from the preceding selection with loosened $\mathcal{L}_{\mathrm{Up}} - \mathcal{L}_{\mathrm{Down}}$ using v0.3 (see Section 7.2).

Run	Event	Run	Event	Run	Event	Run	Event	Run	Event
2290	5585	2293	210	2300	2938	2354	5442	2441	16072
2489	19297	2546	9043	2555	1353	2609	3665	2623	5161
2643	15953	2658	5579	2689	20299	2722	12065	2884	14120
2904	8711	2918	16983	2965	13608	2973	11163	3012	21459
3035	17577	3035	17967	3086	19454	3089	11477	3165	7725
3174	12158	3201	13108	3231	12940				

Table A.12: Run IDs and event IDs of the neutrino candidate events resulting from the preceding selection with loosened maximum ToT threshold using v0.3 (see Section 7.2).

Run	Event	Run	Event	Run	Event	Run	Event	Run	Event
2290	5585	2293	210	2300	2938	2354	5442	2380	3746
2441	16072	2489	19297	2546	9043	2555	1353	2609	3665
2623	5161	2636	14553	2643	15953	2658	5579	2689	20299
2713	1743	2722	12065	2760	12370	2884	14120	2904	8711
2918	16983	2965	13608	2973	11163	3012	21459	3035	17577
3035	17967	3074	8647	3086	19454	3089	11477	3099	19278
3165	7725	3174	12158	3201	13108	3231	12940	3249	3216

Table A.13: Run IDs and event IDs of the neutrino candidate events resulting from the preceding selection with loosened general ToT threshold mask using v0.3 (see Section 7.2).

Run	Event	Run	Event	Run	Event	Run	Event	Run	Event
2555	1353	2627	14749	2689	20298	2690	15083	2722	12064
2884	14121	2889	3988	2904	8711	2965	13608	2973	11161
3012	21459	3035	17577	3035	17967	3086	19453	3089	11475
3174	12158	3177	13251	3231	17219				

Table A.14: Run IDs and event IDs of the neutrino candidate events resulting from the preceding selection using v5.8 (see Section 7.2).

Run	Event	Run	Event	Run	Event	Run	Event	Run	Event
2555	1353	2627	14749	2689	20298	2690	15083	2722	12064
2884	14121	2889	3988	2904	8711	2930	10479	2965	13608
2973	11161	3012	21459	3035	17577	3035	17967	3086	19453
3089	11475	3174	12158	3177	13251	3231	17219		

Table A.15: Run IDs and event IDs of the neutrino candidate events resulting from the preceding selection with loosened $\langle z_{\mathrm{trg}} \rangle$ using v5.8 (see Section 7.2).

Run	Event	Run	Event	Run	Event	Run	Event	Run	Event
2458	20446	2484	2648	2555	1353	2580	16573	2627	14749
2658	20523	2689	20298	2690	15083	2722	12064	2724	694
2771	22175	2849	5990	2884	14121	2889	3988	2904	8711
2965	13608	2970	7499	2973	11161	2997	17977	3012	21459
3035	17577	3035	17967	3086	19453	3089	11475	3169	5587
3174	12158	3177	13251	3231	17219				

Table A.16: Run IDs and event IDs of the neutrino candidate events resulting from the preceding selection with loosened r_{vertex} using v5.8 (see Section 7.2).

Run	Event	Run	Event	Run	Event	Run	Event	Run	Event
2555	1353	2623	5161	2627	14749	2689	20298	2690	15083
2703	1107	2722	12064	2884	14121	2889	3988	2904	8711
2926	54	2965	13608	2973	11161	3012	21459	3035	17577
3035	17967	3086	19453	3089	11475	3174	12158	3177	13251
3201	13110	3231	17219	3247	19372				

Table A.17: Run IDs and event IDs of the neutrino candidate events resulting from the preceding selection with loosened downgoing mask using v5.8 (see Section 7.2).

Run	Event	Run	Event	Run	Event	Run	Event	Run	Event
2555	1353	2627	14749	2689	20298	2690	15083	2722	12064
2740	6605	2884	14121	2889	3988	2904	8711	2965	13608
2973	11161	3012	21459	3035	17577	3035	17967	3043	6956
3086	19453	3089	11475	3174	12158	3177	13251	3231	17219
3234	4770								

Table A.18: Run IDs and event IDs for the neutrino candidate events resulting from the preceding selection with loosened $\mathcal{L}_{\mathrm{Up}}$ using v5.8 (see Section 7.2).

Run	Event	Run	Event	Run	Event	Run	Event	Run	Event
2430	17032	2440	7679	2462	20388	2503	9775	2527	22966
2538	18336	2543	11827	2546	945	2555	1353	2627	14749
2636	3875	2689	20298	2690	15083	2722	12064	2725	20923
2811	13222	2826	11149	2827	7570	2872	5566	2884	14121
2889	3988	2904	8711	2925	13196	2965	13608	2968	21533
2973	11161	3012	21459	3028	14609	3031	9973	3035	17577
3035	17967	3037	13696	3086	19453	3089	11475	3099	5647
3130	5844	3174	12158	3177	13251	3190	3354	3195	22032
3201	19153	3231	17219	3233	22372	3241	5184		

Table A.19: Run IDs and event IDs of the neutrino candidate events resulting from the preceding selection with loosened $\mathcal{L}_{\mathrm{Up}} - \mathcal{L}_{\mathrm{Down}}$ using v5.8 (see Section 7.2).

Run	Event	Run	Event	Run	Event	Run	Event	Run	Event
2489	19297	2555	1353	2627	14749	2689	20298	2690	15083
2713	1743	2722	12064	2884	14121	2889	3988	2904	8711
2918	16984	2965	13608	2973	11161	3012	21459	3035	17577
3035	17967	3086	19453	3089	11475	3165	7724	3174	12158
3177	13251	3231	17219						

Table A.20: Run IDs and event IDs of the neutrino candidate events resulting from the preceding selection with loosened maximum ToT threshold using v5.8 (see Section 7.2).

Run	Event	Run	Event	Run	Event	Run	Event	Run	Event
2489	19297	2555	1353	2627	14749	2655	11284	2689	20298
2690	15083	2713	1743	2722	12064	2760	12369	2829	20445
2851	4807	2884	14121	2889	3988	2904	8711	2918	16984
2965	13608	2973	11161	3012	21459	3035	17577	3035	17967
3086	19453	3089	11475	3165	7724	3174	12158	3177	13251
3231	17219	3249	3215						

Table A.21: Run IDs and event IDs of the neutrino candidate events resulting from the preceding selection with loosened general ToT threshold mask using v5.8 (see Section 7.2).

Run	Event	Run	Event	Run	Event	Run	Event	Run	Event
2430	17032	2438	14431	2439	280	2448	7772	2458	2455
2458	3486	2484	9633	2488	4396	2489	16097	2491	4096
2492	1314	2495	3876	2514	8165	2521	14832	2521	17464
2534	6620	2564	4900	2564	8897	2574	9662	2579	9048
2583	20583	2590	14255	2613	22751	2624	20476	2633	14182
2635	7072	2637	14072	2654	9478	2655	19356	2656	2274
2657	6803	2658	5579	2696	16781	2735	15421	2740	15070
2741	10411	2768	16041	2771	21806	2773	16820	2782	6831
2787	18965	2787	19618	2797	11995	2797	12790	2806	5407
2807	2286	2807	19980	2829	10022	2844	1033	2845	5251
2848	13968	2852	3680	2852	10127	2852	15181	2864	10227
2867	9973	2871	13738	2888	8223	2890	3872	2904	9896
2926	54	2934	3845	2936	13903	2943	18676	2957	3866
2957	13766	2957	15624	2958	12791	2963	11308	2975	5640
2975	19850	2976	4307	2980	20668	2984	17720	2999	3852
3005	0	3005	5590	3009	17335	3021	19608	3022	19854
3041	3216	3059	8123	3080	6134	3090	5567	3090	11876
3104	3483	3107	8688	3108	21171	3111	3459	3112	8701
3127	4682	3128	6477	3168	6091	3169	5587	3173	2532
3180	3619	3187	1409	3192	7273	3194	2043	3205	3093
3208	3128	3208	9296	3210	12689	3212	14313	3235	10918
3249	19430	4135	17806	4157	25983	4162	9378	4162	12254
4166	5843	4203	11596	4206	8878	4218	19359	4218	19538
4218	20943	4218	21587	4219	3279	4222	20255	4226	12888
4264	9676	4282	15425	4282	15713	4291	3301	4295	17146
4307	2580	4309	24124	4310	17076	4312	15479	4315	20500
4316	16502	4318	5668	4319	2567	4323	19932	4328	246
4331	3857	4332	24992	4345	15396	4357	9104	4360	2805
4360	8328	4366	17900	4371	10518	4372	1804	4373	4908
4378	16895	4379	6153	4379	18844	4382	18332	4390	8173
4391	14672	4393	20177	4394	8557	4403	16539	4408	2964
4411	7495	4414	19663	4415	2051	4424	16918	4427	4714
4429	8742	4431	17821	4434	16858	4437	14389	4438	4155
4460	19226	4462	10705	4468	9531	4478	2047	4479	22572
4491	20890	4491	22315	4493	11808	4501	15526	4507	19180
4511	20644	4513	17315	4519	22994	4541	20148	4547	832
4547	3579	4549	12620	4553	14599	4556	20652	4566	16275
4577	20712	4581	8305	4592	22084	4598	10188	4601	47871
4602	35880	4607	33084	4607	40059	4612	12098	4614	24195
4620	42052	4622	44831	4623	36498	4623	47020	4624	25306
4627	3741	4630	24941	4631	13166	4633	16944	4633	26085
4634	14858	4634	43685	4636	19640	4644	35862	4644	45857
4648	3748	4648	12933	4658	25032	4659	11895	4659	37626
4660	16027	4662	36182	4664	28900	4664	50412	4666	555
4666	3008	4667	34089	4667	49510	4668	19187	4670	34374
4671	14398	4671	15966	4685	27469	4687	8073	4693	16014
4693	39840	4696	39520	4709	23034	4711	13422	4712	23088

Table A.22: Run IDs and event IDs of the neutrino candidate events resulting from the geometric selection (see Section 7.4).

Run	Event	Run	Event	Run	Event	Run	Event	Run	Event
2442	9027	2480	6729	2515	15108	2627	17517	2689	20298
2690	15083	2793	19396	2844	12405	2849	5990	2926	54
2971	10161	3015	19638	3029	11648	3057	16531	3078	13029
3126	11107	3177	13251	3201	4048	3202	1581	4157	15880
4222	20255	4242	8183	4263	4399	4282	15425	4322	10789
4360	8328	4407	14227	4470	4195	4472	7974	4603	40789
4619	31335	4654	12119	4677	37634	4709	30722		

Table A.23: Run IDs and event IDs of the neutrino candidate events resulting from the quality selection (see Section 7.5).

Run	Event	Run	Event	Run	Event	Run	Event	Run	Event
2430	17032	2461	20506	2462	20388	2478	5395	2543	11827
2550	10102	2574	9662	2608	9201	2609	3666	2613	22751
2629	6414	2658	5579	2658	10678	2689	20298	2690	15083
2712	23106	2722	12064	2743	19116	2849	5990	2872	5566
2898	10099	2926	54	2957	3866	2973	11161	2976	4307
2979	1626	3015	4326	3031	9973	3089	20098	3112	19994
3113	19292	3169	5587	3177	13251	3177	16812	3181	15857
3201	13110	3212	18827	3241	14411	4149	13327	4157	15880
4204	19869	4222	20255	4226	12888	4230	17766	4242	8183
4263	4399	4282	15425	4323	19154	4326	1704	4331	3857
4360	8328	4381	3137	4413	17715	4418	8792	4424	16918
4433	6459	4452	20724	4456	17829	4460	19226	4491	20890
4492	11221	4519	8332	4550	21599	4572	13726	4596	30917
4614	24195	4619	31335	4630	2579	4634	14858	4659	11895
4677	37634	4687	44987	4693	16014	4693	39840	4714	49664

Table A.24: Run IDs and event IDs of the neutrino candidate events resulting from the custom selection (see Section 7.6).

A.5.2 Two-DU Configuration

Run	Event	Run	Event	Run	Event	Run	Event	Run	Event
4836	16354	4876	6581	4885	27610	4890	14476	4893	6095
5018	8787	5031	515						

Table A.25: Run IDs and event IDs of the neutrino candidate events resulting from the preceding selection (see Section 8.1).

Run	Event	Run	Event	Run	Event	Run	Event	Run	Event
4786	14547	4804	30445	4806	23126	4836	16354	4838	16072
4840	1350	4840	9602	4865	9840	4867	18452	4876	6581
4883	21247	4885	27610	4890	14476	4893	6095	4895	5318
4897	12218	4903	6450	4904	15753	4925	14790	4926	17558
4975	13767	4982	10744	4983	8141	4985	19865	4994	13719
4996	24155	5011	27894	5018	8787	5021	28046	5022	27459
5029	19635	5031	515	5037	13803	5060	12730		

Table A.26: Run IDs and event IDs of the neutrino candidate events resulting from the preceding selection with loosened limits (see Section 8.1).

Run	Event	Run	Event	Run	Event	Run	Event	Run	Event
4804	30445	4806	23126	4840	9602	4867	18452	4885	27610
4892	22072	4897	12218	4903	6450	4925	14790	4948	6651
4959	25505	4982	10744	4983	8141	4996	24155	5007	15932
5018	8787	5021	28046	5022	27459	5031	515	5037	13803

Table A.27: Run IDs and event IDs of the neutrino candidate events resulting from the custom selection (see Section 8.2).

Bibliography

[1] http://microboone-docdb.fnal.gov/cgi-bin/RetrieveFile?docid=953;filename=pauli%20letter1930.pdf.

[2] B. Pontecorvo, "Mesonium and antimesonium." *Zhur. Eksptl'. i Teoret. Fiz.* 33 (1957).

[3] https://www.nobelprize.org/prizes/physics/2015/press-release/.

[4] V. F. Hess, "Über Beobachtungen der durchdringenden Strahlung bei sieben Freiballonfahrten." *Physikalische Zeitschrift* 13 (November, 1912) 1084–1091.

[5] J. A. Formaggio and G. P. Zeller, "From ev to eev: Neutrino cross sections across energy scales." *Rev. Mod. Phys.* 84 (Sep, 2012) 1307–1341.

[6] Particle Data Group Collaboration, C. Patrignani *et al.*, "Review of Particle Physics." *Chin. Phys.* C40 no. 10, (2016) 100001.

[7] B. T. Cleveland, T. Daily, J. Raymond Davis, J. R. Distel, K. Lande, C. K. Lee, P. S. Wildenhain, and J. Ullman, "Measurement of the solar electron neutrino flux with the homestake chlorine detector." *The Astrophysical Journal* 496 no. 1, (Mar, 1998) 505–526.

[8] http://www.nu-fit.org/?q=node/166.

[9] L. Wolfenstein, "Neutrino oscillations in matter." *Phys. Rev. D* 17 (May, 1978) 2369–2374.

[10] S. P. Mikheyev and A. Y. Smirnov, "Resonant amplification of ν oscillations in matter and solar-neutrino spectroscopy." *Il Nuovo Cimento C* 9 no. 1, (Jan., 1986) 17–26.

[11] A. M. Dziewonski and D. L. Anderson, "Preliminary reference earth model." *Physics of the Earth and Planetary Interiors* 25 no. 4, (1981) 297 – 356.

[12] U. Katz and C. Spiering, "High-energy neutrino astrophysics: Status and perspectives." *Progress in Particle and Nuclear Physics* 1260 (12, 2011).

[13] https://cosmic.lbl.gov/SKliewer/Cosmic_Rays/Atmosphere.htm.

[14] J. P. Yañez and A. Kouchner, "Measurement of atmospheric neutrino oscillations with very large volume neutrino telescopes." *Adv. High Energy Phys.* 2015 (2015) 271968, arXiv:1509.08404.

[15] E. V. Bugaev, A. Misaki, V. A. Naumov, T. S. Sinegovskaya, S. I. Sinegovsky, and N. Takahashi, "Atmospheric muon flux at sea level, underground, and underwater." *Phys. Rev. D* 58 (Jul, 1998) 054001.

[16] G. Carminati, A. Margiotta, and M. Spurio, "Atmospheric MUons from PArametric formulas: A Fast GEnerator for neutrino telescopes (MUPAGE)." *Comput. Phys. Commun.* 179 (2008) 915–923, arXiv:0802.0562.

[17] E. Fermi, "On the Origin of the Cosmic Radiation." *Phys. Rev.* 75 (1949) 1169–1174.

[18] T. Piran, "Gamma-ray bursts and the fireball model." *Phys. Rept.* 314 (1999) 575–667, arXiv:astro-ph/9810256.

[19] T. A. Enßlin, "Information theory for fields." *Annalen Phys.* 531 no. 3, (2019) 1800127, arXiv:1804.03350.

[20] J. Knollmüller and T. A. Enßlin, "Metric gaussian variational inference." 2019.

[21] S. Hutschenreuter and T. A. Enßlin, "The galactic faraday depth sky revisited." 2019.

[22] J. Reubelt, *Hardware studies, in-situ prototype calibration and data analysis of the novel multi-PMT digital optical module for the KM3NeT neutrino telescope.* doctoralthesis, Friedrich-Alexander-Universität Erlangen-Nürnberg (FAU), 2019.

[23] http://users.ictp.it/~smr2246/monday/tiffenberg-NUSKY.pdf.

[24] J. Brunner, "*Simulation of* ^{40}K *signals*." ANTARES internal note (ANTARES-Site/1999-002), 1999.

[25] ANTARES Collaboration, V. Van Elewyck, "Recent results from the ANTARES neutrino telescope." *Nucl. Instrum. Meth.* A742 (2014) 63–70, arXiv:1311.7002.

[26] A. V. Akindinov *et al.*, "Letter of Interest for a Neutrino Beam from Protvino to KM3NeT/ORCA." arXiv:1902.06083.

[27] https://www.km3net.org.

[28] M. deJong, "Jpp." https://git.km3net.de/common/jpp, 2019.

[29] T. Gal and M. Lotze, "Km3py." https://git.km3net.de/km3py, 2019.

[30] http://www.icrr.u-tokyo.ac.jp/~mhonda/nflx2011/index.html.

[31] https://gitlab.mpcdf.mpg.de/ift/nifty.

[32] J. Reubelt, *Hardware studies, in-situ prototype calibration and data analysis of the novel multi-PMT digital optical module for the KM3NeT neutrino telescope.* doctoralthesis, Friedrich-Alexander-Universität Erlangen-Nürnberg (FAU), 2019.

[33] D. Zaborov, "Observation of atmospheric neutrinos with orca du-2." KM3NeT interal note (KM3NeT_ORCA_2018_001-DU2_neutrino_v1.pdf), May, 2018.

[34] http://www.icrr.u-tokyo.ac.jp/~mhonda/nflx2011/index.html.

[35] S. Geißelsöder, *Model-independent search for neutrino sources with the ANTARES neutrino telescope.* doctoralthesis, Friedrich-Alexander-Universität Erlangen-Nürnberg (FAU), 2016.

[36] https://healpix.sourceforge.io/.

[37] http://antares.in2p3.fr/publicdata2017.html.

[38] A. Albert, M. André, M. Anghinolfi, G. Anton, M. Ardid, J.-J. Aubert, J. Aublin, T. Avgitas, B. Baret, J. Barrios-Martí, S. Basa, B. Belhorma, V. Bertin, S. Biagi, R. Bormuth, J. Boumaaza, S. Bourret, M. C. Bouwhuis, H. Brânzaş, R. Bruijn, J. Brunner, J. Busto, A. Capone, L. Caramete, J. Carr, S. Celli, M. Chabab, R. C. E. Moursli, T. Chiarusi, M. Circella, J. A. B. Coelho, A. Coleiro, M. Colomer, R. Coniglione, H. Costantini, P. Coyle, A. Creusot, A. F. Díaz, A. Deschamps, C. Distefano, I. D. Palma, A. Domi, R. Donà, C. Donzaud, D. Dornic, D. Drouhin, T. Eberl, I. E. Bojaddaini, N. E. Khayati, D. Elsässer, A. Enzenhöfer, A. Ettahiri,

F. Fassi, I. Felis, P. Fermani, G. Ferrara, L. Fusco, P. Gay, H. Glotin, T. Grégoire, R. G. Ruiz, K. Graf, S. Hallmann, H. van Haren, A. J. Heijboer, Y. Hello, J. J. Hernández-Rey, J. Hößl, J. Hofestädt, G. Illuminati, M. de Jong, M. Jongen, M. Kadler, O. Kalekin, U. Katz, N. R. Khan-Chowdhury, A. Kouchner, M. Kreter, I. Kreykenbohm, V. Kulikovskiy, C. Lachaud, R. Lahmann, D. Lefèvre, E. Leonora, M. Lotze, S. Loucatos, M. Marcelin, A. Margiotta, A. Marinelli, J. A. Martínez-Mora, R. Mele, K. Melis, P. Migliozzi, A. Moussa, S. Navas, E. Nezri, A. Nuñez, M. Organokov, G. E. Păvălaş, C. Pellegrino, P. Piattelli, V. Popa, T. Pradier, L. Quinn, C. Racca, N. Randazzo, G. Riccobene, A. Sánchez-Losa, M. Saldaña, I. Salvadori, D. F. E. Samtleben, M. Sanguineti, P. Sapienza, F. Schüssler, M. Spurio, T. Stolarczyk, M. Taiuti, Y. Tayalati, A. Trovato, B. Vallage, V. V. Elewyck, F. Versari, D. Vivolo, J. Wilms, D. Zaborov, J. D. Zornoza, and J. Z. and, "The search for neutrinos from TXS 0506+056 with the ANTARES telescope." *The Astrophysical Journal* 863 no. 2, (Aug, 2018) L30.

[39] J. Aublin, G. Illuminati, and S. Navas, "Searches for point-like sources of cosmic neutrinos with 11 years of ANTARES data.." *Proceedings of Science* 358 no. 2, (Jul, 2019) L30.

[40] S. A.-M. et al., "Letter of intent for KM3net 2.0." *Journal of Physics G: Nuclear and Particle Physics* 43 no. 8, (Jun, 2016) 084001.

[41] J. Bluemer, R. Engel, and J. R. Hoerandel, "Cosmic rays from the knee to the highest energies." `arXiv:0904.0725`.

[42] J. Coelho, "Oscprob." `https://github.com/joaoabcoelho/OscProb`, 2019.

[43] J. Hofestädt, *Measuring the neutrino mass hierarchy with the future KM3NeT/ORCA detector*. doctoralthesis, Friedrich-Alexander-Universität Erlangen-Nürnberg (FAU), 2017.

Danksagungen

Insgesamt gilt mein Dank allen denjenigen, die mich auf dem Weg hin zu dieser Arbeit unterstützt haben. Hierbei ist natürlich PD Dr. Thomas Eberl besonders herauszuheben, der mir durch diese Arbeit die Gelegenheit gegeben hat mich näher mit der Thematik zu beschäftigen. Der KM3NeT-Gruppe und insbesondere meinen Bürokollegen Tamás Gál und Jonas Reubelt, möchte ich für das gute persönliche Klima und die vielen fachlichen Diskussionen danken, welche immer eine große Bereicherung sind.
Ebenso geht ein Dank an Jannik Hofestädt der immer ein offenes Ohr und einen guten Rat für meine Fragen und Anliegen hatte.

Ein besonderer Dank gilt meinen Eltern, meiner Schwester Kathrin, sowie Werner und Dagi, die mich in allen Phasen meiner Ausbildung in allen Belangen uneingeschränkt unterstützt haben und mir damit in besonderer Weise mein Studium ermöglicht haben.

Des Weiteren geht mein Dank an die „Laufer-Connection“ und meine Freunde vom Eishockey, die mir zur rechten Zeit die nötige geistige Zerstreuung geboten haben, um mich danach wieder mit einem frischen Blick den Geheimnissen des Universums zu widmen.

Erklärung

Hiermit bestätige ich, dass ich diese Arbeit selbstständig und nur unter Verwendung der angegebenen Hilfsmittel angefertigt habe.

Erlangen, den 14. Oktober 2019

Johannes Schumann